

SPECIFICITY PROTEIN 1 INDUCES THE EXPRESSION OF ANGIOMOTIN IN
RESPONSE TO IL-6/STAT3 ACTIVATION TO MEDIATE YAP-DEPENDENT
GROWTH OF BREAST CANCER CELLS

Lauren R. Bringman

Submitted to the faculty of the University Graduate School
in partial fulfillment of the requirements
for the degree
Doctor of Philosophy
in the Department of Biochemistry and Molecular Biology,
Indiana University

January 2017

Accepted by the Graduate Faculty, of Indiana University, in partial fulfillment of the requirements for the degree of Doctor of Philosophy.

Clark D. Wells, Ph.D., Chair

Doctoral Committee

Maureen A. Harrington, Ph.D.

Brittney-Shea Herbert, Ph.D.

June 16, 2016

Lawrence Quilliam, Ph.D.

© 2017

Lauren R. Bringman

DEDICATION

I dedicate this dissertation to my family, especially my husband, Dr. Andrew Rodenbarger, and to my sister, Erica Mulder. Their dedication to my education, through many avenues, including prayers, understanding, and love, supported me in the completion of this work. Furthermore, I could not have made it through my graduate education without my lab mate, Brandon R. Lane or my good friends Drs. Paul Childress and Sarah Deffitt. Their comradery and counsel were exploited almost daily over the course of six years.

ACKNOWLEDGMENTS

I would like to thank my mentor, Dr. Clark Wells, for training me to think critically and for teaching me that the most challenging part of scientific research is learning to ask the “perfect questions.” It was never a challenge to spark his interest in an experimental proposal or result. Dr. Wells is also credited with teaching me to appreciate that the careful experiment design process and the thorough follow up analysis of experimental results can and should require a greater time commitment than the experimentation itself. Taking the time to design, review, and evaluate is the best way to honor the results, as well as the effort and money spent to achieve them.

I am also greatly appreciative toward the members of my committee, whose support was critical for my success. Specifically, I wish to thank Dr. George Sandusky for sharing an abundance of mammary tissue slides and expertise in pathology, Dr. Maureen Harrington for her thoughtful encouragement and carefully constructed feedback, Dr. Brittney-Shea Herbert for her knowledge, approachability, and abundant donations of cells and reagents, Dr. Lawrence Quilliam for his ever-constant donation of reagents and advice, and former committee member Dr. David Gilley for his great attention to detail.

I am very grateful for the encouragement and active collaboration on this work from my lab mates, Brandon Lane, Kevin Lange, and Anthony Folck. Further, this work would not be complete without active help from scientists like Sara Young and Dr. Ron Wek.

I would like to thank the entire Biochemistry Department office staff, especially Jack Arthur, who provided key computer-related solutions to countless problems, helpful career advice, and a kind ear for listening.

This work was funded through Department of Defense and National Institute of Health grants to Clark D. Wells.

Lauren R. Bringman

**SPECIFICITY PROTEIN 1 INDUCES THE EXPRESSION OF ANGIOMOTIN IN
RESPONSE TO IL-6/STAT3 ACTIVATION TO MEDIATE YAP-DEPENDENT
GROWTH OF BREAST CANCER CELLS**

Chronic inflammation is a major driver of tumor progression in over fifty percent of breast cancers. Tumors activate inflammatory processes by secreting factors that recruit and trigger inflammatory cells to release cytokines such as Interleukin 6 (IL-6). IL-6 stimulates the activity of signal transducers and activators of transcription 3 (STAT3), a transcription factor that has been extensively studied for its role in promoting breast cancer. Recently, downregulated HIPPO signaling was shown to drive the pro-growth effects of IL-6. Reduced HIPPO signaling allows for the nuclear translocation of transcriptional co-activator yes associated protein (YAP), implicating IL-6 in the co-activation of several transcription factors such as the TEADs that trigger pro-growth programs. While IL-6/STAT3 stimulation has been shown to increase YAP activity, the mechanism driving this remains undocumented. The Angiomotins (Amots) are adapters of the HIPPO pathway that directly bind and regulate YAP activity. Molecular characterization of Amot transcriptional regulation unexpectedly revealed a single promoter controlling the expression of its two major isoforms: Amot 130 and Amot 80. Through immunofluorescent analysis, this study found that total Amot levels were elevated across multiple breast tumor subtypes and highest in samples with increased presence of stromal inflammatory cells. Further, the induction of total Amot expression by IL-6 was found to be essential for YAP dependent growth of breast cancer cells.

The activation of Amot transcription by IL-6 was found to be through Specificity Protein 1 (Sp1), a transcription factor that is activated by STAT3. This work connects the activation of YAP1 by IL-6/STAT3 through the elevation of Amot expression by Sp1. Taken together, this explains a new avenue whereby breast cancer cells acquire enhanced oncogenic properties in response to inflammatory signaling.

Clark D. Wells, Ph.D., Chair

TABLE OF CONTENTS

List of Tables	xii
List of Figures	xiii
List of Abbreviations	xvi
Chapter 1: Introduction	1
1.1 Current facts regarding breast cancer incidence and treatments in the United States.....	2
1.2 The overview of mammary tissue polarity and its de-regulation in breast cancer	4
1.3 Inflammation and Cancer	10
1.4 Wound healing as a model to understand the impact of inflammation in epithelial systems.	11
1.4.1 Wound Healing: The Inflammatory Phase	14
1.4.2 Wound Healing: The Fibroblastic Phase.....	15
1.4.3 Wound Healing: The Re-Epithelialization Phase	16
1.4.4 From wound healing to cancer: EMT with no MET	16
1.5 Mammary cell depolarization in response to Interleukin 6 signaling	19
1.6 HIPPO signaling promotes epithelial cell polarity	22
1.7 YAP1 and TAZ as oncogenes	26
1.8 Amot 130 and Amot 80 co-coordinate YAP1 and TAZ subcellular localization	27
1.9. The major questions and hypotheses of this work	32
Chapter 2: Materials and Methods.....	34

Chapter 3: LED photobleaching reduces autofluorescence and enhances antigen retrieval of paraffin embedded human breast tissue sections	44
3.1 Prologue.....	45
3.2 Introduction	45
3.3 Materials, Methods, and Results	49
3.4 Discussion.	58
Chapter 4: Amot expression is highest in breast tissue that is undergoing a transition from DCIS to IDC, and occurs in multiple subcellular localizations.	61
4.1 Introduction	62
4.2 Materials and Methods	64
4.3 Results and Discussion.....	65
Chapter 5: A single promoter governs the transcriptional activation of the long (130 kDa) isoform and the short (80 kDa) isoform of angiotenin.....	81
5.1 Introduction	82
5.2 Materials and Methods	83
5.3 Results_	85
5.4 Discussion.	100
Chapter 6: Specificity protein 1 induces the expression of Angiotenin in response to IL-6/Stat3 activation to mediate Yap1 dependent growth of breast cancer cells.....	103
6.1 Introduction	104
6.2 Materials and Methods	104
6.3 Results	107

6.4 Discussion.....	134
Chapter 7: Discussion... ..	138
7.1 Total Amot expression levels are greater and its subcellular localization is altered in more aggressive forms of breast cancers	139
7.2 The mRNA expression of the Amot isoforms is controlled by a single promoter and result from alternative pre-mRNA splicing	142
7.3 The enhanced expression of pro-tumorigenic genes by IL-6 is Amot- dependent and requires coordinated Sp1, STAT3, and YAP1-TEAD promoter occupancy.....	144
Appendix: Nucleotide Sequences.....	149
References.....	151
Curriculum Vitae	

LIST OF TABLES

Table 2-1	Primary antibodies used in the immunoblots within this dissertation.	38
Table 3-1	Comparison of the advantages and disadvantages between different antigen staining techniques.	47
Table 3-2	Primary antibodies used in immunofluorescence staining within Chapter 3.	53
Table 4-1	Clinical features of breast tumors grades I-III.	63
Table 4-2	Characteristics of the patient samples studied in this cohort.	66

LIST OF FIGURES

Figure 1-1	A schematic of the structure of a normal breast and mammary gland.	5
Figure 1-2	Comparison of a normal mammary duct and tumorigenic mammary duct exhibiting DCIS.	6
Figure 1-3	The organogenesis of the mammary gland.	7
Figure 1-4	The structure of two contacted epithelial cells.	9
Figure 1-5	The morphology of a healing skin wound.	12
Figure 1-6	The comparison of the wound healing phenotype to the cancer phenotype.	13
Figure 1-7	Diagram of an epithelial-to-mesenchymal transition.	18
Figure 1-8	Regulation of intracellular cell polarity is innervated by the HIPPO signaling pathway.	24
Figure 1-9	The Functional Regions of the Transcriptional Co-activators YAP1 and TAZ.	25
Figure 1-10	A Schematic Diagram of the Angiomotin Family.	28
Figure 1-11	The levels of Amot transcripts indicate a potential signature for identifying invasive breast tumors vs. normal tissue.	30
Figure 3-1	Exposure of mammary tissue sections to sodium borohydride had no effect on autofluorescence reduction.	50
Figure 3-2	Exposure of mammary tissue sections to 452 nm LED light reduces autofluorescence in the GFP channel.	52
Figure 3-3	The heat produced from the LED light functions to enhance antigen retrieval of human mammary tissue.	54
Figure 3-4	The Wells lab custom Amot antibody selectively binds the Amot-specific epitopes.	57
Figure 3-5	LED photobleaching reduces mammary tissue autofluorescence at an optimized duration of 24 hrs.	59
Figure 4-1	Amot protein levels are elevated in breast tumors when compared to normal breast tissues.	67
Figure 4-2	Comparison of Amot protein expression between normal and grades I-III breast tumor tissues.	68
Figure 4-3	Comparison of Amot protein expression between normal breast tissues, and ER negative and positive breast tumor tissues.	69
Figure 4-4	Comparison of Amot protein expression between normal breast tissues, and PR negative and positive breast tumor tissues.	70
Figure 4-5	High Amot expression does not correlate with node-positive breast tumors than with node-negative breast tumors.	71
Figure 4-6	Comparison of Amot protein expression between non-metastatic/non-recurrent breast tumor tissues and pre-metastatic breast tumor tissues.	72

Figure 4-7	Comparison of Amot protein expression between non-metastatic/non-recurrent breast tumor tissues and pre-recurrent breast tumor tissues.	73
Figure 4-8	Amot protein levels are more greatly elevated in IDC breast tumors with predominant presence of DCIS than in breast tumors that lack the presence of DCIS.	76
Figure 4-9	The pattern of Amot staining and localization is variable in tumor tissues verses normal breast tissue.	77
Figure 5-1	A Schematic of the Potential Promoter Regions of the Amot gene.	88
Figure 5-2	The analysis of Amot cDNAs highlight the potential for alternative splicing of the Amot gene.	89
Figure 5-3	A single transcription start site and promoter regulate the expression of Amot 130 and Amot 80.	90
Figure 5-4	Genetic inactivation of the most 5' transcription start site eliminates mRNA and protein expression of both Amot isoforms.	92
Figure 5-5	The Amot gene has a splice junction between exons 2 and 5.	93
Figure 5-6	Compiled illustration of the unique exon splicing of the 5' leader region yielding two Amot isoforms generated from a single transcription start site.	95
Figure 5-7	The Amot isoform specific exons in the 5' leader region provide the opportunity to design primer sets that can distinguish the transcriptional activation of Amot 80 verses Amot 130.	96
Figure 5-8	A schematic of the Amot promoter and the subsequent serial deletion reporter constructs and the transcription factors found to bind the region.	98
Figure 5-9	Amot promoter activity requires the binding of the transcription factors that occur between -770 and -1473.	99
Figure 6-1	Out of three cytokines commonly found in breast cancer, IL-6 impacted Amot promoter activity as well as YAP1 and Taz protein levels.	108
Figure 6-2	CTGF and Amot mRNA levels correlate with positive cachexia marker Pax7 in muscle tissue from post-hepatectomic mice.	110
Figure 6-3	IL-6 drives the nuclear translocation of YAP1, elevates YAP1 levels, and increase the levels of YAP1 target gene CTGF through the activation of STAT3, independently of LATS1.	112
Figure 6-4	The Amot isoform-specific transcripts are not differentially regulated by IL-6/STAT3 signaling.	113
Figure 6-5	Treatment with IL-6 correlates with elevated Total Amot transcript and Amot p130 and Amot p80 protein levels.	115
Figure 6-6	The elevation of Amot transcript and protein levels by	

	IL-6 requires the activation of STAT3.	116
Figure 6-7	IL-6 elevates the Amot promoter activity above basal levels through STAT3.	117
Figure 6-8	The Amot promoter is activated by IL-6 within a responsive region between -770 and -1079 bps.	119
Figure 6-9	Amot transcript levels significantly correlate with the transcript levels of the Amot promoter transcription factor binders BACH1, MAZ, SP1, and RUNX as well as STAT3 transcript levels in breast cancer.	121
Figure 6-10	Sp1 is required for the induction of Amot promoter activity by IL-6.	122
Figure 6-11	Sp1 is required for Amot expression.	124
Figure 6-12	Sp1 depletion inhibits the elevation of CTGF transcript levels by IL-6.	125
Figure 6-13	IL-6 requires Sp1 to induce CTGF transcription and growth in poorly differentiated Her2+ breast cancer cells.	126
Figure 6-14	The inactivation of Amot by CRISPR inhibits the elevation of CTGF by IL-6.	128
Figure 6-15	IL-6 requires Amot to induce CTGF transcription and growth in poorly differentiated Her2+ breast cancer cells.	129
Figure 6-16	IL-6 requires Amot to induce CTGF transcription and growth in moderately differentiated triple negative breast cancer cells.	130
Figure 6-17	IL-6 requires YAP1 to induce CTGF transcription and growth in moderately differentiated ER + breast cancer cells.	131
Figure 6-18	IL-6 requires the coactivation of TEAD by YAP1 to induce CTGF transcription and growth in moderately differentiated ER + breast cancer cells	132
Figure 6-19	Genes that are simultaneously bound by YAP1-TEAD, Sp1, and STAT3 correlate with cancer associated genes, in contrast to genes that are bound by only YAP1-TEAD, by Sp1 and YAP1-TEAD, or by STAT3 and YAP1-TEAD.	135

LIST OF ABBREVIATIONS

3-D	3-Dimensional
5' RACE	5' Rapid amplification of cDNA ends
°C	Degrees Celsius
α	Alpha/Anti
λ	Lambda/wavelength
μg	Micrograms
μL	Microliters
μM	Micromolar
AC ₅₀	50 % active concentration
ACCH	Amot coiled-coil homology
AIP4	Atrophin-1 Interacting Protein 4
Amot	Angiomotin
Amot80	80-kDa Angiomotin protein isoform (A80)
Amot130	130-kDa Angiomotin protein isoform (A130)
AmotL1	Angiomotin-like 1
AmotL2	Angiomotin-like 2
AREG	Amphiregulin
BACH1	BTB and CNC homology 1
BCA	Bicinchoninic acid
BIRC6	Baculoviral IAP repeat containing 6
BLAST	Basic Local Alignment Tool
bp	Base pair
BPE	Bovine pituitary extract
BSA	Bovine serum albumin
C/EBPdelta	CCAAT/enhancer-binding protein delta
C.A.	Constitutive active
C188-9	STAT3 SH2 domain inhibitor
C2C12	Mus musculus muscle cells
CASR	Calcium-sensing receptor
CD	Cluster of differentiation
cDNA	Complimentary DNA
CFP	Cerulean fluorescent protein
ChIP-Seq	Chromatin immunoprecipitation sequencing
ChrX	Chromosome X
cm	Centimeters
CRISPR	Clustered regularly interspaced short palindromic repeats
C-terminus	Carboxyl terminus
CTGF	Connective tissue growth factor
DAPI	4', 6-diamidino-2-phenylindole
DAVID	Database for Annotation, Visualization, and Integrated Discovery
DCIS	Ductal carcinoma in situ
DDCT	Delta delta crossover threshold
ddl	Double deionized

DDX17	Dead box helicase 17
DMEM	Dulbecco's Modified Eagle Medium
DMSO	Dimethyl sulfoxide
D.N.	Dominant negative
DNA	Deoxyribonucleic acid
dNTP	Deoxy-nucleoside triphosphate
dT	Deoxythymine
DsRED	Far red 594 nm filter
E3	Ubiquitin ligase enzyme
ECM	Extra cellular matrix
EDTA	Ethylenediaminetetraacetic acid
EGF	Epidermal growth factor
EMT	Epithelial-to-mesenchymal transition
ENCODE	Encyclopedia of DNA Elements
ER	Estrogen receptor
EST	Expressed sequence tags
FBS	Fetal bovine serum
Fig.	Figure
FOS	FBS murine osteosarcoma viral oncogene homolog
GAPDH	Glyceraldehyde 3-phosphate dehydrogenase
GFP	Green fluorescent protein
H&E	Haematoxylin and Eosin
H3K27ac	Histone 3, lysine 27 acetylated marker of active chromatin
H3K4me3	Histone 3, lysine 4 tri-methylated marker of active chromatin
HE	High efficiency
HEK 293T	Human epithelial kidney 293-TERT
HER2	Human epidermal growth factor receptor 2
Hrs	Hours
IB	Immunoblot
IBC	Inflammatory breast cancer
IDC	Invasive ductal carcinoma
IF	Immunofluorescence
IFN γ	Interferon gamma
IHC	Immunohistochemistry
IL-6	Interleukin-6
IP	Immunoprecipitation
IRF1	Interferon regulatory factor 1
IUSCC	Indiana University Simon Cancer Center
JAK	Janus kinase
kb	Kilobases
kDa	Kilodalton
KLF	Kruppel-like factor
LATS	Large tumor suppressor
LED	Light emitting diode
IrECM	Laminin-rich extracellular matrix
LPA	Lysophosphatidic acid

KD	Knockdown
KO	Knockout
M	Molar
MAPK	Mitogen activated protein kinase
MAFF	V-Maf Avian Musculoaponeurotic Fibrosarcoma Oncogene Homolog F,
MAFK	V-Maf Avian Musculoaponeurotic Fibrosarcoma Oncogene Homolog K
MAZ	MYC-Associated Zinc Finger Protein
MCF	Michigan Cancer Foundation
MDA-MB-468	Human triple negative breast cancer cell line
Met.	Metastatic
MET	Mesenchymal-to-epithelial transition
Mer	Merlin protein
mL	Milliliters
MM	Mithramycin
ms	Milliseconds
MST	Mammalian Ste20-like protein kinase
MYC	Myelocytomatosis
MW	Molecular weight
N	Sample size
NAD(P)H	Nicotinamide adenine dinucleotide phosphate
NCBI	National Center for Biotechnology Information
NF γ A	Nuclear factor-gamma A
NF γ B	Nuclear factor-gamma B
ng	Nanograms
nm	Nanometers
N.S.	Not significant
N-terminus	Amino terminus
PALS1	Protein associated with Lin Seven 1
Par	Partitioning defective
PAX7	Paired Box 7
PATJ	PALS1-associated tight junction protein
PBS	Phosphate-buffered saline
PBX3	Pre-B-Cell Leukemia Homeobox 3
PCR	Polymerase chain reaction
PDZ	Post-synaptic density, Discs large, Zonula occludens
PEI	Polyethylenimine
PFA	Paraformaldehyde
PLC	Pregnancy lactation cycle
PR	Progesterone receptor
P-Y	Proline and tyrosine-rich motif
PPXY	2 proline residues and a tyrosine residue with a variable residue (X) in between
PS127 YAP1	Phosphorylated serine residue on YAP1
PS175 Amot130	Phosphorylated serine residue on Amot130

PY705 STAT3	Phosphorylated tyrosine residue on STAT3
qRT-PCR	Quantitative real time polymerase chain reaction
RBC	Red blood cell
Recur.	Recurring
RIPA	Radioimmunoprecipitation assay
RLM-RACE	5' RNA ligase-mediated rapid amplification of cDNA ends
RNA	Ribonucleic acid
rRNA	Ribosomal RNA
R.T.	Room temperature
RUNX	Runt-box related
S.D.	Standard deviation
SDS-PAGE	Sodium-dodecyl sulfate polyacrylamide gel electrophoresis
S.E.M.	Standard error of the mean
sg RNA	small guide ribonucleic acid
SH2	Src homology domain
shRNA	short hairpin ribonucleic acid
SKBR3	Human HER2+ breast cancer cell line
Sp	Specificity protein
STAT	Signal transducers and activators of transcription
TAZ	Transcriptional co-activator with PDZ-binding motif
TCF7L2	Transcription factor 7-like 2
TCGA	The Cancer Genome Atlas
TEAD	TEA-domain
TFBS	Transcription factor binding site
TGF- β	Transforming growth factor beta
TMA	Tumor microarray
TNF α	Tumor necrosis factor alpha
TR	Texas Red
TSS	Transcription start site
U373	Human glioblastoma astrocytoma A
Ub	Ubiquitin
UCSC	University of California Santa Cruz
UV	Ultraviolet
VP	Verteporfin
vs	Verses
v/v	Volume by volume percent
w/	With
WT	Wild-type
WW	Containing two conserved tryptophans
YAP	Yes-associated protein
YFP	Yellow fluorescent protein
ZBTB7A	Zinc Finger and BTB domain containing 7A
ZNF263	Zinc finger protein 263

CHAPTER 1: INTRODUCTION

1.1 Current facts regarding breast cancer incidence and treatments in the United States.

Despite many advances, breast cancers continue to claim the lives of approximately 1 in every 12,000 women in the United States each year, and global incidence of the disease has increased thirty-percent over the past decade [1]. The transition from the pre-invasive state of ductal carcinoma *in situ* (DCIS) to the more aggressive state of invasive ductal carcinoma (IDC) is a major area under investigation [2].

DCIS describes a pre-neoplastic state in which an intra-ductal population of heterogeneous hyperplastic cells aberrantly accumulate, yet remain contained within a polarized mammary duct [3,4]. IDC tumors have already spread locally within the surrounding breast tissue [5]. Nationwide mammogram screening data demonstrate that nearly 25 % of breast abnormalities result in the diagnosis of DCIS. Although DCIS is not an obligate precursor to IDC, DCIS to IDC transitions occur in approximately 50 % of women who do not seek immediate treatment after a DCIS diagnosis [5-8]. There is no known cause or predictor of DCIS to IDC transitions; the current standard for treatment of all DCIS cases is surgical excision followed by radiation and/or chemotherapy [6]. This conservative treatment is predominantly to prevent the development of the very aggressive inflammatory breast cancer (IBC) phenotype; DCIS precurses these highly fatal diagnoses in 15-20 % of cases. However, surgical excision is also successful in the prevention of transition to IDC [7]. Taken together, these nationwide statistics tell us that 50 % of DCIS cases will transition to IDC, 15-20 % will transition to

IBC, and 30-35 % will not experience any cancer progression [7]. This means that of the 60,290 new diagnosis of DCIS in 2015, 18,087 surgeries removed lesions that would likely not progress to either IDC or IBC [8]. The Oncotype DX DCIS Score ©, a twelve gene expression assay, has demonstrated proficiency in predicting local recurrence of node-negative breast cancer already treated with both surgical excision and tamoxifen [9]. Similarly, MammaPrint ©, a seventy gene expression assay for surgically excised breast tumor tissue, successfully predicts the potential efficacy of chemotherapy treatment [10]. Although clinical investigations of breast cancers have greatly advanced the field by incorporating mammary tumor histologic analysis and biomarker composition as tools to enhance diagnosis and prognosis, there is still no method to distinguish between the patients that stand to benefit from tumor resection and those that do not need surgery [11].

While the diagnosis of DCIS indicates a three-fold increase in the likelihood for the development of IDC, the integrity of both the ductal epithelial and myoepithelial layers can act to prevent intra-ductal hyperplasia from transitioning to IDC by invading the surrounding stroma [11,12]. The field currently lacks a comprehensive understanding of the signaling pathways that, when dysregulated, contribute to the degradation of polarized ductal epithelial tissue. The absence of this knowledge hinders the improvement of current prognoses and treatments, and leaves key questions regarding the natural history of this disease unanswered [13,14]. The work described in this dissertation seeks to provide a greater appreciation for the dysregulation of

pathways that support a polarized ductal epithelium, a potential cause of the transition of pre-invasive ductal carcinoma *in situ* (DCIS) to the aggressive state of invasive ductal carcinoma (IDC) [4,15].

1.2 The overview of mammary tissue polarity and its de-regulation in breast cancer.

The study of the natural history of the breast begins with the understanding the structure of normal breast physiology. The cross-sectional structure of the functional mammary gland is comprised of a myoepithelial outer layer adjacent to a stratum of polarized epithelium that surround a hollow inner lumen. Longitudinally, this structure forms a long hollow hose that extends toward the nipple. The duct is nestled within layers of adipose tissue capable of synthesizing and secreting various hormones [16]. Upon the activation via hormonal signaling, the mammary gland is designed to secrete and deliver breast milk to a suckling infant (Fig. 1-1, 1-2 (Left)). The health and function of the mammary duct requires the maintenance of a strongly polarized epithelium [17,18]. Paradoxically, this requires a regular regeneration cycle that involves the depolarization, cellular clearing, regrowth, and re-polarization of new epithelial cells. Additionally, this standard regeneration cycle is accompanied by several more drastic remodeling events that comprise the natural history of the breast, including pubertal expansion, pregnancy/lactation-associated remodeling, and post-lactational/menopausal associated involution (Fig. 1-3) [13]. At the cellular level, these major remodeling events require the modulation of epithelial

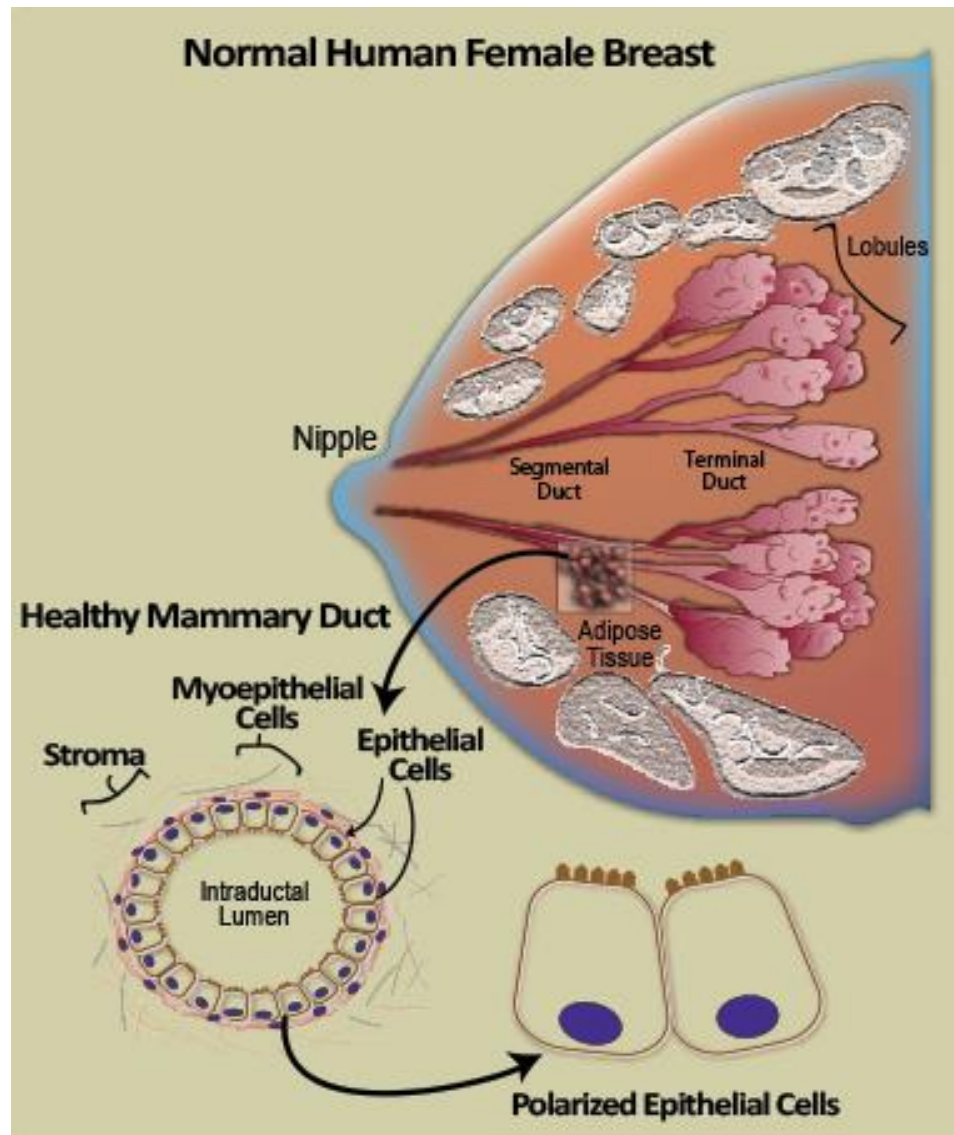


Figure 1-1. A schematic of the structure of a normal breast and mammary gland. The normal human female breast is comprised of polarized mammary epithelial tissue surrounded by a layer of myoepithelial and stromal cells. Longitudinally, the mammary duct forms an extended tubular structure: The lobules and terminal ducts point toward the breast bone and extend all the way to the nipple. The myoepithelial cells add integrity and flexibility to the tubule, allowing for gentle squeezing in the event of milk secretion. Latitudinally, the mammary duct is composed of polarized epithelial cells with strong cell-cell contacts that support a permeable barrier separating the intraductal lumen from the stroma. These structures are supported by hormone producing adipose tissue. Figure designed by Clark Wells, PhD. and adapted by Lauren Bringman May 2016.

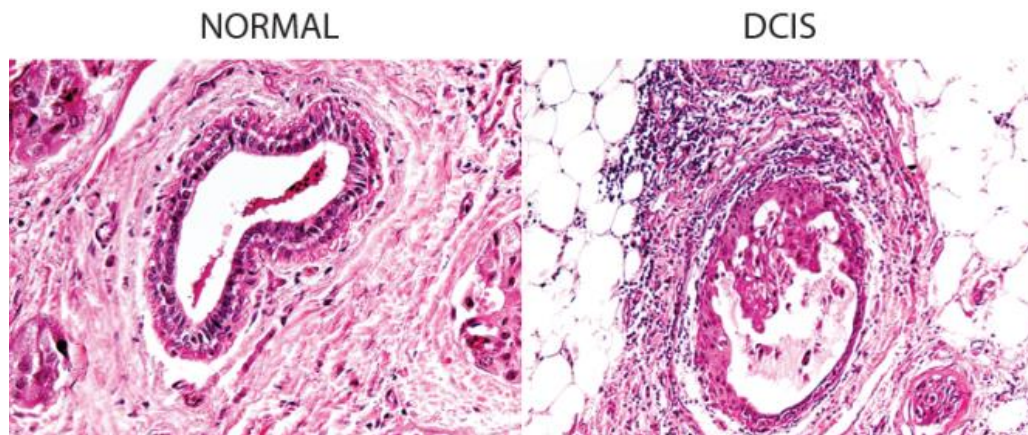


Figure 1-2. Comparison of a normal mammary duct and tumorigenic mammary duct exhibiting DCIS. This haemotoxylin and eosin (H&E) staining of normal mammary tissue displays a hollow lumen and healthy stroma, and DCIS mammary tissue displays a lumen positive for tumor cells and stroma with lymphocytic infiltration. Nuclei are stained purple and stromal and connective tissue are stained in pink. Slides were provided by George Sandusky, PhD. and were stained and imaged by Lauren Bringman.

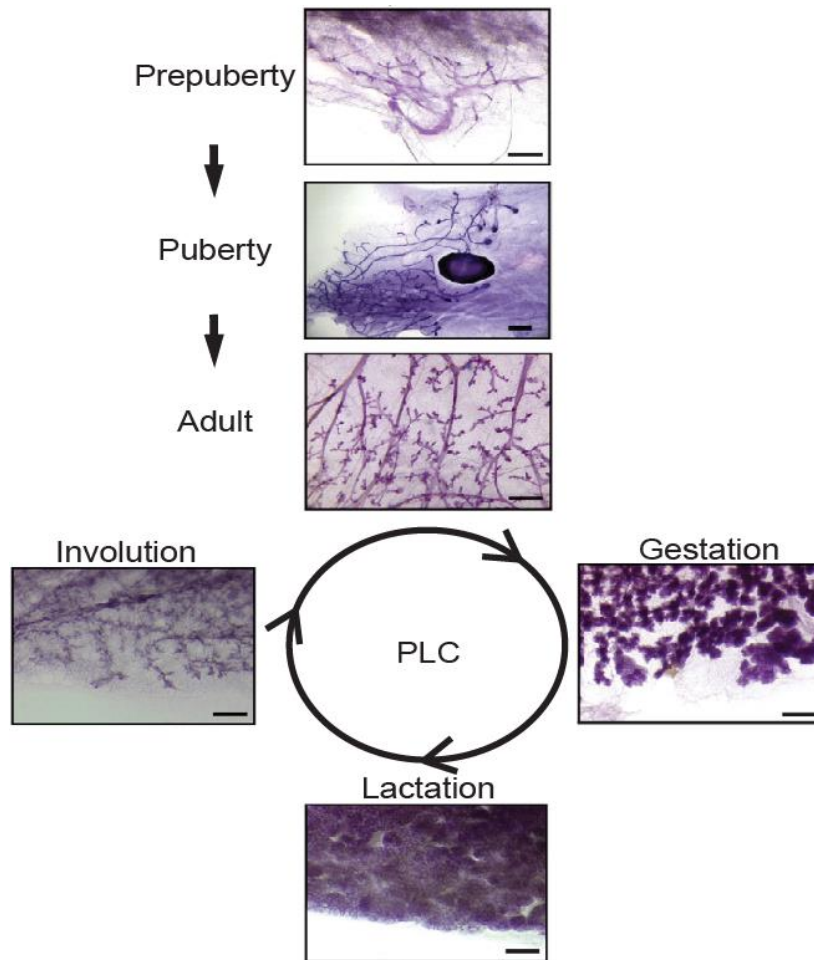


Figure 1-3. The organogenesis of the mammary gland. Images of murine mammary tissue whole mount slides representing all of the phases of glandular development. Image 1 represents the pre-pubertal mammary tissue of a 2-week old pup and displays minimal presence and branching of ductal structures. Image 2 represents the pubertal mammary tissue of a 5-week old mouse, and displays a significantly enhanced presence and increased branching of ductal structures. Image 3 represents the adult mammary tissue of a 10-week old mouse and displays highly organized and branched ductal structures. Image 4 represents the mammary tissue during gestation of a pregnant mouse (gestation day 18.5) and displays a significant increase in the number and size of ducts. Image 5 represents the mammary tissue during lactation and displays enlarged ductal structures likely engorged with milk. Image 6 represents the involuting mammary gland of a mouse 8 days post-lactation and displays the a return of the number and size of ductal structures to that of the pre-gestational adult mouse. The cycle of morphological changes between the adult, gestational, lactating, and involuting mammary tissue is known as the pregnancy and lactation cycle (PLC). These images collectively represent the highly dynamic structure of the mammary gland. Scale bars = 1 mm. Figure designed by William Ranahan. Figure adapted from [1].

cell polarity. A polarized epithelial layer can contain hundreds of apico-basal epithelial cells held tightly together via tight and adherens junctions. This structure is represented in a wide variety of body tissues including the inner lining of the gastrointestinal tract and uterus, and the outer layers of the epidermis [19]. These tightly bound cells support the health of ductal tissue by functioning as a permeable barrier that carefully filters the exchange of molecules, cells, and other tissue debris between cells from the basal face to the apical face, and vice versa (Fig. 1-4). This organization underlies proper milk secretion by the mammary gland [20-22].

Changes to the exterior cell structure modify internal cell signaling. The subcellular localization of proteins that mediate signaling that translates external cues onto cellular behavior differs dramatically between an actively proliferating cell and a polarized cell [23-25]. Highly polarized ductal epithelial cells are growth arrested due to active growth controlling signaling pathways such as the HIPPO signaling pathway [26,27]. In contrast, the loss of cell polarity enables growth by inactivating HIPPO signaling and the wiring of growth promoting pathways such as the mitogen activated protein kinase (MAPK) signaling pathway [12,28,29]. The primary cues supporting cell polarity include the formation of tight junctions and adherence junctions. Their formation dictates cell shape, which in turn drives the asymmetrical organization of organelles, the cytoskeleton, and most protein complexes [24,30] (Fig 1-4).

The dysregulation of mechanisms that control cellular polarity is intricately connected to the development and progression of cancer. The cyclical

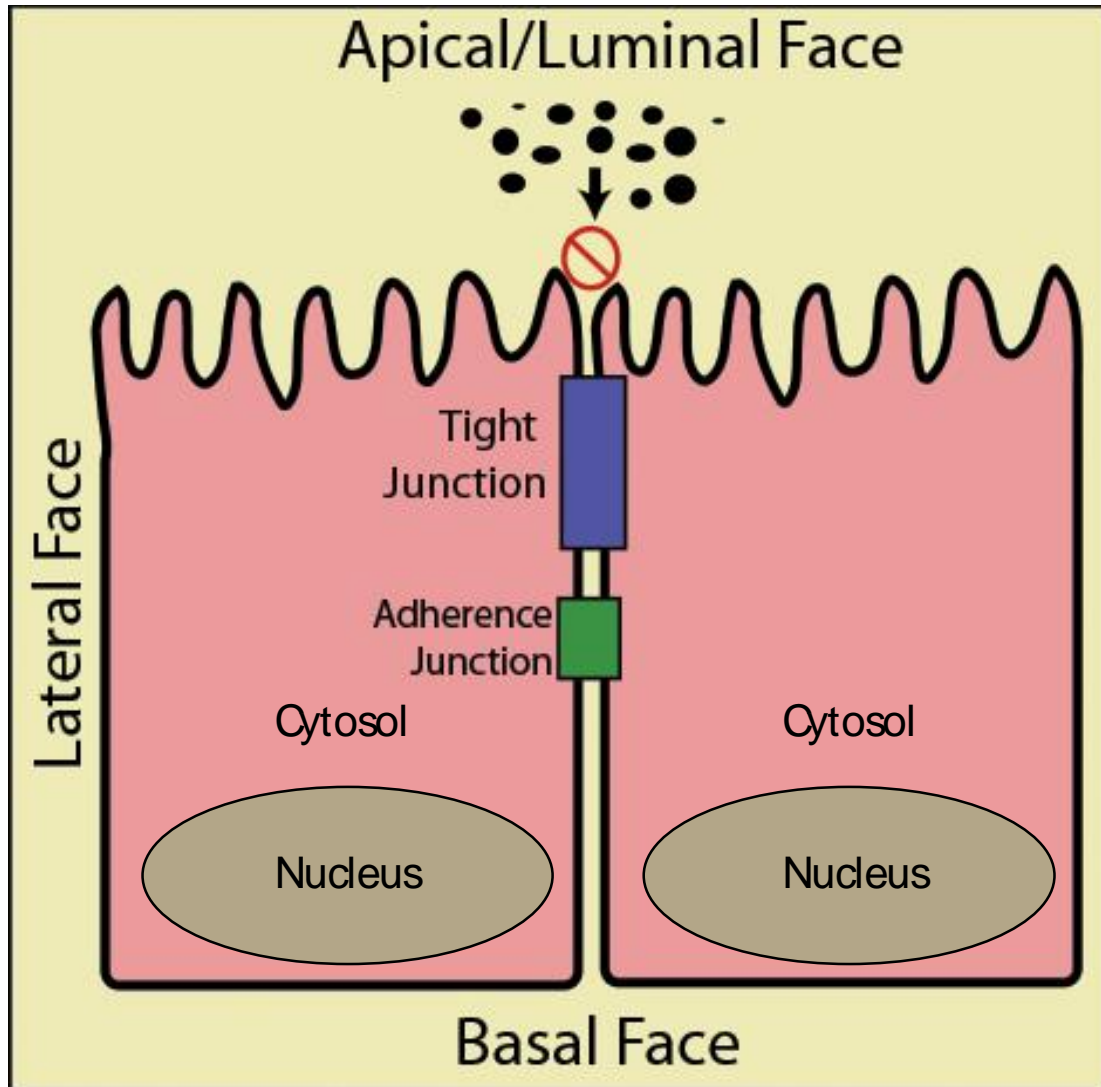


Figure 1-4. The structure of two contacted epithelial cells. Polarized epithelial cells possess three distinct faces (i.e. lateral, basal, and apical) that are maintained by the contact through junctional protein complexes adherence and/or tight junctions. The structural polarity signals intracellular polarity with respect to protein localization and cytoskeletal structure. Permeability is restricted which prevents molecules from transferring through the epithelial stratum. Figure was designed by Clark Wells, PhD. and adapted by Lauren Bringman.

neoplastic outcomes [17]. For instance, if cells remain depolarized, the proteins that drive transcriptional programs that promote cellular divisions are often no longer sequestered from the nucleus and thereby can induce aberrant cell divisions associated with hyperplastic growth in the mammary duct. If this cell happens to contain a pro-oncogenic mutation, then the ability of that constitutively active protein to transmit signaling is greatly amplified [31] [32]. One of the best examples of this occurring is in the ability of chronic inflammation to promote carcinogenesis in epithelial tissue composed of cells that contain oncogenic mutations. Through the release of pro-growth factors such as cytokines, inflammation activates the sustained dedifferentiation and proliferation of otherwise highly polarized, growth arrested cells.

1.3 Inflammation and Cancer

The connection between the immune system and cancer is overwhelmingly two-sided. One on hand, over eleven new classes of immunotherapeutic drugs aimed at stimulating the antitumor immune response have been developed in the last 10 years [33]. Yet, on the other hand, the impacts of chronic inflammation on tumorigenesis have also been widely observed for centuries [34-37]. For example, thorough investigation into this link by thousands of groups has demonstrated that an inflammatory microenvironment is unequivocally critical for the support of tumor growth and progression in a variety of tissue types [38]. Martel and Franceschi 2009 were first to establish and categorize the correlation between bacterial and/or viral

infection induced inflammation and the increased risk of cancer development [39,40]. Additionally, accumulating evidence indicates that the carcinogenicity of tobacco products is due in large part to their ability to establish a chronic inflammatory state in the lung tissue [41]. More surprisingly, chronic inflammation has been shown to correlate with a marked reduction in chemotherapeutic efficacy [42]. Accumulation of damaged DNA and cell senescence within a cell can produce secreted protein-based pathogens that initiate an immune response. [43,44].

1.4 Wound healing as a model to understand the impact of inflammation in epithelial systems.

The connection between inflammation and cancer was first observed by Rudolf Virchow in 1863 who noted the high frequency in which tumors develop in post-trauma fibrotic tissue [34]. The mechanisms underlying wound healing are key in the study of epithelial cell depolarization in response to inflammatory cues (Fig 1-5). Wound healing is defined as the remodeling of tissue damaged through physical or chemical trauma. This occurs through a tightly regulated program involving the dedifferentiation, proliferation, migration, and redifferentiation of the cells composed in and around the wound site. Wound healing is characterized by three phases of tissue remodeling: inflammatory, fibroblastic, and re-epithelialization (Fig 1-5). These three events have been shown to take place in the pro-inflammatory tumor microenvironment (Fig. 1-6) [45,46].

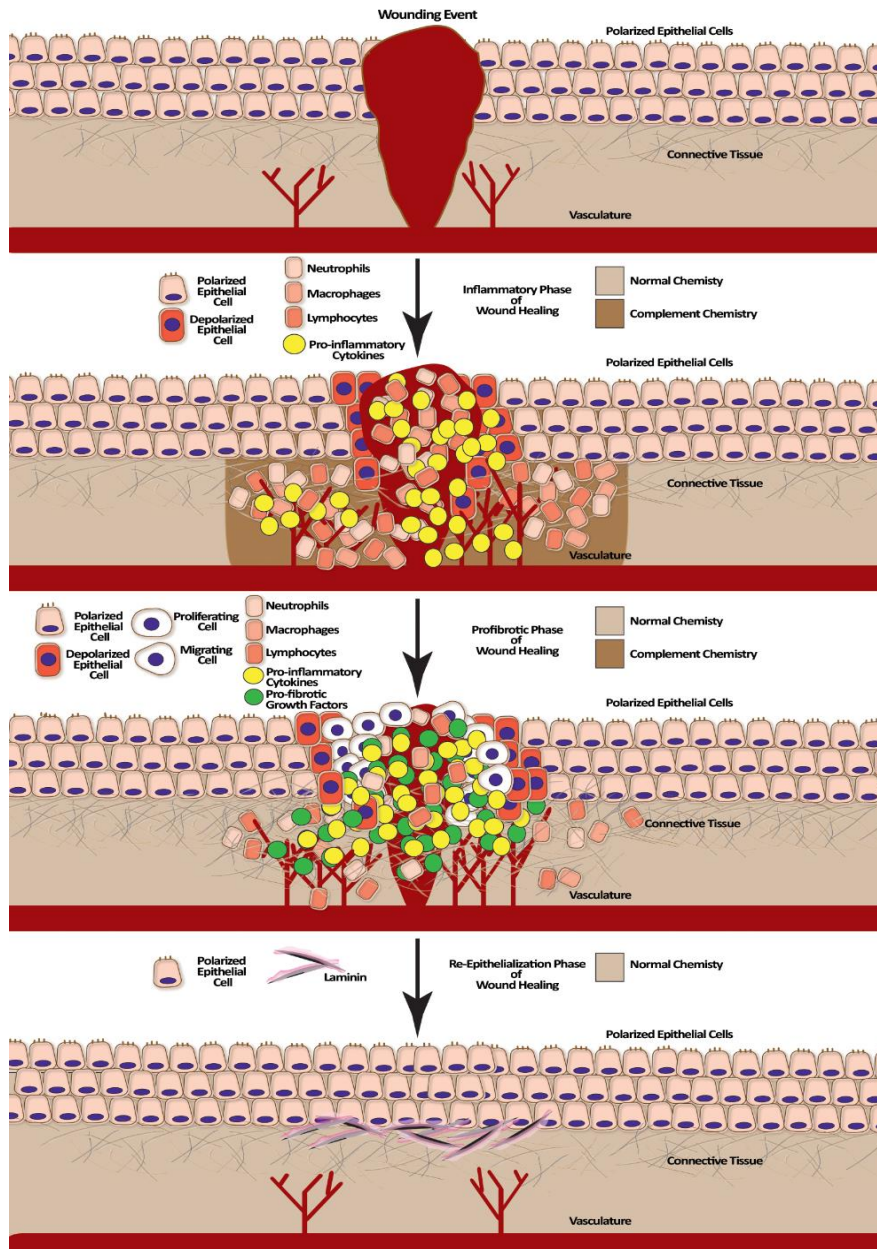


Figure 1-5. The morphology of a healing skin wound. The inflammatory phase of wound healing initiates a rapid influx of macrophages and neutrophils, followed by the recruitment of lymphocytes that drive the production of pro-inflammatory cytokines that protect host epithelial cells from the toxic environment created by the complement cascade of proteolysis. Pro-inflammatory cytokines such as IL-6 signal the epithelial cells to survive, proliferate, and induce the profibrotic phase through the production of pro-fibrotic growth factors such as CTGF to drive the development of new connective tissue. In the re-epithelialization phase, the production of laminin and other pro-differentiation factors fosters enhanced cell polarity to drive the re-epithelialization of the tissue cells and facilitate wound closure.

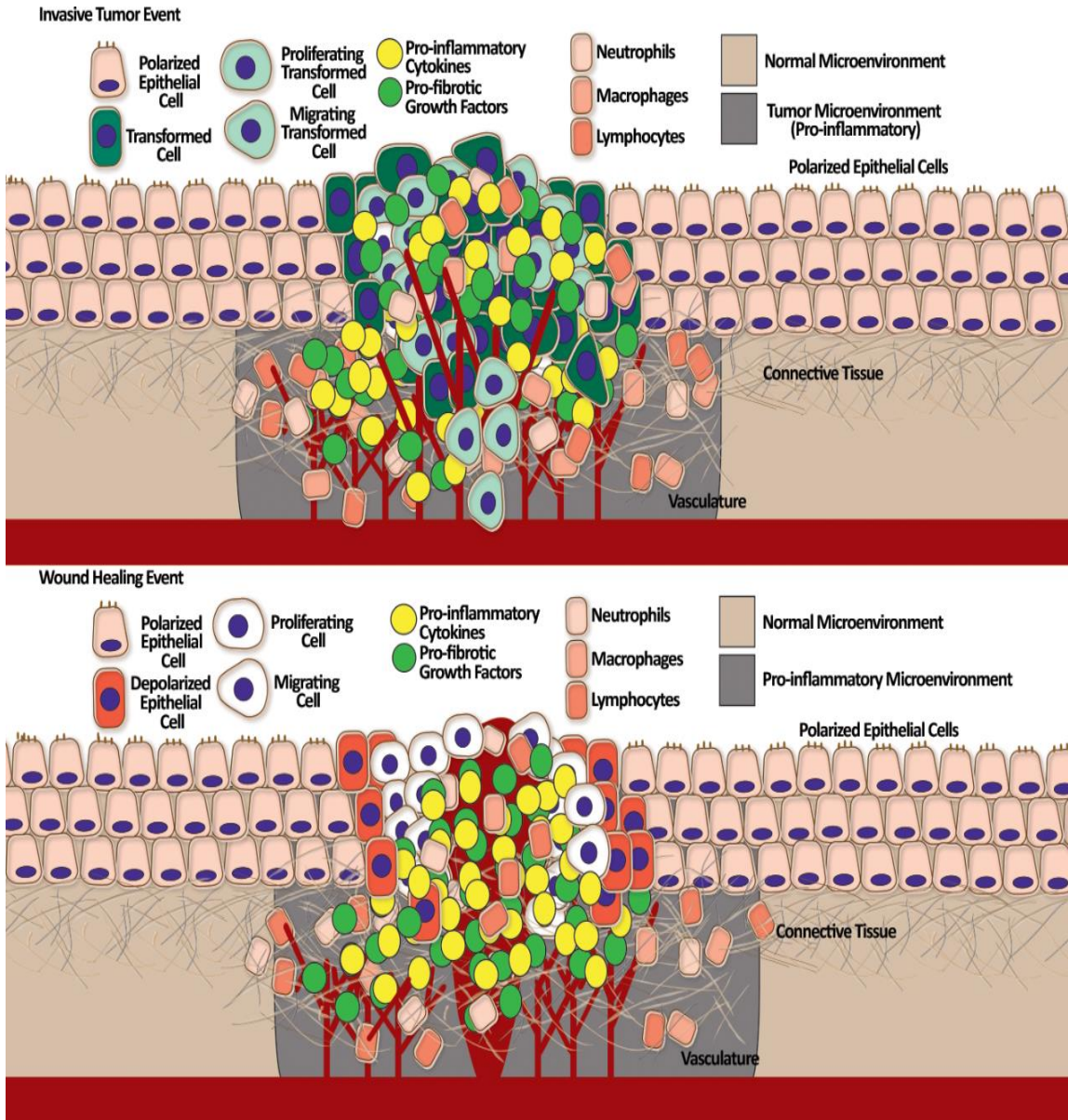


Figure 1-6. The comparison of the wound healing phenotype to the cancer phenotype. An illustration of an invasive tumor (a) as it compares to a healing wound (b). Both phenotypes are characterized by the influx of inflammatory cells, fibrosis, and vascularization.

1.4.1 Wound Healing: The Inflammatory Phase

Inflammation is a defensive response from the connective tissue surrounding a wound site which functions to abolish the source of damage, eliminate pathogenic invasion, and repair damaged tissue cells [45]. The inflammatory phase commences upon tissue damage by activating a localized acute inflammatory response that involves a vascular reaction followed by a cell based reaction [45,47]. Blood vessels surrounding the damage site enlarge to increase blood and nutrient supply, and pro-proteins found in the blood undergo cleavage and subsequent activation by what is known as the complement protease cascade. This cleavage of over thirty complement-associated proteins creates a toxic microenvironment that facilitates the opsonization of bacterial and viral invaders by neutrophils, lysis of foreign cells, and agglutination of pathogens for degradation. These processes also induce the recruitment of macrophages and lymphocytes by chemotaxis, which initiates the cell-based inflammatory reaction [48-50]. Macrophages engulf cellular debris to neutralize the otherwise toxic environment. T-lymphocytes secrete cytokines and also activate macrophages to follow suit. These cytokines are small proteins (5-20 kDa) that bind and signal host epithelial cells to initiate host protective responses including apoptotic evasion, dedifferentiation, and proliferation in spite of the toxic inflammation microenvironment [45,51,52]. The inflammatory phase of wound repair induces the eradication of foreign invaders and promotes the regrowth of healthy cells to comprise the newly repaired tissue. While the infiltration of inflammatory cells is a hallmark of cancer, the roles of the inflammatory phase of

wound repair in cancer development is a very active area of ongoing research [36,37].

1.4.2 Wound Healing: The Fibroblastic Phase

The fibroblastic phase of wound repair initiates fibrosis, a process in which the supportive connective tissue is rebuilt. Connective tissue underlies mammary epithelium, originates from mesenchyme, and is comprised of fibroblasts, macrophages, mast cells, neutrophils and lymphocytes [53,54]. Fibrosis rebuilds the structural and chemical foundation to support the integrity and health of the newly repaired tissue. Structurally, this often results in the development of visible and occasionally palpable scar tissue [55]. The connective tissue supporting mammary epithelium possesses both a loose and dense consistency, and is classified as irregular, in which thick, multi-planar fibers make up fibrous capsules that surround the gland. This is in contrast to regular connective tissue including tendons, ligaments, cartilage, and blood, which all contain thin single planar fibers [56].

The fibrotic process is initiated by pro-fibrotic growth factors that are secreted by proliferating epithelial cells at the wound site in response to their exposure to pro-inflammatory cytokines such as interleukin (IL-6). Of these pro-fibrotic factors, Connective Tissue Growth Factor (CTGF) is one of the most studied and most important factors in this process [57-59]. In physiological wound healing, CTGF directs fibrosis signaling that underlies scar formation through its ability to induce cells to secrete extra-cellular matrix components. The resulting accumulation of ECM facilitates vascularization and immune cell

recruitment at the site of the wound. Increased levels of CTGF in sera, urine, and plasma is a clinically dominant diagnostic marker for fibrosis [60,61]. Pathologic/inappropriate CTGF signaling fosters a tumor promoting environment [62-66].

1.4.3 Wound Healing: The Re-Epithelialization Phase

The reformation of connective tissue in the fibroblastic phase of wound healing provides the foundation that fosters the seeding of new cells for re-epithelialization (differentiation). Re-epithelialization is necessary for complete wound closure, where a tight permeable barrier from the re-establishment of cell to cell junctional complexes is formed [67-69]. In skin wounds, re-epithelializing keratinocytes exhibit a lamellipodial cell structure, characteristic of mesenchymal migration [68]. This indicates the dynamic role that newly proliferated cells play; their migration is both calculated and highly organized.

Once new cells arrange in the correct organization, they begin to differentiate into polarized epithelial cells where cell-cell contact initiates signaling that induces expression and junctional localization of tight and adherens complex proteins. In addition, these sub-basal layer cells are signaled to organize their basement membranes in response to contact with the laminin freshly remodeled connective tissue [68-69].

1.4.4 From wound healing to cancer: EMT with no MET

The wound healing cycle requires several dramatic changes in cell structure. This initiates when polarized epithelial cells are induced to de-differentiate into primitive mesenchymal cells, an event appropriately named an epithelial to mesenchymal transition (EMT) [23,70]. During an EMT event, cells lose cell-cell contacts to allow for their reorganization which is significantly mediated by the induction of new pro-EMT transcriptional programs that result in decreased expression of E-Cadherin and increased expression of N-Cadherin, Vimentin, Snail, and Twist. Re-epithelialization in physiological wound healing drives the reversed transition of cells from a mesenchymal phenotype to the more differentiated epithelial phenotype, known as an MET event. These newly differentiated epithelial cells regain E-Cadherin expression and again lose N-Cadherin, Vimentin, Snail, and Twist expression (Fig 1-7) [71]. In addition to wound healing, normal physiology requires the process of EMT / MET under instances of healthy tissue remodeling, such as in the maintenance of the mammary gland [16,72,73].

The field of breast cancer research has focused a great deal of attention on the concept of EMTs as a necessity for the initiation and promotion of breast cancers. Pathological EMTs occur in response to inappropriate signaling from the extracellular matrix, and direct the loss of a polarized epithelial layer. This process is highly exploited in various carcinomas to effect the initiation of cellular invasion programs associated with metastasis. In the mammary duct, EMTs create a “leaky duct” that can no longer prevent oncogenic cells that fill the intra-

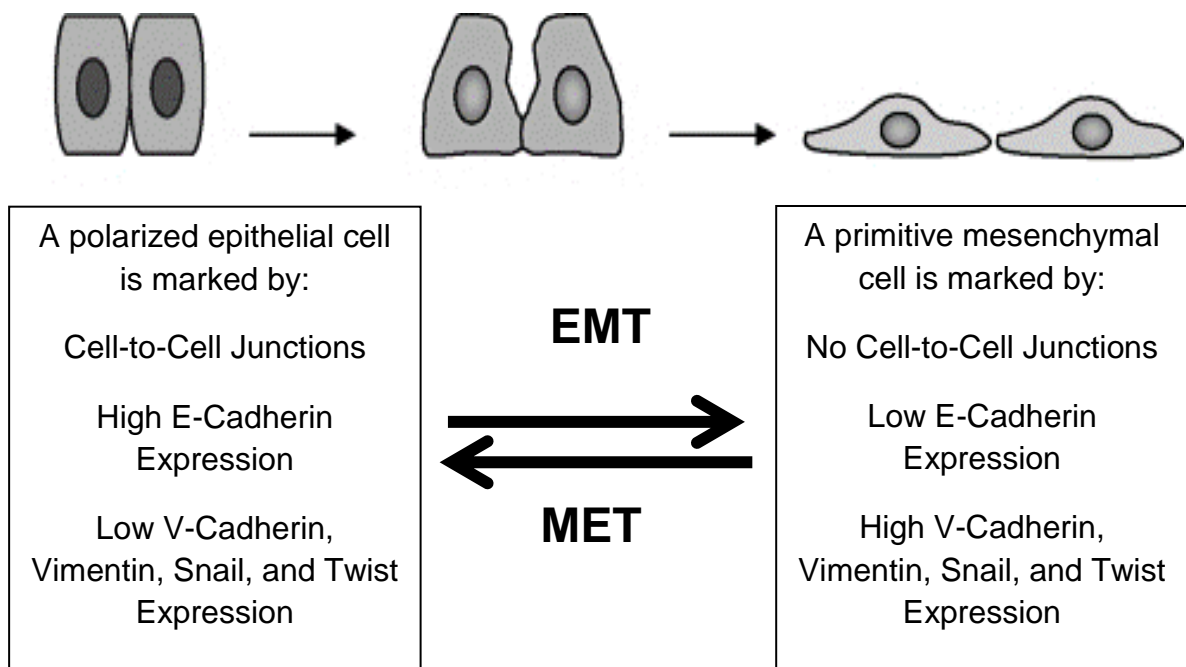


Figure 1-7. Diagram of an epithelial-to-mesenchymal transition (EMT/ mesenchymal-to-epithelial transition (MET)). Polarized epithelial cells lose cell-to-cell contacts and levels of E-cadherin, and gain an increase in V-cadherin, vimentin, snail, and twist levels (EMT) and vice versa (MET). EMT events occur during the regular remodeling of epithelial tissue, as well as in tumorigenesis.

ductal lumen from invading into the surrounding stroma [23,70,72-77]. Thus, the initiation of EMTs is a major process contributing to the transition of DCIS to IDC [78]. Further, once the cells break free from adjacent cells in the mammary duct, they are free to invade the surrounding stroma and to eventually metastasize by entering the bloodstream which allows their dissemination to distant secondary sites. This concept comprises the dogma that the maintenance of epithelial polarity is a fundamental tumor suppressive mechanism at both the cellular and tissue levels [17,18,79].

1.5 Mammary cell depolarization in response to Interleukin 6 signaling

The secretion of interleukin 6 (IL-6) by macrophages and lymphocytes has been directly linked to driving pathological EMT events in the breast [70,72,75-77]. First discovered by Hirano et al. 1986, IL-6 is a 27 kDa soluble cytokine that is commonly upregulated in the immune cells that respond to wound healing, sites of infection, and tumorigenesis [80]. Throughout the progression from normal breast tissue to infiltrative ductal carcinoma (IDC), increased infiltration of inflammatory cells that secrete cytokines into the parenchymal and stromal tissue ensues. The presence of CD3+ T cells, CD68+ macrophages, and CD+20 cells is elevated, with the presence of highly secreting activated T cells increasing most prevalently [3]. T-lymphocytes and macrophages, when activated, upregulate and secrete IL-6 [35,80]. IL-6 has been found to signal host cells to initiate a variety of cell programming events to direct survival, proliferation, angiogenesis, etc. Inappropriate signaling by IL-6 plays a dramatic role in tumorigenesis and

tumor progression. Serum levels of Interleukin 6 (IL-6) are elevated in the stroma surrounding the tumorigenic mammary gland.

IL-6 promotes pro-tumorigenic effects by binding to cell surface receptors linked to the Janus Kinase (JAK)-coupled receptors subcellular localization that in turn phosphorylate and activate members of the signal transducers and activators of transcription (STAT) family, in particular STAT1 and STAT3 [3,81-83]. Of the seven STAT proteins, STAT3 is most commonly identified in a constitutively phosphorylated form in cancers. Phosphorylated STAT3 (P-STAT3) has been extensively studied for its role in activating the transcription of specific genes that promote cancer [72,84,85]. Specifically, STAT3 signaling occurs when extracellular IL-6 binds to the IL-6 receptor (IL-6R) present on the surface of epithelial cells. The IL-6R contains two subunits, gp130 and gp80. Once the conformational change is induced via IL-6 ligand binding, the activation of the Janus Kinases 1/2 (JAK 1/2) proceeds via gp130. JAK1/2 function to phosphorylate STAT3. The phosphorylation event of STAT3 exposes an SH2 domain, which provides a high affinity binding site for a homodimer to form. This rapid homodimerization event correlates so highly with the phosphorylated state of STAT3 that P-STAT3 is assumed to always exist in a homodimer complex. STAT3 homodimerization reveals a powerful set of nuclear localization sequences, which drive the nuclear translocation of P-STAT3 and promotes the activation of thousands of pro-growth and pro-survival genes [81,86].

It has been estimated that more than three thousand promoters are bound and directly activated by P-STAT3 [87]. Additionally, through the upregulated

expression of many transcription factors by STAT3, the number of promoters that are indirectly activated by STAT3 is nearly immeasurable. For instance, STAT3 activates the transcriptional expression of the transcription factor Specificity Protein 1 (SP1), which, in turn, also activates the transcription of over 3000 promoters [87]. SP1 is an 81 kDa protein and one of the nine proteins belonging to the Specificity Protein/Kruppel-Like Factor (Sp/KLF) family of zinc finger transcription factors. These transcription factors specifically bind to GC boxes contained in thousands of gene regulatory regions. Sp1, in particular, has been shown to directly activate the transcription of genes that regulate chromatin remodeling and DNA damage repair, cell growth, differentiation, apoptosis, and even immune responses [74,88-92]. The increased expression of Sp1 by P-STAT3 is implicated in the uncontrolled growth of cancer cells [87,88,93].

P-STAT3 has also been reported to regulate biochemical signaling mechanisms independent of its DNA binding function. For example, P-STAT3 has been implicated in the nuclear recruitment of other transcription factors. Interestingly, an example of this lies in the crosstalk between STAT3 and Sp1 [87]. Sp1 and STAT3 have been shown to co-dependently activate the transcription of a variety of genes with promoters that contain adjacent Sp1 and STAT3 binding sites including JAK3 and C/EBPdelta [93-95]. Additional studies have found that the physical interaction of STAT3 and Sp1 is induced by IL-6 to facilitate the promoter activation of the calcium-sensing receptor (CASR) gene [93].

P-STAT3 and SP1 have both been shown to bind the promoter of pro-

fibrotic factor CTGF [96]. In addition to driving fibrosis and ECM accumulation, CTGF also triggers proliferation, mitogenesis, apoptotic evasion, chemotaxis (directional cell migration), chemokinesis (random migration), invasion, and inflammatory cell infiltration, and has been implicated in the driving of EMTs [57-59,64,97-101]. CTGF is upregulated in response to IL-6 [57] and has also shown to be activated by Sp1 to promote dedifferentiation via signaling through Transforming Growth Factor β (TGF β) [74]. Elevated CTGF levels are found in melanoma, pancreatic cancer, breast cancer, and in the regenerating liver, and is implicated in cardiac immunorejection and fibrotic disease of the kidney and liver [52,57,58,62,65,66,102]. CTGF possesses far more TEA Domain (TEAD) binding sites in its promoter than STAT3 and Sp1 binding sites [96], and its promoter activation is dramatically enhanced by occupancy by the yes-associated protein (YAP1)-TEAD nuclear complex [103-105]. The predominant pathway which antagonizes YAP1-TEAD dependent activation of pro-tumorigenic CTGF signaling and maintains epithelial polarity is the HIPPO Signaling Pathway [19,106,107].

1.6 HIPPO signaling promotes epithelial cell polarity

Recently, the HIPPO signaling pathway, as a promoter of intracellular epithelial polarity, has been demonstrated to resist EMT events [108]. The HIPPO signaling pathway was first discovered in *Drosophila melanogaster* through the execution and analysis of mosaic screenings for mutant tumor suppressor proteins [109]. The ablation of a number of HIPPO pathway

components yielded dramatic cell overgrowth and apoptotic evasive phenotypes, implying a widespread tumor suppressive characteristic of the HIPPO signaling pathway [109-111]. Further studies revealed the pathway's high activity in development through the control of organ size [112]. Since its elucidation in *Drosophila* just over 20 years ago, the study of HIPPO signaling has been appreciated to function in all metazoans including humans in almost 1100 completed studies.

HIPPO Pathway Signaling can be broken down into two main components. 1. The growth inhibitory serine/threonine kinase component and 2. The growth activating transcriptional component. The kinases in the first component include mammalian STE20-like protein kinase 1 and 2 (MST1/2) and large tumor suppressor 1 and 2 (LATS 1/2) and function to terminate growth when active. The transcriptional coactivators in the second HIPPO pathway component include functional analogues yes associated protein (YAP1) and transcriptional coactivator with a PDZ binding motif (TAZ) [109,111,113]. The kinases in component 1 function to phosphorylate and thereby inactivate the coactivators in component 2. This phosphorylation event inhibits YAP1 and TAZ by allowing their association with protein 14-3-3 and enable their sequestration in the cytosol. In cases where MST1/2 and LATS1/2 remain inactive, unphosphorylated YAP1 and TAZ are free to translocate to the nucleus where they stimulate the transcription of pro-growth and –survival genes. Both YAP1 and TAZ stimulate growth and cell survival when active (Fig. 1-8; 1-9) [112,114,115].

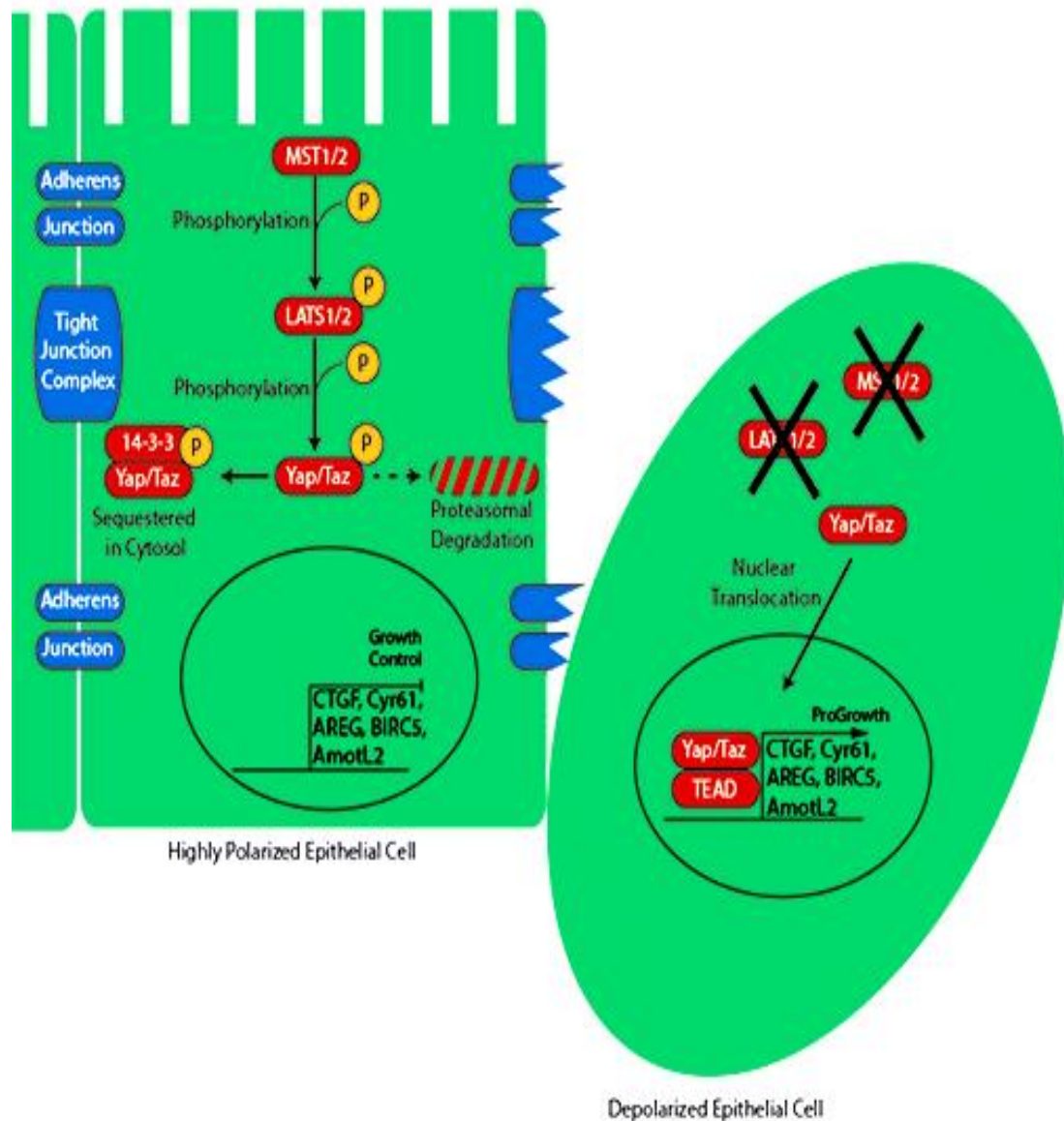


Figure 1-8. Regulation of intracellular cell polarity is innervated by the HIPPO Signaling Pathway. Tight and/or adherens junctions aid in the control of cell shape and the intracellular protein localization. In response to external cues of polarization, such as cell-to-cell contact through adherens and tight junctions, the HIPPO Signaling Pathway directs intracellular polarity upon the activation of HIPPO pathway kinase cascade involving mammalian STE20-like protein kinase 1 and 2 (MST 1/2) and large tumor suppressor 1 and 2 (LATS1/2) which, in turn, phosphorylate HIPPO co-activators YAP1 and TAZ. These phosphorylation events encourage either their degradation or their binding and cytosolic sequestration by the tumor suppressor 14-3-3. These cytosolic events prevent the nuclear translocation of YAP1 and TAZ, thus preventing the coactivation of transcription factors that stimulate the transcription of multiple pro-growth and pro-survival genes such as CTGF, Cvr61, Amphiregulin (AREG), BIRC6, and AmotL2.

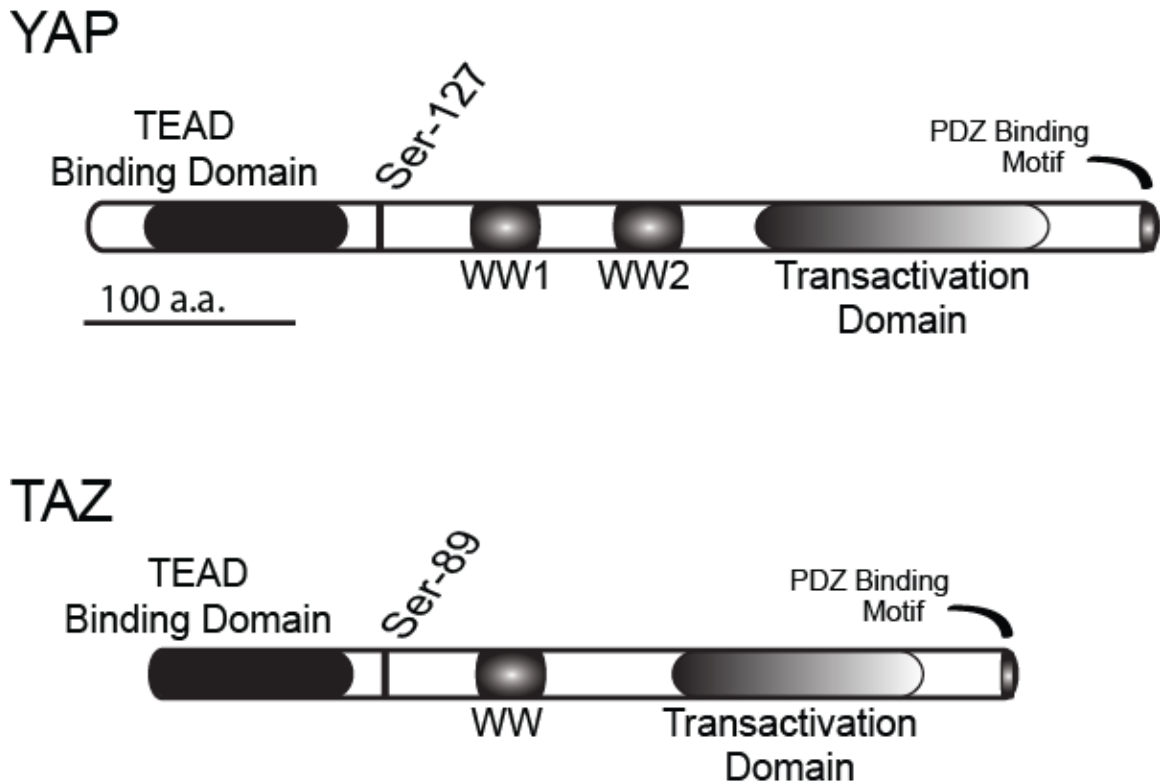


Figure 1-9. The Functional Regions of the Transcriptional Co-activators YAP1 and TAZ. Both YAP1 and TAZ possess an N-terminal TEA domain (TEAD) transcription factor binding domain, a transactivation domain, serine phosphorylation sites, and a C-terminal PDZ binding motif. YAP1 possesses two WW (tryptophan-tryptophan) domains and TAZ possesses one. The TEAD domains allow for YAP1 and TAZ to bind and co-activate TEAD transcription factors 1, 2, 3, and 4. The trans-activation domains of YAP1 and TAZ have been shown to be required for their transcriptional coactivation activity. The serine phosphorylation sites allow for these proteins to be regulated via phosphorylation by LATS. The PDZ binding motifs allow for YAP1 and TAZ to interact with other proteins that possess PDZ binding motifs. Finally, the WW domains allow for YAP1 and TAZ to associate with various Angiomotin proteins and LATS which regulate their activity.

Through gene amplification and inactivation of HIPPO signaling, the direct enhancement of both YAP1 and TAZ levels correlates with enhanced malignancy in most cancers. Further, the activation of the tumor microenvironment that favors a loss of cell-cell contacts leads to neoplastic cell growth [103,104,116-118]. Surprisingly, with the exception of a rarely occurring LATS2 mutant found in multiple myeloma, no germline or somatic mutations of any of the Hippo pathway components consistently occur in cancers. This led researchers to appreciate that the predominant mechanism including increased mechanotransduction or by mitogenic signaling through GPCRs. Taken together, it is clear that the dysregulation of the HIPPO pathway contributes greatly to tumorigenesis.

1.7 YAP1 and TAZ as oncogenes

Hyperactivation of YAP1 and TAZ is pervasive across a multitude of cancers, and has demonstrated sufficiency both in developing and sustaining tumor growth [21,30,104,110,116,119]. A variety of studies have shown that the inactivation of YAP1/TAZ regresses tumorigenic properties, including stemness, resistance to anoikis, migration, and metastatic potential. Nuclear YAP1/TAZ is also enhanced by highly stiff extra cellular matrices (ECMs), a common component in the tumor microenvironment due to elevated profibrotic and integrin signaling [120]. This is consistent with the recent link with YAP1 activity to the induction of an EMT event [121]. The importance of oncogenic YAP1 in driving neoplasia in NF2 deficient neurofibromatosis was demonstrated by pharmacologic inhibition of YAP1 reverting the otherwise rampant tumor growth

in NF2 mutant mice [122]. Pancreatic and lung cancers with overactive KRAS oncogene expression have also been found to have increased YAP1 activity that not only worked cooperatively with KRAS to drive tumorigenesis but that could also allow tumors to escape when treated with anti-KRAS therapies. Multiple studies indicate that activation of YAP1 increases the malignancy of breast cancers. This includes histologic and genomic studies that find that tumors have increased levels of YAP1 mRNA transcript, reduced ratios of phospho-YAP1 over total YAP1, and increased YAP1 in the nucleus in a manner that increased in direct correlation with tumor malignancy [123-125]. Taken together, these data validate the widespread impact of YAP1 activity on tumorigenesis.

1.8. Amot 130 and Amot 80 co-coordinate YAP1 and TAZ subcellular localization

The Angiomotin family of adapter proteins also play significant roles in cell growth control and polarity by integrating the activities of cell polarity proteins with HIPPO signaling [126]. Unlike most Hippo pathway components, Angiomotin proteins do not have obvious *Drosophila* orthologs [127]. The highly conserved Angiomotin family of proteins is comprised of three separate genes, Amot, Amot Like 1, and Amot Like 2 that encode proteins that share a basic architecture comprising the Amot coiled coil homology domain (ACCH) that separates an N-terminal region that binds to YAP1, TAZ, and LATS1 from a C-terminal region that associates with apical polarity proteins [128]. The *AMOT* gene yields two unique splice isoforms that result in the translation of Amot p130 and Amot p80 proteins [129]. Because the Amot p80 isoform lacks the region N-terminal to the ACCH

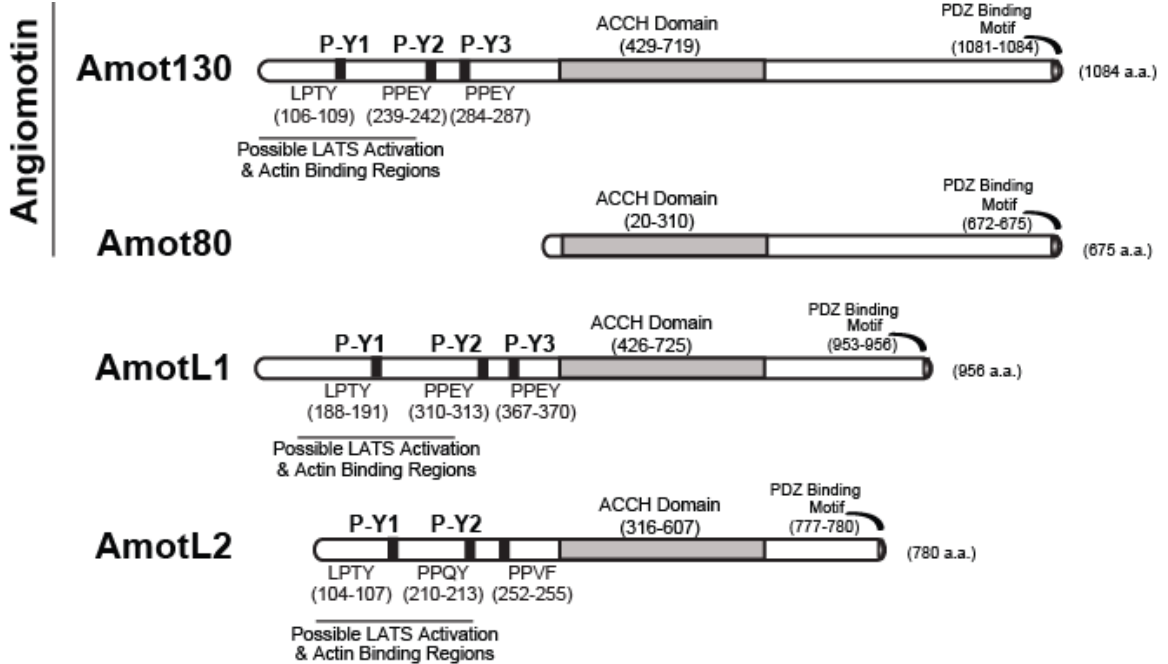


Figure 1-10. A Schematic Diagram of the Angiomotin Family. The Angiomotin family of adapter proteins is derived from three genes: Angiomotin (*AMOT*), Angiomotin Like 1 (*AMOTL1*), and Angiomotin Like 2 (*AMOTL2*). These genes generate four proteins Amot p130, Amot p80, Amot L1, and Amot L2 that share multiple common domains. All four proteins contain an Amot coiled-coil homology (ACCH) domain and a PDZ binding motif. The ACCH domain allows for homodimerization as well as heterodimerization within the Amot family, which has been shown to impact their behavior. The C-terminal PDZ binding motif allows these proteins to associate with other proteins containing a PDZ binding motif. Amot130, AmotL1 and AmotL2 all share N-terminal P-Y motifs that associate with the WW domains of Yap and Taz.

domain, it does not associate with YAP1 or TAZ (Fig. 1-10). In collaboration with Dr. Cristina Ivan (MD Anderson), an analysis of The Cancer Genome Atlas (TCGA) was undertaken that revealed that elevated Amot 130 transcript levels in breast cancer tumors correlate with a poor patient survival hazard ratio 1.13 ($p < 0.01$). This is consistent with reports which found elevated total Amot levels were linked with more aggressive breast tumors of higher grade from patients with a poorer prognosis and reduced survival [130,131]. Additionally, using SAGE tag analysis from K. Polyak, PhD. of the Dana Farber Cancer Institute, we observed that total Amot transcripts were elevated in tumor cells and specifically those with increased CD44 surface expression which is associated with a cancer stem cell signature (Fig 1-11).

Amot 130 is a direct binding partner of YAP1 and TAZ. The first ¹⁷¹WW²⁰⁸ domain of YAP1 associates with the ¹⁰⁶LPTY¹⁰⁹ and ²³⁹PPEY²⁴² domains of Amot p130. It appears that the second WW domain of YAP1, binds selectively to the second PPEY domain of Amot p130. Amot 130 can simultaneously associate with two WW domains of YAP1 (PPEY/WW; LPTY/WW), it only forms an association with TAZ at one domain site (PPXY/WW) [132,133]. This fact, in addition to the functional redundancy between the YAP1 and TAZ coactivators, is mostly responsible for the primary focus of study on the Amot p130 and YAP1 interaction. The highly conserved ACCH domain among the Amot family allows these proteins to heterodimerize with one another [128,134]. The dimerization of Amot130 and Amot 80 greatly impacts the function and localization of Amot 130 which, in turn, affects the trafficking of polarity proteins and YAP1. Amot has

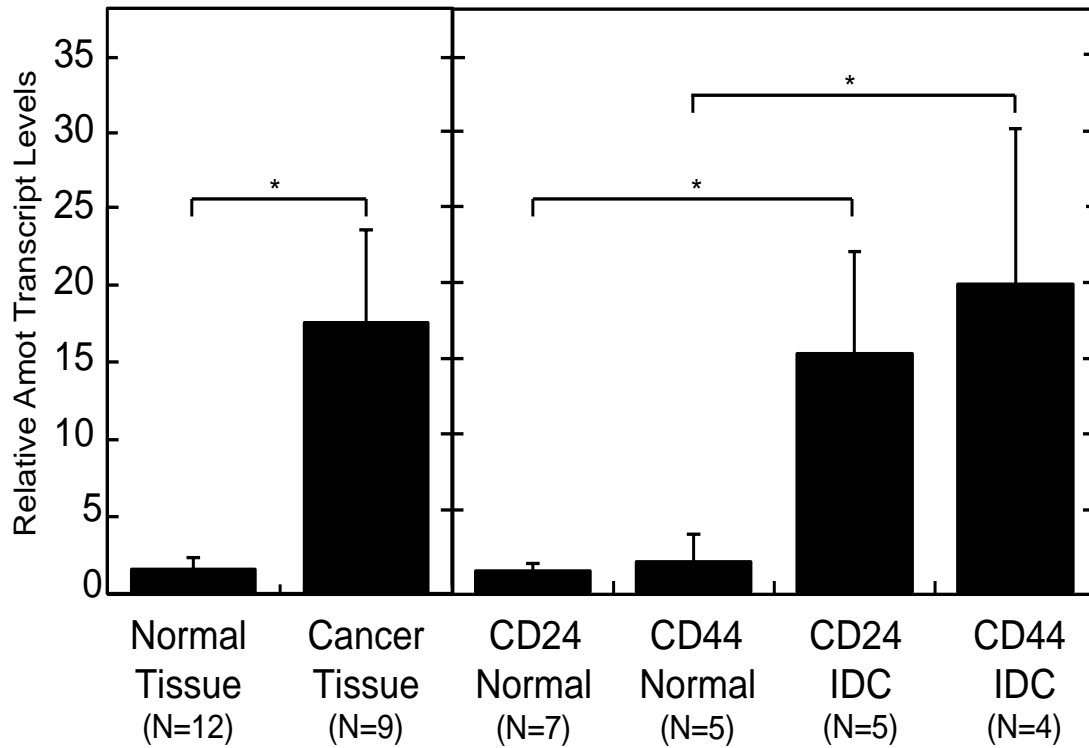


Figure 1-11. The levels of Amot transcripts indicate a potential signature for identifying invasive breast tumors versus normal tissue. In collaboration with K. Polyak (Dana Farber Cancer Institute), the relative levels of transcripts for Amot were determined by SAGE analysis from primary mammary cells derived from normal or invasive cancer tissue following cell sorting on CD24 and CD44 (stem-like) status. Sample size is indicated. SEM. $p \leq 0.05$. Data from K. Polyak, PhD. of the Dana Farber Cancer Institute.

been found to be required for ERK induced growth of breast cancer cells. MCF7 cells infected with a cerulean fluorescent protein (CFP) tagged-Amot 80 plasmid resulted in a 2.2 fold increase in the levels of [³H] thymidine incorporated into nucleic acids as compared to control, indicating a robust enhancement of proliferation. When MCF10A cells overexpressing Amot 80 were cultured in Matrigel®, the resulting mammary acini lacked a hollow lumen and exhibited 4-fold greater cross-sectional area when compared to control cells [13]. Ectopic expression of Amot 130 was found to render mammary acini with reduced cross-sectional area [138], however, in unpublished data from our lab, the coexpression of Amot 130 and Amot 80 resulted in cells that showed enhanced growth and failed to form a polarized acini structure versus control cells. Likewise, total Amot knockdown resulted in cells that lacked any growth in Matrigel® [12]. Taken together, these data suggest that the dimerization of the Amot isoforms is required for YAP1 nuclear translocation and that Amot 80 functions to dominantly redirect the Amot130/YAP1 complex resulting in YAP1 nuclear accumulation.

Amot 130 also inhibits YAP1 by reducing its stability through coupling it to the atrophon 1 interacting protein 4 (AIP4) E3 ubiquitin ligase. This enhances YAP1 ubiquitination and degradation [135]. Importantly, phosphorylation of Amot130 by LATS1/2 is required for Amot 130 to bind both to YAP and to AIP4. Consistent with the phosphorylation of Amot 130 being essential to turn on its anti-YAP1 activity. MCF10A cells expressing a mutated form of Amot 130, (S175A), which cannot be phosphorylated by LATS1/2, exhibited unrestricted cell

growth as compared to cells expressing wild type Amot 130 when grown in Matrigel©. Consistent with this being due to increased YAP1 activity, cells expressing Amot 130 S175A exhibited 1.8-fold increased CTGF transcript levels verses control cells and 3.6 fold greater transcript levels of CTGF than cells expressing WT Amot 130 [136].

While several studies show that the p130 and p80 isoforms of Amot dictate opposing effects on the activity of YAP1/TAZ, very little is understood about how their expression is controlled [133,135-139]. Limited work has found that Amot 130 and Amot 80 are splice isoforms. However, it is possible that they are driven by two separate promoters that lie at different positions in the *AMOT* gene. Thus, the current literature on Amot leaves many questions unanswered. Due to their unique roles within the cell, understanding the expression of Amot requires a deeper investigation of how these two isoforms are differentially regulated.

1.9. The major questions and hypotheses of this work

The work comprising this dissertation seeks to understand the mechanisms that control the expression of Amot in order to better comprehend how breast cancers induce increased levels of Amot in breast epithelial cells to promote the transition from DCIS to IDC. We hypothesize the following: Inflammation in the breast drives a DCIS to IDC transition through the secretion of IL-6 from inflammatory cells in the stroma, which functions to disrupt intracellular polarity by inactivating HIPPO signaling and foster the nuclear

translocation of YAP1 to promote growth. We postulate that the inactivation of HIPPO signaling is not through the kinase component, but through the activated expression of the Amot isoforms. To answer these broad questions, we addressed the following more specific points: 1. Associate the histologic measures of Amot protein levels and subcellular localizations with reports of enhanced levels of Amot transcripts in breast tumors. 2. Define the *AMOT* gene, its regulatory region(s), the promoter elements that control its transcription, and the manner in which the unique isoforms are expressed. 3. Define the impact of inflammatory cytokine induced signaling on Amot expression. 4. Determine the importance of Amot as an effector of inflammatory induced cell dedifferentiation and proliferation. 5. Identify the key factors in inflammatory based signaling that induce Amot transcription.

Our novel hypothesis seeks to illuminate the role of tumor-associated inflammation in driving the loss of intracellular polarity in mammary epithelial cells to facilitate DCIS to IDC transitions. The accomplishment of our aims laid out above will establish the Amot HIPPO adapter proteins as key players in DCIS to IDC transitions. This work has the potential to underlie the use of the Amot proteins as biomarkers to predict DCIS to IDC transitions at the time of a DCIS diagnosis, and perhaps preclude unnecessary surgeries. Moreover, this work may launch anti-Amot drug discovery efforts in the prevention of DCIS to IDC transitions.

CHAPTER 2: MATERIALS AND METHODS

*Please Note: This chapter contains the detailed instructions for the techniques common to multiple chapters within this dissertation. Chapter-specific methods and materials are detailed further within the chapters.

Mammalian Cell Culture

Cell lines were thawed from -80 °C (freezer) and/or -196 °C (liquid nitrogen tank) via incubation in 37 °C for a duration of no more than 5 minutes. Cells were then diluted with 2 milliliters (mLs) of complete DMEM culture media, transferred to a 15 mL conical tube, and then centrifuged at room temperature (R.T.) for 1.5 minutes at 1500 rotations per minute (rpm). The supernatant was removed and cells were re-suspended into 10 mLs of their respective culture medium. The suspended cells were transferred into 10 centimeter (cm) culture plates for stock culture. Michigan Cancer Foundation-7 (MCF7), MD Anderson MetaBlastic-468 (MDA-MB-468), Human Epithelial Kidney 293 Tert-immortalized (HEK 293T), SKBR3, U373, and C2C12 cells were cultured in Complete DMEM (10% FBS, 1% (v/v) penicillin/streptomycin, and Dulbecco's Modified Eagle Medium (DMEM)). Michigan Cancer Foundation 10A (MCF10A) pre-tumorigenic cells were cultured in 250 mLs Hams-F12, 250 mLs DMEM, and supplemented with 50 micrograms/milliliter ($\mu\text{g/mL}$) Bovine Pituitary Extract (BPE) (Hammond, 1078-NZ), 0.5 $\mu\text{g/mL}$ hydrocortisone, 5 $\mu\text{g/mL}$ human insulin, 10 nanograms/milliliter (ng/mL) epidermal growth factor (EGF), and 100 ng/mL cholera toxin. Cells were incubated at 37 °C with 5 % CO_2 (v/v). Cells in culture were monitored at least once every two days, and were split as needed. To split cells grown in culture, the following reagents were prewarmed for a duration of

20 minutes at 37 °C: 1X phospho-buffered saline (PBS), 1X trypsin, Complete DMEM (or respective media). The media of the cells to be split was aspirated and replaced with a warm 2.5 mL PBS wash, which was then aspirated and replaced with 2.5 mL 1X trypsin. Cells were then returned to the 37 °C incubator for a duration of 5 minutes, or until cells had visibly lost adherence. The cell-trypsin solution was then resuspended in Complete DMEM (or respective media) at a 1:1 ratio and transferred into a labelled 15 mL conical tube. The cell solution was centrifuged at room temperature for 1.5 minutes at 1500 rpm. The supernatant was removed and cells were re-suspended at the desired dilution into 10 mLs of their respective culture medium.

Polyethylenimine (PEI) Transfection

DNA was introduced into adherent eukaryotic cells at a ratio of 1 µg of plasmid DNA per 200,000 cells. DNA was diluted into 1 mL of prewarmed serum-free DMEM, and (2µg/mL) polyethylenimine (PEI) was added at a ratio of 0.5 µL PEI per 1 µg of DNA. Once added, the solution was vortexed for 5 seconds and allowed to incubate at ROOM TEMPERATURE for a duration of five minutes prior to adding to a plated of adhered cells. Cells were incubated in transfection media at for 12-18 hours at 37 °C with 5 % CO₂ (v/v).

Lentiviral Transduction

HEK 293T cells were plated at 4 million cells into a 10 cm plate and allowed to adhere overnight prior to transfection with 20 µg of target lentiviral

DNA plasmid, 10 µg of pMDLg-RRE, 6 µg pCMV-VSVG, 5 µg pRSV-Rev, and 25 µL PEI (2 µg/mL). Cells were incubated with transfection medium for a duration of 18 hours, and subsequently replaced with 7 mLs of Complete DMEM to collect secreted viral particles. Virally conditioned media was collected and replaced again with 7 mLs of Complete DMEM every 24 hours for a duration of 2 days. Virally conditioned media was centrifuged at 1500 rpm for 4 minutes and the supernatant was collected. Polybrene (5 mg/mL) was added to viral media at a ratio of 3 µL polybrene: 1 mL viral media. Viral media was stored at 4 °C for no longer than 2 weeks. Prior to infection, target cells were plated at 1 million cells into a 10 cm plate and allowed to adhere overnight. The target cells were then incubated in viral media for a duration of 6 hours. Target cells were then split within 24 hours of the completion of the viral incubation to encourage cell division and expression of the target plasmid. A representative population of infected cells was harvested at least 48 hours after infection to confirm expression via immunoblot.

pGL3 Luciferase Reporter Assays

HEK 293T cells were plated (200,000/well) into a 12 well dish and allowed to adhere overnight. Cells were transiently transfected with 0.25 µg TK-Renilla as a transfection control, and 0.25 µg full Amot, serially deleted Amot, or SP1 motif site-mutated promoter plasmids. Luciferase was allowed to accumulate for a duration of 20 hours before cell lysis (200 µL volume per sample) in Promega Luciferase 5X Lysis Buffer (diluted in water). Samples were processed per

manufacturer's instructions for Dual-Luciferase Reporter Assay System (Promega, TM040). A dual luminometer (BioSystems) was utilized to analyze all samples. Data are presented as average ratios of Firefly luciferase measurements over control Renilla measurements.

Immunoblotting

Proteins were harvested in radioimmunoprecipitation assay RIPA buffer (25mM Tris 7.4, 150 mM NaCl, 0.1% sodium dodecyl sulfate (SDS), 0.5% sodium deoxycholate, and 1X Triton X) quantified using a bicinchoninic acid (BCA) assay, normalized and ran out on and SDS polyacrylamide gel electrophoresis (SDS-PAGE) in running buffer at 100 volts until the dye front reached the bottom of the gel. The proteins in the gel were transferred onto a 0.45 micron nitrocellulose membrane (Protran) in transfer buffer at 24 volts for a duration of 45 minutes. The transferred membrane was then probed with primary antibody overnight at 4 °C (Table 2-1) and anti-rabbit or anti-mouse secondary antibodies (Odyssey) diluted 1:50,000 for a duration of 30 minutes at room temperature. All primary and secondary antibodies were diluted in tris-buffered saline with Tween (TBST). The membrane was then imaged on a Licor imager.

Table 2-1. Primary antibodies used in the immunoblots within this dissertation.

Primary Antibody	Antigen(s) Detected	Obtained from	Dilution (in TBST)
476 Final Bleed; Affinity Purified; α -Rabbit	Amot p130; Amot p80	Wells Lab Custom Antibody	1:1000
Yap1; α -Mouse	Yes Associated Protein 1	Abnova H00010413-MO1	1:1000

Phospho-Yap; α -Rabbit	Yap1 Ser127	Cell Signaling, 4911S	1:1000
Taz; α -Mouse	Transcriptional co-activator with PDZ-binding motif	BD Biosciences, 560235	1:1000
Stat3; α -Mouse	Signal transducer and activator of transcription 3	Cell Signaling	1:1000
Phosph-Stat3; α -Rabbit	Stat3 Tyr705	Cell Signaling	1:1000
LATS 1; α -Rabbit	Large Tumor Suppressor 1	Bethyl, A300,-477A	1:1000
Phospho-LATS 1; α -Rabbit	LATS1 Ser909	Cell Signaling, 9157S	1:1000
Sp1; α -Mouse	Specificity Protein 1	Santa Cruz	1:1000
GAPDH; α -Mouse	Glyceraldehyde 3 phosphate dehydrogenase	Millipore, MAB374	1:20,000
M2; α -Mouse	Flag Tag	Sigma, F3165	1:10,000

RNA Extraction

The media from cells to be extracted was aspirated and replaced with a 1 mL PBS wash, and then again was aspirated. Cells were then treated with Tri-Reagent LS (Sigma) at a ratio of 500 μ L per 1 million cells and the solution was transferred to a labelled 1.5 mL microcentrifuge tube. The cell solution was allowed to incubate at room temperature for 5 minutes before the addition of 200 μ L of chloroform. Tubes were vortexed and centrifuged at a rate of 14,000 rpm at 4 °C for 10 minutes. The upper aqueous phase containing RNA was transferred to a fresh microcentrifuge tube and diluted 1:1 in isopropanol. Tubes were vortexed and centrifuged at a rate of 14,000 rpm at 4 °C for 10 minutes. The supernatant was discarded and the pellet containing RNA was washed twice in

70 % ethanol; a centrifugation step at a rate of 14,000 rpm at 4 °C for 10 minutes proceeded each wash. Once the final supernatant was discarded, the pellet was allowed to dry at room temperature for a duration of 5 minutes. The RNA was then diluted in 30 µL of deionized water and the concentration (ng/mL) was measured via Nanodrop®.

Complementary DNA (cDNA) synthesis

Freshly extracted RNA was employed to synthesize complementary DNA (cDNA). A recipe including 5 µg RNA, 2 µL oligo deoxy-thymine (oligo dT) (for the amplification of regions near the 3' end of the gene product) or random hexamers (for the amplification of all other regions of the gene product), and 4 µL deoxy-nucleoside triphosphates (dNTPs) risen up to a total volume of 24 µL was incubated at 65 °C for a duration of 5 minutes. The following reagents were then added to the solution: 10 µL ddI water, 4 µL 10X reverse transcriptase buffer, 2 µL Superscript II reverse transcriptase. Tubes were then incubated at 50 °C for a duration of 1 hour. The concentration of the resulting cDNA was measured via Nanodrop®. Sample concentrations were normalized to a standard of 300 ng/mL.

Quantitative Real Time-Polymerase Chain Reaction (qRT-PCR)

Primer sets were designed to satisfy requirements for PCR with SYBR green polymerase, with melting temperatures between 59 °C-61 °C and amplicon lengths between 70-150 base pairs. These primers were then diluted to a concentration of 100 µM stock stored at -20 °C, with a working stock

concentration of 10 μ M stored at 4 °C. The recipe for each PCR reaction required 5 μ L cDNA (300 ng/mL), 10 μ L 2X SYBR Green Master Mix (BioLine), 1 μ L forward and 1 μ L reverse primers (10 μ M) and 3 μ L ddI water. Reactions were plated into a 96 well clear PCR plate, covered with a clear adhesive film, and centrifuged 4000 rpm at 4 °C for 10 minutes. The plate was then loaded into the Realplex2 Gradient Mastercycler (Eppendorf). All crossover threshold values of target genes were normalized to GAPDH or 18S ribosomal RNA.

Fixed Cell Imaging

Cells (200,000) were plated on acid washed glass coverslips coated in fibronectin and collagen distributed in 12 well plates (Corning) and allowed to adhere overnight. Media was removed and cells were harvested in a 4% paraformaldehyde (PFA) wash for a duration of 5 minutes at 4 degrees Celsius. Slides were then incubated at 4 degree C in blocking buffer (5% bovine serum albumin/0.2% saponin in PBS) for a duration of 1 hour. Coverslips were incubated in YAP1 anti mouse primary antibody (Abnova) diluted between 1:1000 in blocking buffer for 1 hour and in 488 anti-mouse secondary antibody (Alexa Fluor) diluted 1:500 for 30 minutes (in the dark). Slides were rinsed in blocking buffer and DDI before removal from the 12 well dish, flipping over and placed onto a glass slide covered in ProLong Gold mounting media. Slides were allowed to dry overnight in the dark prior to imaging.

Fluorescent Microscopy

Epifluorescent images were acquired using structured light via an Apotome on a Zeiss Axio ObserverZ1. This technique is described in greater detail in Chapter 3 of this dissertation.

Quantification of Immunofluorescent Imaging

Zen image processing software (Zeiss) was used to quantify the average pixel area and intensity per nuclei of each antigen. Tissue structures were isolated and quantified, thereby eliminating the hollow lumen from the calculation.

Analysis of The Cancer Genome Atlas (TCGA)

Level 1 TCGA analysis was completed by Dr. Cristina Ivan at University of Texas MD Anderson Cancer Center of Houston, TX, which provided us the correlations of Amot transcript levels to its corresponding hazard ratio and the breast tumor associated transcripts in over 700 breast tumor tissue samples. Raw data was analysed and compiled into graphic form in Microsoft Excel. The results shown here are in whole or part based upon data generated by the TCGA Research Network: <http://cancergenome.nih.gov/>.

Statistical Analysis

Statistical analysis was completed using Microsoft Excel software. Precision was displayed as either standard deviation (S.D.) or standard error (S.E.M.). S.D. was used unless a high sample size called for the use of a

weighted mean, in which S.E.M. was employed. Significance was tested using a two-tailed, two-sample of unequal variance Student's t-test. A significance threshold was maintained at $p < 0.05$.

**CHAPTER 3: LED PHOTBLEACHING REDUCES AUTOFLUORESCENCE
AND ENHANCES ANTIGEN RETRIEVAL OF PARAFFIN EMBEDDED HUMAN
BREAST TISSUE SECTIONS**

3.1 Prologue

The first point to address in our project was to associate the histologic measures of Amot protein levels and subcellular localizations with reports of enhanced levels of Amot transcripts in breast tumors [132]. Therefore, we set out to investigate the levels and subcellular localization of the Amot proteins in human breast tissue samples. The decision to use fluorescence based detection methods held the promise of several advantages including: A) the ability to image multiple antigens per slide, B) the ability to quantify signals for each channel with little interference from other channels, C) the much greater sensitivity of fluorescence detection verses standard IHC based methods, and D) the ability to image multiple planes of the same field in the form of a Z-stack. However, a barrier for analyzing samples using fluorescent methods was the significant autofluorescence detected in archival paraffin embedded tissues following standard fixation and permeabilization methods. To overcome this, we innovated a cost and time efficient technique to degrade the high degree of autofluorescence commonly associated with human mammary tissue.

3.2 Introduction

The ability to define the concentration and 3-dimensional localization of multiple antigens in a common tissue sample would allow a much deeper understanding of the molecular changes that associate with breast cancer formation and progression. Immunofluorescent (IF) labeling has the potential to be a superior method to standard immunohistochemically (IHC) techniques that

are mainly used by pathologists (Table 3-1) [140,141]. IHC became the standard method for labeling breast cancer markers in biopsies in 1999 after succeeding the use of ligand binding biochemical assays. The IHC method proved more specific and better able to analyze samples of smaller volume [142,143]. Additional technological innovations have since been made in the field of fluorescence microscopy to overcome the limitations of IHC. For instance, IHC is confined to analyzing a single antigen in 2-dimensions. IHC labeling also prohibits the isolation of antigen staining from hematoxylin and eosin (H&E) staining, resulting in an increased difficulty in the quantification of antigen levels. This also prohibits the study of multi-antigen association and co-localization in tissue samples [144]. In contrast, immunofluorescent (IF) labeling allows the imaging of multiple antigens in a single sample simultaneously due to the ability to detect each antigen using a different excitation and emissions spectra. This provides for the determination of the localization of multiple antigens in relation to each other. Additionally, the detection via different emission spectra also allows for the ability to view and quantify isolated images of each distinct antigen [145]. Despite all of the advantages of IF staining, this technique presents distinct complications, particularly when it is applied to the analysis of para-formaldehyde (PFA)-fixed tissue sections. Because the overwhelming majority of archival tissue is fixed with PFA, it is vital to develop analysis methods that are compatible with PFA fixation [146]. However, this embedment technique generally results in significant autofluorescence between the wavelengths of 450-550 nm [147,148].

Table 3-1. Comparison of the advantages and disadvantages between different antigen staining techniques.

	Immunohistochemical Staining	Immunofluorescent Staining (Epifluorescent Microscope)
Total Number of Simultaneous Antigen Detection	1	3
Capable of 3-Dimensional Imaging?	No	Yes
Capable of single antigen distinguishable quantification?	No	Yes
Autofluorescence resulting in high background	No	Yes

Autofluorescence refers to the inherent and nonspecific fluorescent spectra emitted from organic tissue. This results from naturally occurring, fluorescence-emitting protein structures, tissue components, and embedment in aldehyde fixatives [147,149-155]. Degrees of autofluorescence varies between different types of tissues. Autofluorescence is caused by many sources including lipofuscins, collagen, flavins, reticulin fibers, elastin, NAD(P)H, and proteins with high concentrations of tyrosine, tryptophan, and phenylalanine, all emitting natural fluorescence at varying wavelengths [155]. There are a number of organic properties that contribute to the ability of a molecule to reflect and/or refract light, including: the presence of electron donating groups, aromatic rings, chiral centers, and compounds that contribute to peroxide formation [156, 157].

Tissue-type specific differences in metabolic rates-with regard to co-enzymatic redox carrier activity (flavins, NADPH), red blood cell (RBC) concentration and degradation rates, (lipofuscins), and stromal structure can result in significant autofluorescence [157].

Autofluorescence becomes a major impediment to imaging tissues as it clouds the ability to distinguish the signal emitted from a labeled antigen from the fluorescence-emitting components in the tissue. Additionally, as tumor cells possess elevated metabolic rates and thus increased concentrations of flavins and NADPH, the degree of tumorigenicity also dramatically contributes to autofluorescence. Particularly in mammary tissue, autofluorescence has long been used as a clinical tool for detecting tissue malignancy, as tumor tissue composition differs drastically from that of benign tissue [79,156].

Many techniques have been developed as single remedies to reduce the level of autofluorescence in tissues for the purpose of IF antigen detection. Such methods include short wave ultra-violet (UV) photobleaching, chemical treatments, digital background reduction, and image processing methods by confocal laser imaging [151-155,157,158]. However, we found that these methods were either ineffective in our samples, were highly damaging to the tissue, or required imaging equipment that is outside of the budget of most biomedical research laboratories. We therefore set out to find methods to combat autofluorescence in mammary tissue that could be applied to epifluorescence-based focal imaging.

The autofluorescence of mammary tissue occurs predominantly between 400 and 500 nanometer wavelengths. This greatly impedes the imaging of these tissues in the green fluorescent protein (GFP) channel, a key excitation and emission spectra used for epifluorescence-based imaging. Methods to reduce this autofluorescence such as long term exposure to short-wave UV photobleaching has the deleterious effect of damaging the tissue structure. Chemical pre-treatments such as sodium borohydride, which is reported to reduce autofluorescence of several types of tissues [159], in our hands was ineffective and has been reported by others to enhance autofluorescence in mammary tissue (Fig 3-1). Confocal laser image processing cannot be applied to standard epi-fluorescent imaging microscopes.

After analyzing the absorption and emissions spectra of autofluorescing compounds in mammary tissue, we realized that they mainly absorbed around 450 nm. Further, the recent development of light emitting diodes (LEDs) that emit with high intensity and low heat at this wavelength suggested that they may be appropriate for photobleaching mammary tissue with minimal tissue damage. This initial series of observations and research resulted in the development of a simple, rapid, and inexpensive method of mammary tissue immunofluorescence staining that focuses on: 1. Reducing mammary-tissue specific autofluorescence; 2. minimizing residual background signals via long-wave LED photobleaching and optimized epi-focal image processing.

3.3. Materials, Methods, and Results

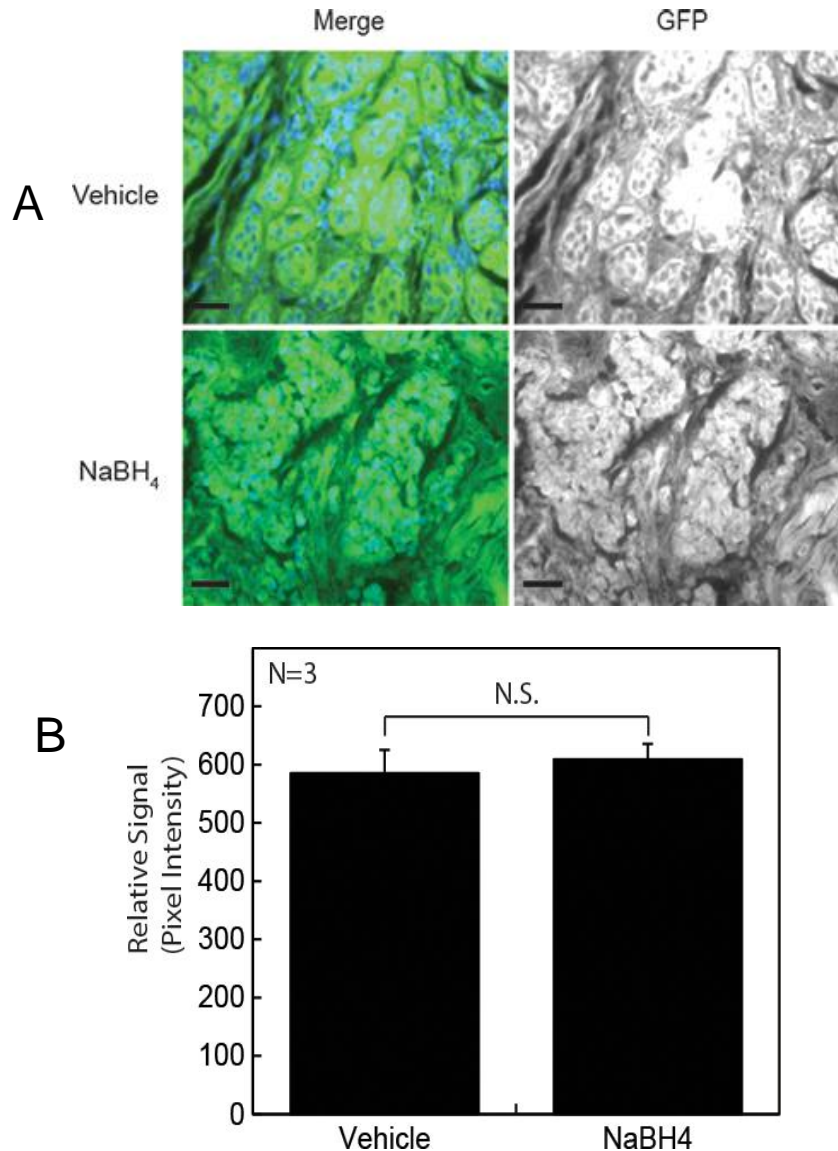


Figure 3-1. Exposure of mammary tissue sections to sodium borohydride had no effect on autofluorescence reduction. A. Mammary tissue sections were subjected to treatment with 10 mM NaBH₄ for a duration of 24 hours prior to deparaffinization and then stained with Hoescht dye. Fluorescent epifocal imaging of each section was performed using the 40X W objective and a constant exposure time of 1S in the GFP channel. B). Zen immunofluorescent quantification software was used to analyze the average GFP channel mean intensity normalized to the number of nuclei. N=3; Standard Deviation; $p < 0.01$.

Tissue Sections

Tissue sections were PFA-fixed 5 µm thick sections mounted onto glass slides. We acquired malignant mammary tissue sections from the IUSM Simon Cancer Center. Additionally, we acquired 60 slides from fourteen blocks of the IUSCC Tumor MicroArray. This was compiled by members of the breast cancer working group.

Slide Processing

After testing multiple durations, it was determined that the optimal conditions were a 24 hour exposure of tissue slides to a 90W industrial blue wavelength) LED light (LED Wholesalers) with a 1980 luminous flux intensity at a distance of 0.5 centimeters (cm) from the light source on a foil background (Fig 3-2). While this was carried out at room temperature, the temperature on the slide surface was 65°C. This long treatment with relatively low heat visibly melted the paraffin and as discovered below is thought to also contribute to better antigen retrieval.

Deparaffinization and Rehydration:

Sections were treated with xylene for a duration of 5 minutes and then rehydrated with two 3-minute washes of 100%, 95%, 80%, and 70% EtOH solutions and finally rinsed three times with ddH₂O.

Antigen Retrieval, Blocking, and Antibody Staining:

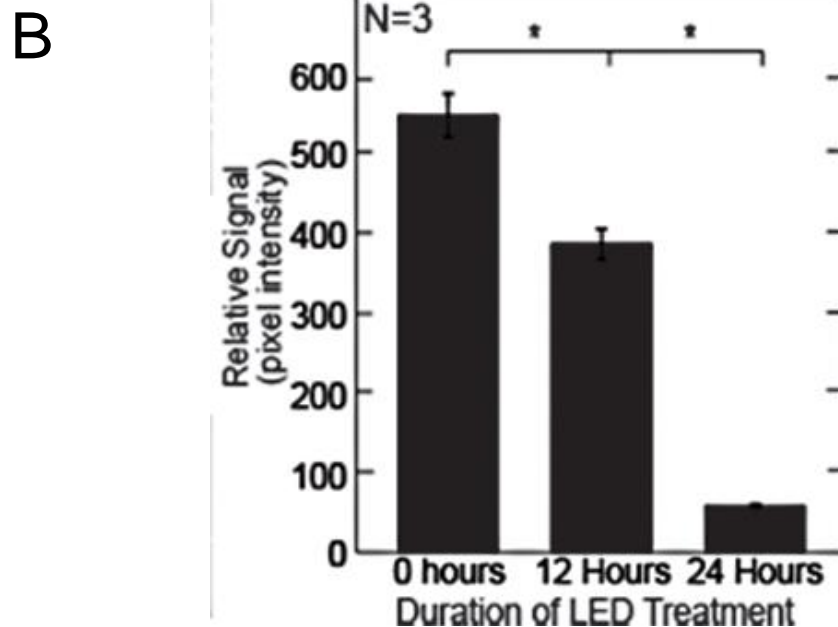
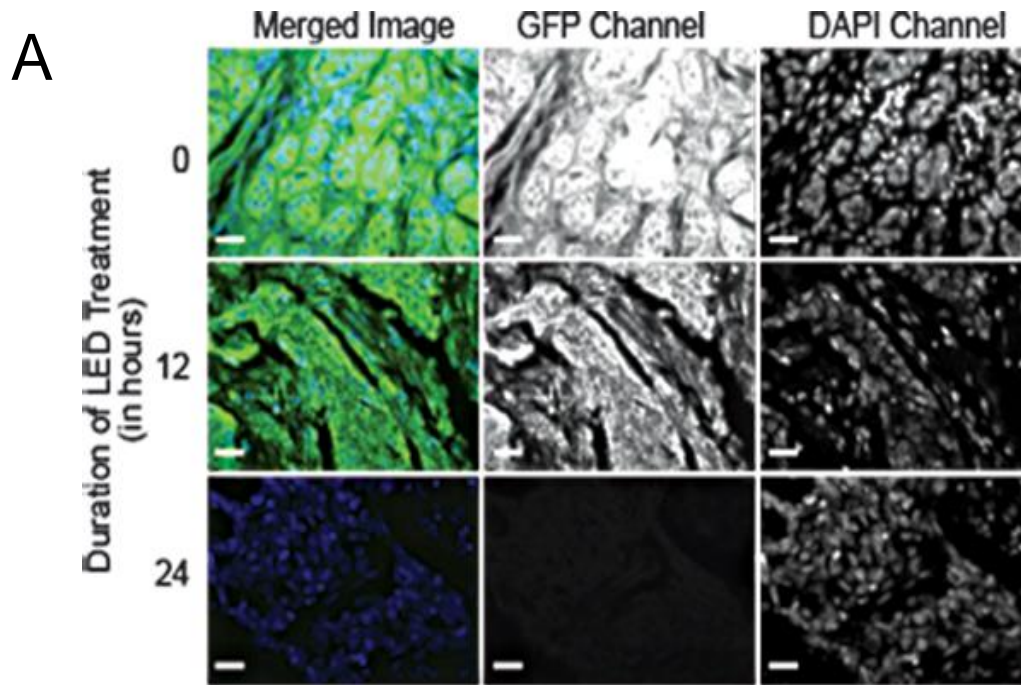


Figure 3-2. Exposure of mammary tissue sections to 452 nm LED light reduces autofluorescence in the GFP channel. Mammary tissue sections were subjected to 0, 12, and 24 hr exposures to 452 nm LED light and then stained with Hoescht dye. A). Fluorescent epifocal imaging of each section was performed using the 40X W objective and a constant exposure time of 1S in the GFP channel. B). Zen immunofluorescent quantification software was used to analyze the average GFP channel mean intensity normalized to the number of nuclei. N=3; Standard Deviation; $p < 0.01$.

Sections were subjected to a 20 minute 10 mM $\text{Na}_3\text{C}_6\text{H}_5\text{O}_7$ boil using a 1100 watt, 2450 MHz microwave (Whirlpool) at full power, with intermittent pauses every 2 minutes to replace the displaced solution with ddH₂O. Sections were then placed in a 5.0 % / 0.01 % bovine serum albumin (BSA) / saponin phosphor-buffered saline (PBS) blocking buffer solution for one hour at room temperature. In addition the 24 hour heating of the sample to 65 degrees produced by the LED at the slide surface was found to reliably enhance the specific signal from the antigen and it is therefore postulated to enable antigen retrieval. This matches our findings and the findings of other groups that have shown that heat disrupts aldehyde cross-linking that can block epitope availability (Fig. 3-3) [160]. Slides were then incubated in primary antibody (Table 3-2) diluted in blocking buffer for 1 hour at room temperature and in anti-rabbit or anti-mouse 594 or 488 nm secondary antibodies (Alexa Fluor) diluted 1:500 for 30 minutes (in the dark). Nuclei were underwent a 9 minute incubation in Hoescht dye diluted 1:3000 in blocking buffer. Slides were then rinsed in blocking buffer and DDI before drying in the chemical hood for 5 minutes. Once dry, glass coverslips were adhered to the slides using ProLong Gold mounting media. Slides were allowed to dry overnight in the dark prior to imaging.

Table 3-2. Primary antibodies used in immunofluorescence staining in Chapter 3.

Primary Antibody	Antigen(s) Detected	Obtained from	Dilution (in Blocking Buffer)
475 Bleed 2 Affinity Purified; α -Rabbit	Amot p130; Amot p80	Wells Lab Custom Antibody	1:500
B-Catenin; α -Mouse	B-Catenin	BD Biosciences,	1:1000
9E10; α -Mouse	Myc	Cell Signaling, 2272S	1:10,000

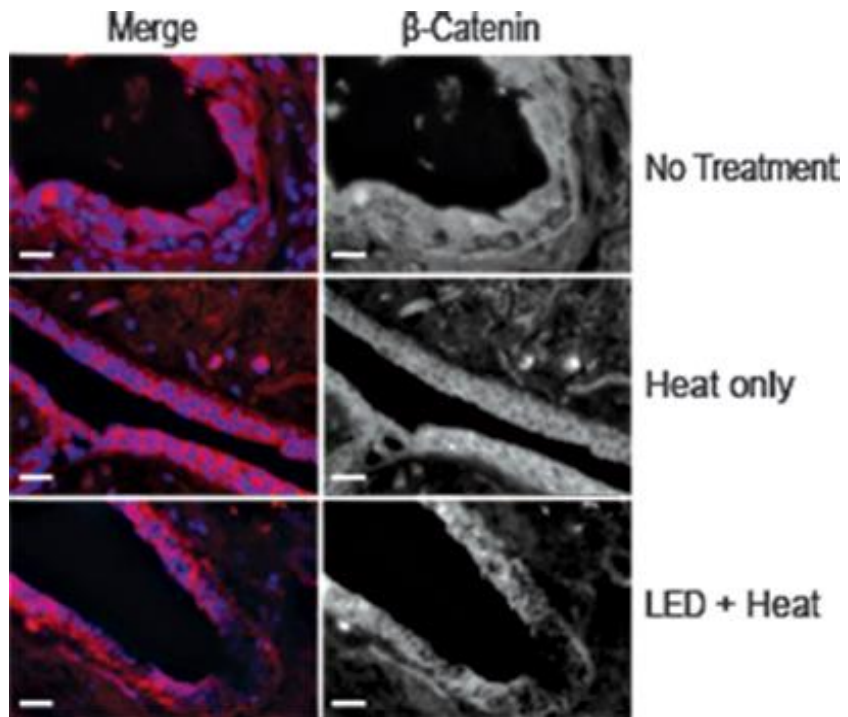


Figure 3-3. The heat produced from the LED light functions to enhance antigen retrieval of human mammary tissue. Mammary tissue sections were subjected to 24 hr exposures to either 65°C heat or 452 nm LED treatments and then immunolabelled for β-catenin to demonstrate effects on antigen specificity.

Microscopic Imaging:

All imaging was carried out using a 4 objective, 6-filter enabled Zeiss AxiObserver Microscope with epifluorescence capabilities. The capochromat 40X water immersion objective was used for image acquisition. Filter sets and fluor combinations consisted of the high efficiency YFP, DsRED, and DAPI filter sets. Confocal-like imaging was acquired using an apotome attachment (Fig 3-4; 3-5)

Image Quantification:

Mean average signal intensity was quantified using the Zen image quantification software packages, an accompaniment to Zeiss Axiovision image acquisition software. Mean average pixel intensity was used to measure protein expression in the tissues. The number of nuclei present in each analysis field were counted by hand. Mean average signal intensity values were the normalized to the number of nuclei present in the measured area.

Statistical Analysis:

Immunofluorescent average signal intensities normalized to number of nuclei were presented as the means \pm S.D. P-values were calculated by an unpaired two-tailed *t*-test. A significance threshold was maintained at $p < 0.05$.

Optimization of custom Wells Lab Amot antibody for IF:

The antigen specificity of custom Wells Lab Amot antibody (475 Bleed 2; affinity purified (475 B2 AP) was first tested via overexpressing the MYC-tagged

Amot in fixed-cell IF imaging. A MYC-tagged construct containing the insert coding for Amot or an empty insert was transfected via PEI into MCF7 cells that were cultured on glass coverslips. After an 18 hour incubation in transfection media, coverslips were fixed via incubation in a 4 % PFA solution at 4°C for a duration of 5 minutes. This was followed by three 5-minute PBS washes and a 1-hour long incubation in blocking buffer at room temperature. Coverslips were then incubated with a primary antibody solution containing MYC (dilution 1:10,000) and 475 B2 AP at the following dilutions: (1:100, 1:250, 1:500, and 1:1000). The corresponding imaging experiment compared the staining of the MYC antibody to the Amot antibody and found that the IU 475 B2 AP antibody against Amot was specific to the Amot protein and that the optimal dilution for use with IF protocols is 1:500 (Fig 3-4A) (other dilutions not shown). Epitope blocking experiments were employed to validate the specificity of antibodies for their indicated antigen. Epitope blocking involves incubating the antibody with protein constituting the epitope originally used to create the antibody at a 1:1 ratio for a duration of 4 hours. This solution, or a vehicle solution containing a control epitope, was then applied to the tissue section, replacing the primary incubation step in the protocol above. The corresponding imaging experiment compared the staining of the epitope blocked antibody to that of the control in order to determine viable antigen specificity of each antibody (Fig 3-4B).

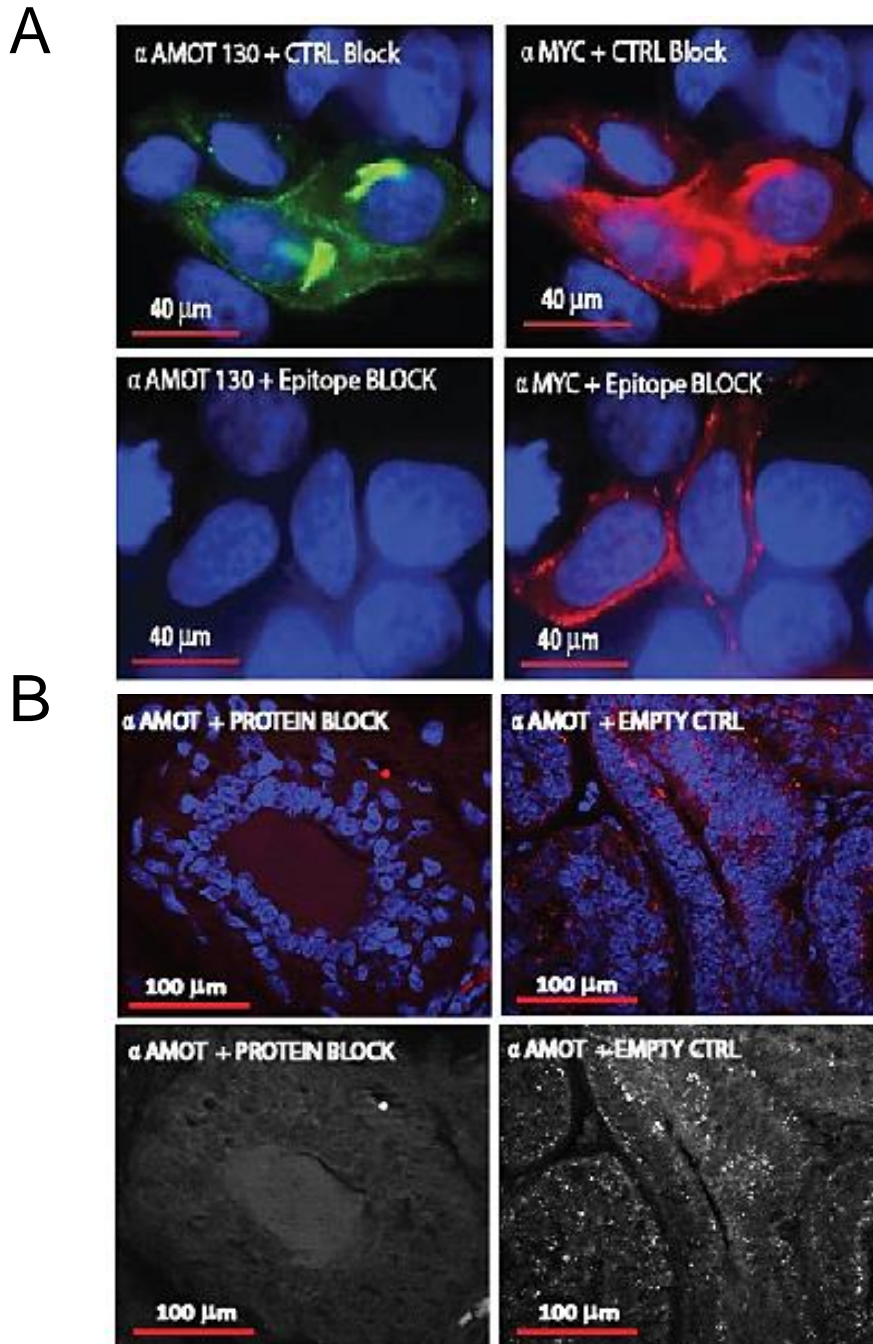


Figure 3-4. The Wells lab custom Amot antibody selectively binds the Amot-specific epitopes. A. A rabbit polyclonal antibody raised against Amot was affinity purified and used to probe breast cancer cells expressing a myc-tagged Amot 130 construct. Co-staining of anti-Myc and Anti-Amot antibodies shows the specificity of the anti-Amot antibody. B. The Amot antibody was incubated with a 5-fold excess of purified antigen or control block prior to staining human breast tumor tissue.

3.4. Discussion

LED exposure reduces autofluorescence of mammary tissue that was primarily seen between 450-510 nm. Sections subjected to LED exposure at durations varying between 0 and 24 hrs were stained for nuclei without antigen retrieval and imaged. A reduction of the autofluorescence in the 488 nm channel are clearly seen between the photobleached and non-photobleached samples (Fig 3-2A). Consistently, the mean average intensity showed a direct negative correlation with the length of LED exposure (Fig 3-2 B).

Residual green and red autofluorescence is virtually undetectable with the use of longer wavelength filters. In addition to the autofluorescence reduction resulting from the LED exposure, residual autofluorescence can be eliminated by using the high efficiency (HE) 526/594 yellow fluorescent protein (YFP) / far red (DsRED) filter sets verses 488 green fluorescent protein (GFP) / 456 texas red (TR) filter sets. The HE 526/594 filter sets also eliminate any bleed-through between channels.

Combining a 24hr LED exposure and imaging with 526/594 filter sets resulted in highly specific immunofluorescent imaging of normal and triple negative mammary tumor sections. These sections following exposure to a 24 hr LED treatment, were deparaffinized and labelled with a mouse monoclonal antibody against Beta-Catenin and the IU 475 bleed 2 AP rabbit polyclonal antibody using the protocol described above. Beta-Catenin (green), Amot (red), and nuclei (blue), can be seen to distinctly localize at cell junctions, punctae, and nuclear structures respectively (Fig 3-5). Thus, three channels were able to be

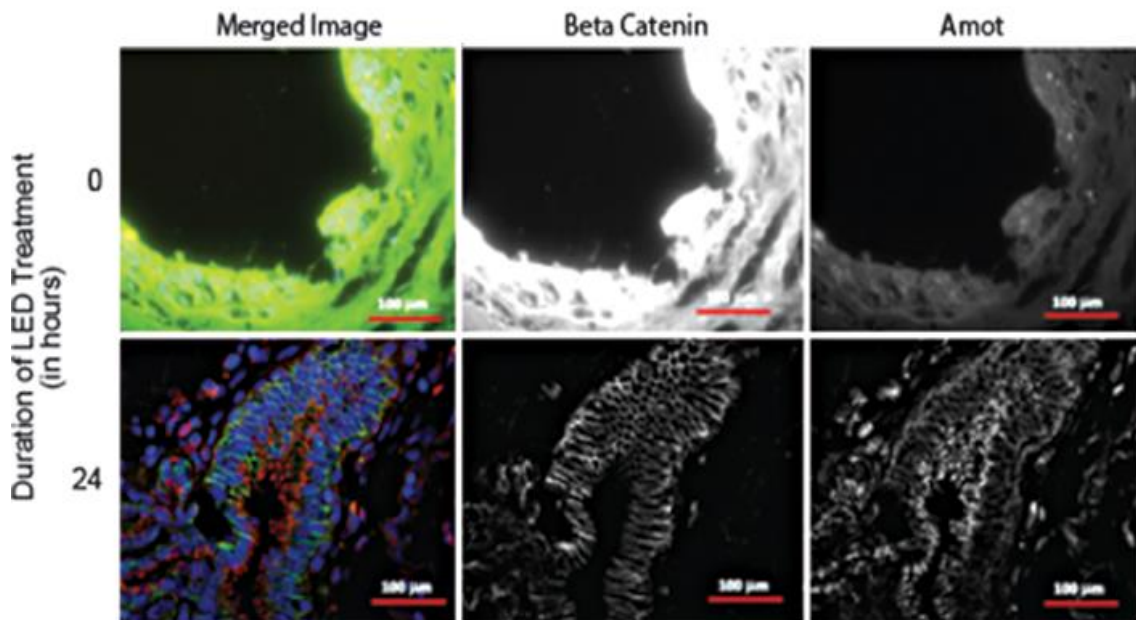


Figure 3-5. LED photobleaching reduces mammary tissue autofluorescence at an optimized duration of 24 hrs. Mammary tissue sections were exposed to a photobleaching treatment with a high intensity blue (single wavelength at 450nm) Light-Emitting Diode (LED) semi-conductor light source for an optimized duration of 24 hrs prior to the de-paraffinization and compared to a no treatment control. Both treated and untreated sections were then immuno-labeled with Amot α -Rabbit (Wells Lab 1:500) and β -catenin α -Mouse (Cell Signaling 1:1000) primary antibodies, Alexa 546 TR α -Rabbit 488 α -Mouse (Invitrogen 1:500) secondary antibodies. Nuclei were stained with Hoescht (1:500). All labels were diluted in blocking buffer (PBS/5% BSA/1% saponin). The three fluorescent signals were each excited with the Zeiss epifluorescent YFP, DsRed, and DAPI filter sets.

imaged simultaneously using epifocal imaging, with antigen specificity that is only comparable to that of confocal imaging. This comprehensive method opens up wide possibilities for breast cancer groups that are limited to epifocal microscope immunofluorescent imaging. The ability to examine up to three fluorescent channels simultaneously can give us substantial insight in many aspects of protein behavior in normal versus tumorigenic human mammary tissue.

CHAPTER 4: AMOT EXPRESSION IS HIGHEST IN BREAST TISSUE THAT IS UNDERGOING A TRANSITION FROM DCIS TO IDC, AND OCCURS IN MULTIPLE SUBCELLULAR LOCALIZATIONS

4.1. Introduction

In 2006, Jiang *et al.* connected the levels of mRNA transcripts of Amot family members with clinical features and outcomes of breast cancer tissue in which they were measured. The transcripts analyzed included *TOTAL AMOT*, *AMOT L1*, and *AMOT L2*. This study was the first to identify that elevated *TOTAL AMOT* (Amot 130 and Amot 80) transcript levels significantly associated with higher tumor grade, increased metastasis of breast cancers, and poor survival. In addition, Lv *et al.* 2015 found consistent results through immunohistochemical (IHC) analysis. The comparison of normal breast tissue to breast tumor tissue by quantitative real time PCR (RT-PCR) revealed a nearly 3-fold elevation in *AMOT* mRNA levels in the tumor tissue ($p \leq 0.05$) when compared to normal breast tissue. The transcript levels of *AMOTL1* and *AMOTL2* showed no correlation with tumor tissue verses normal or with any clinical features of particular tumors.

The comparison between histological subtypes ductal and lobular carcinoma *in situ* (DCIS and LCIS) yielded in a nearly 2-fold elevation of *TOTAL AMOT mRNA* in DCIS tissue. The significance here lies in the passive nature of LCIS; for it is defined simply as the abnormal growth of cells in the lobules of the breast and is therefore classified clinically as benign. That Amot levels were found to be higher in DCIS tissues over LCIS tissues further demonstrates the correlation between Amot expression and breast malignancy [226, 254]. Moreover, *AMOT* mRNA levels also exhibited a 2-fold increase in the more aggressive node positive tumors over node negative tumors ($p \leq 0.01$) [130]. And finally, the comparison between grades I, II, and III breast tumor tissues (Tab 4-

1) by RT-PCR found the greatest elevation of *TOTAL AMOT mRNA* levels (>2-fold) in grade II breast tumors ($p \leq 0.01$), and a moderate (~1.3-fold) elevation in grade III breast tumors ($p \leq 0.05$) when compared to grade I breast tumors. These findings raise the theory that the increase in Amot levels drives early phases of tumorigenic progression from low grade tumors to higher grade, more aggressive breast tumors.

Table 4-1. Clinical features of breast tumors grades I-III.

Grade	Clinical Features
I	Well differentiated cell structure; Highly epithelial
II	Moderately differentiated cell structure
III	Poorly differentiated cell structure; Highly mesenchymal

Through IHC, Lv *et al.* found a strong correlation between Amot and the proliferation marker Ki67, indicating that Amot is elevated in proliferating tumor cells. These investigators also saw an increased staining of Amot protein in breast cancer tissues when compared to non-malignant adjacent tissues [131].

Jiang *et al.* also saw a association between decreased survival and elevated *AMOT* mRNA levels. The survival of patients was nearly 50 % less than mean survival if their tumors showed a 2 fold increase in *AMOT* mRNA levels ($p \leq 0.01$). Relating *AMOT* mRNA levels to 10-year clinical outcome data yielded a significant correlation ($p \leq 0.03$) between elevated *AMOT* mRNA levels and metastasis (>2-fold), whereas no significant correlation occurred between *AMOT* mRNA levels and local recurrence or breast cancer-related death. Kaplan-Meier

survivorship curves demonstrated that tumors from patients that exhibited high levels of *AMOT* mRNA correlated with a 12% reduction in survival compared to tumors from patients that possessed low levels of *AMOT* mRNA. In addition, the relation of *AMOT* mRNA levels to estrogen receptor (ER) status found no significant difference in *TOTAL AMOT mRNA* levels between ER – and ER + breast tumors.

Based on these data, the investigators in Jiang *et al.* have proposed that increased levels of *TOTAL AMOT* mRNA independently indicate high tumor aggressiveness, poor patient survival and a high risk of metastasis [130]. As the field has demonstrated a wide divergence in the many functions of the Amot proteins with respect to tumorigenicity, and that the function of these proteins predominantly depends on cellular polarity status and protein localization, there is great importance in studying the expression, localization, and cellular context of Amot in breast cancer tissues. The best method for executing this type of analysis is the immunofluorescent (IF) staining of human breast tissue samples.

4.2 Methods

The tissues used for this study included: (1) normal mammary ductal epithelial tissue samples from ten healthy female volunteers that were embedded in paraformaldehyde and sectioned (5 μ m) onto glass slides by the IU Simon Cancer Center (IUSCC) at University Hospital in Indianapolis, IN. Slides from a block of a tissue microarray (TMA) compiled by the IUSCC consisting of surgically excised tumors from 451 patients representing a wide variety of breast

cancer subtypes, grades, median 10.3 year patient follow-up data. The block we acquired contained 56 breast tumor core samples. All 56 samples were stained and imaged, and 24 were found to contain viable tissue. The remaining 32 core samples either were highly concentrated in stromal and adipose tissue with very few examples of epithelial tissue, or possessed damage from microtome sectioning.

Slides were processed, stained, imaged, and quantified using the protocols detailed in Chapter 3 section 3 (pages 47 - 48) of this dissertation. Images were acquired using the following channel specific exposure times: DsRed (λ 594 nm), 1000 milliseconds, YFP (λ 488 nm) (1000 milliseconds), DAPI (λ 350nm), variable as needed (between 10-30 milliseconds). Representative images were compiled and cross-referenced with histological and 10 year patient follow-up data.

4.3. Results and Discussion

Tumors from twenty-four breast cancer patients consisted of five grade I tumors, eleven grade II tumors, and eight grade III tumors. According to immunohistochemical staining, four tumors stained negative for the expression of estrogen receptor (ER), and seven were negative for the expression of progesterone receptor (PR). The human epidermal growth factor receptor 2 (Her2) status for all twenty-four samples were found negative via fluorescence *in situ* hybridization (FISH) analysis (Table 4-2).

Table 4-2. Characteristics of the patient samples studied in this cohort. Tumor grade (I-III and hormone receptor status (ER-estrogen receptor/PR-progesterone receptor) of tumor samples from the twenty-four patients analyzed in this study cohort obtained from IU Simon Cancer Center. Note: all tumor samples are negative for human epidermal growth factor receptor 2 (Her2).

Tumor Grade	Hormone Receptor Status
I	ER+ / PR- / Her2- ER+ / PR+ / Her2-
II	ER+ / PR- / Her2- ER- / PR+ / Her2- ER+ / PR+ / Her2-
III	ER+ / PR- / Her2- ER+ / PR+ / Her2- ER- / ER- / Her2-

In agreement with *AMOT* mRNA levels in Jiang *et al.* 2006, we found an eleven-fold increase in Total Amot protein expression over normal breast tissues in these breast tumor tissues (Fig. 4-1A). Unexpectedly, we saw no significant difference in Amot protein levels between ductal and lobular carcinoma tissue, nor between tumor grades I-III, which contrasted the findings in Jiang *et al.* published (Fig. 4-1B; 4-2A,B). Our analysis agreed with Jiang that Amot levels show no correlation with estrogen receptor status, and furthermore, we also found no significant difference in Amot protein expression between PR positive and PR negative tumor tissues (Fig 4-3; 4-4). Surprisingly, we saw no difference in Amot levels between the less aggressive node-negative tumors and more aggressive node-positive tumors (Fig. 4-5). However, we did discover a positive correlation between Amot protein levels and metastatic breast tumors, which agreed with the mRNA data. Metastatic tumors possessed a nearly 3 fold greater expression of Amot than non-metastatic tumors (Fig 4-6A: B). The patients with metastatic breast cancer in this cohort had secondary tumors arise in the liver, bone, and the soft tissues of the head, face, and neck. Local

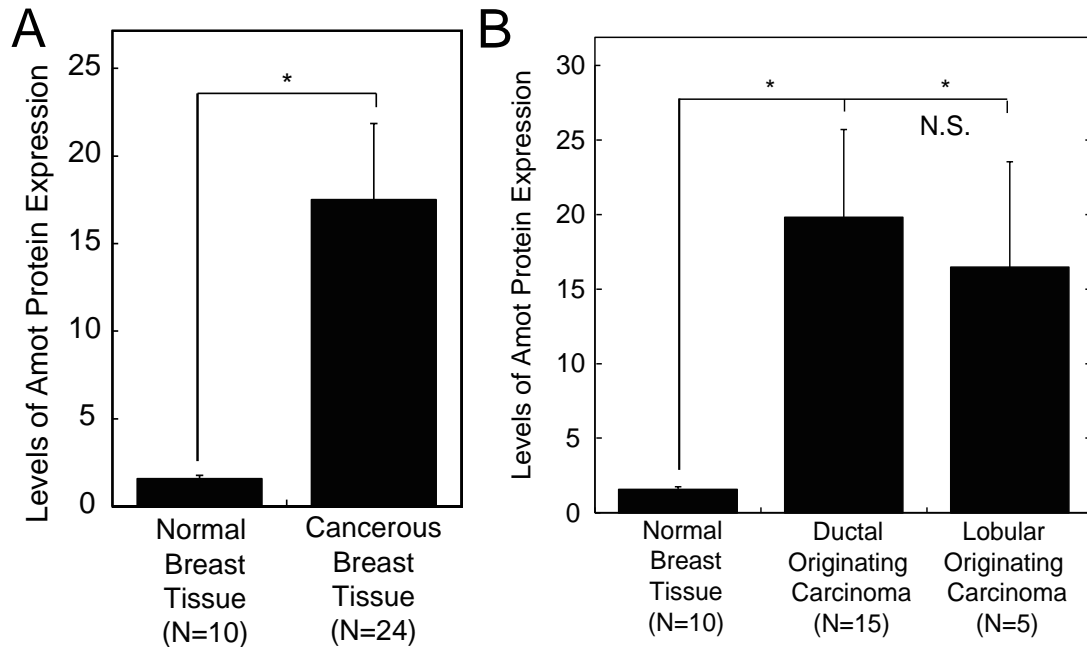


Figure 4-1. Amot protein levels are elevated in breast tumors when compared to normal breast tissues. A. Quantification of average pixel intensity of Amot expression in normal breast tissues vs cancerous breast tissues (A), tumors originating from the mammary duct vs the mammary lobules (B) by Zen Axiovision Image Processing Software. Levels of Amot were normalized to nuclei count. Normal breast tissues: N=10, cancerous breast tissues: N=24, ductal carcinoma tissue: N=15, lobular carcinoma tissue: N=5. SEM. * $p \leq 0.05$.

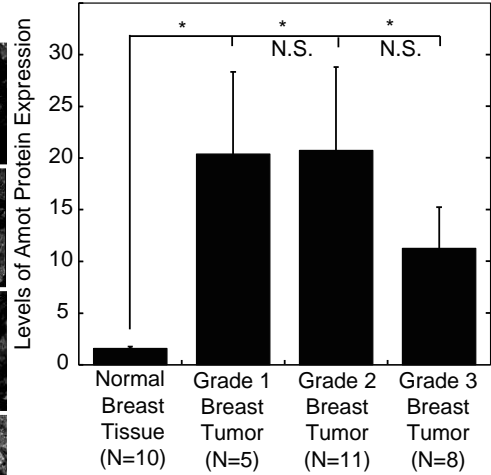
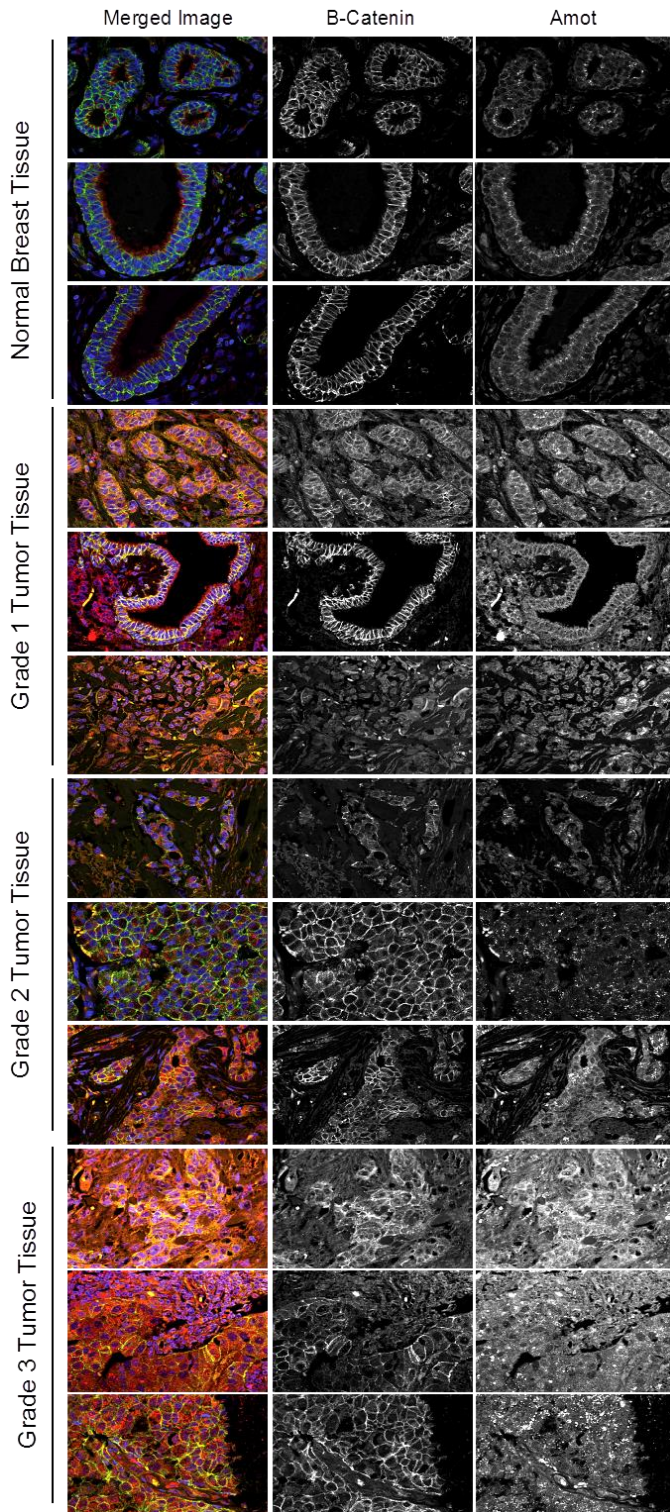


Figure 4-2. Comparison of Amot protein expression between normal breast tissues, and grades I-III breast tumor tissues. A. Immunofluorescent staining of Total Amot (in red). Beta-catenin (green) marks polarized epithelial tissue and Hoescht stain (blue) marks cell nuclei. B. Quantification of average pixel intensity of Amot expression in A by Zen Axiovision Image Processing Software. Levels of Amot were normalized to nuclei count. Normal breast tissue: N=10. Grade I breast tumor tissue: N= 5. Grade II breast tumor tissue: N=11. Grade III breast tumor tissue: N=13. SEM. P <0.05.

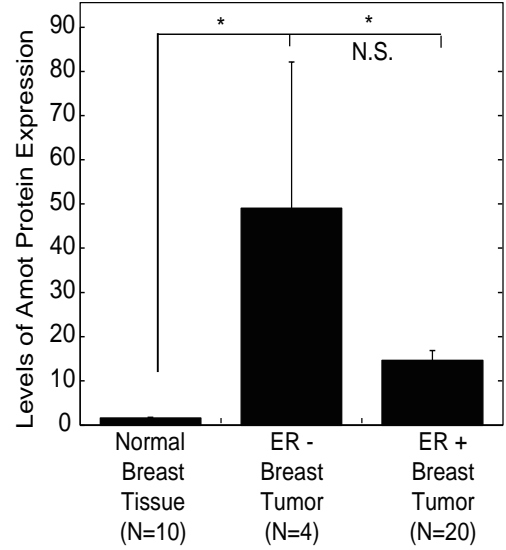
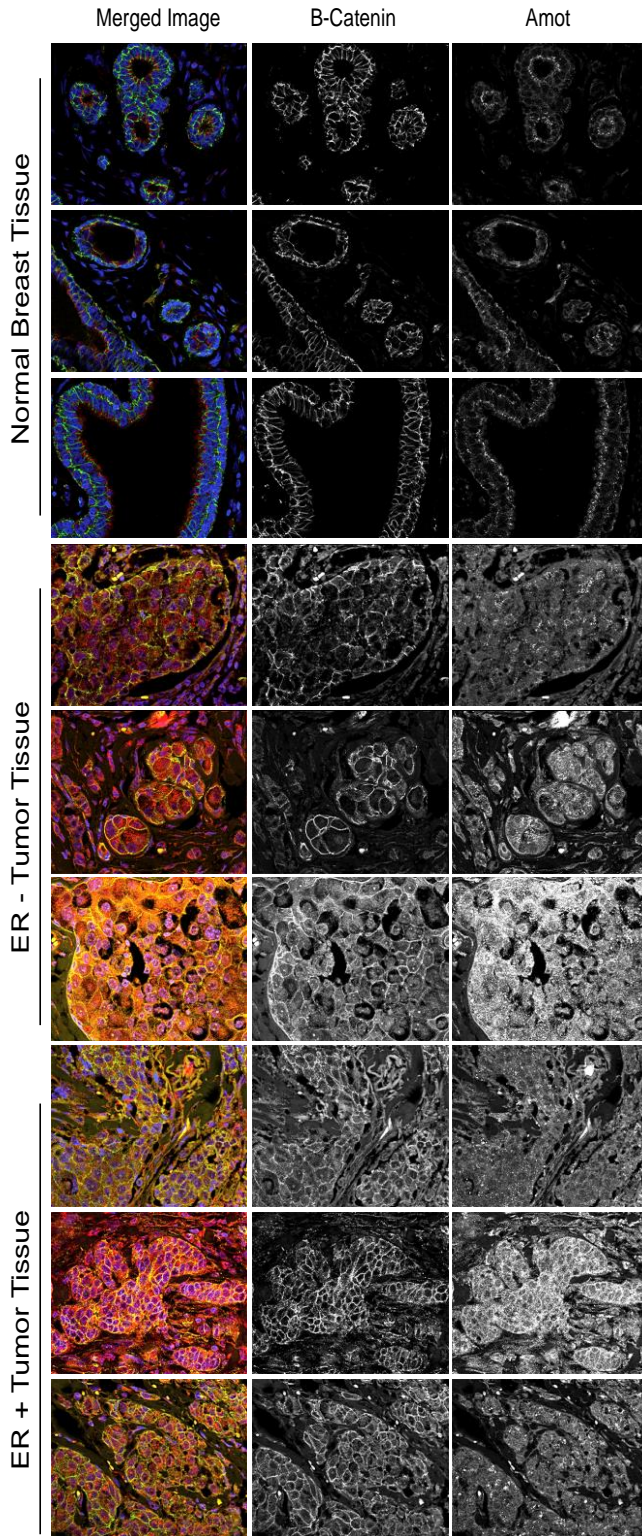


Figure 4-3. Comparison of Amot protein expression between normal breast tissues, and ER negative and positive breast tumor tissues. A. Immunofluorescent staining of Total Amot (in red). Beta-catenin (green) marks polarized epithelial tissue and Hoescht (blue) marks cell nuclei. B. Quantification of average pixel intensity of Amot expression in A. by Zen Axiovision Image Processing Software. Levels of Amot were normalized to nuclei count. Normal breast tissue: N=10. ER - breast tumor tissue: N= 4 ER + breast tumor tissue: N=20. SEM. *p < 0.05.

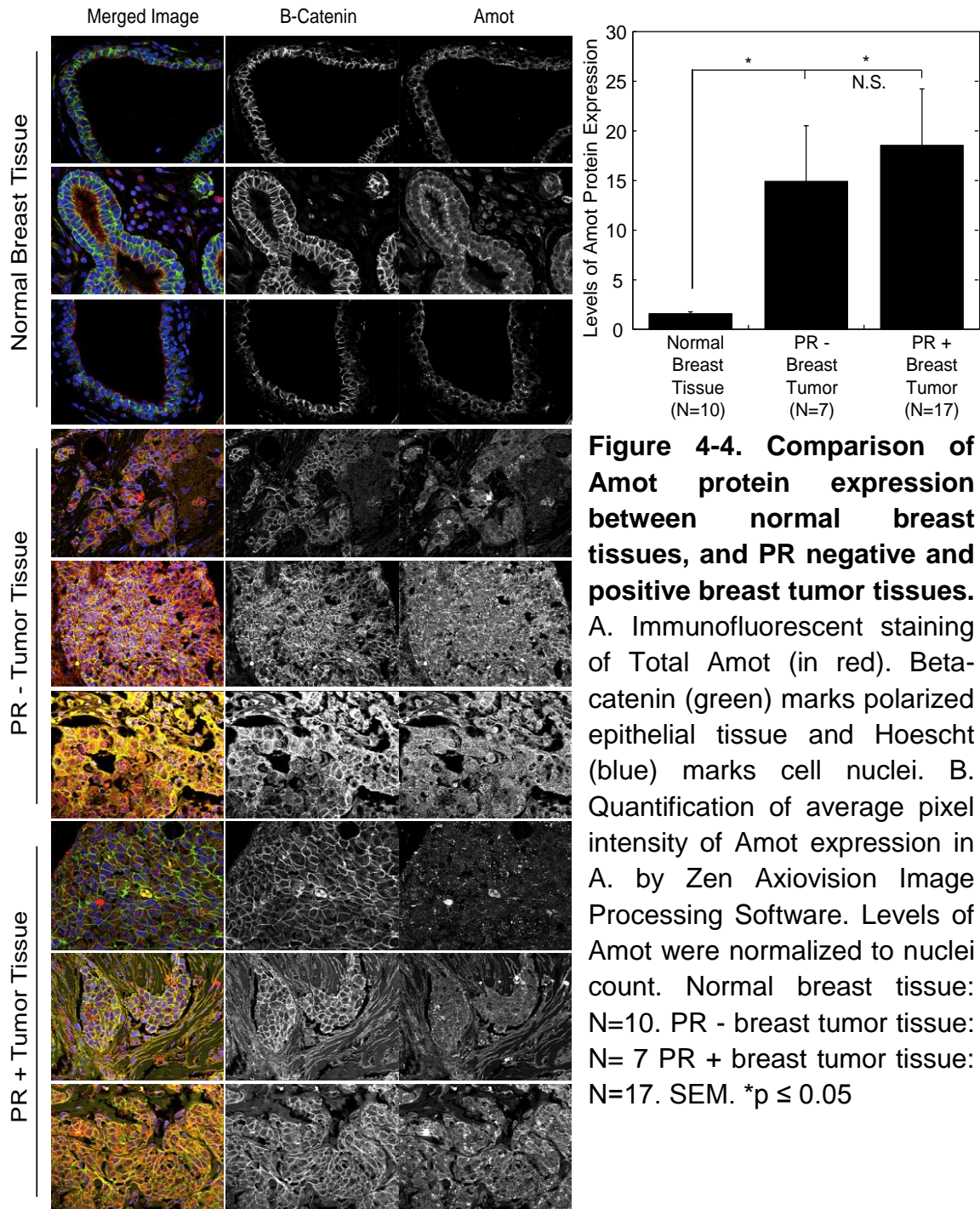


Figure 4-4. Comparison of Amot protein expression between normal breast tissues, and PR negative and positive breast tumor tissues. A. Immunofluorescent staining of Total Amot (in red). Beta-catenin (green) marks polarized epithelial tissue and Hoescht (blue) marks cell nuclei. B. Quantification of average pixel intensity of Amot expression in A. by Zen Axiovision Image Processing Software. Levels of Amot were normalized to nuclei count. Normal breast tissue: N=10. PR - breast tumor tissue: N= 7 PR + breast tumor tissue: N=17. SEM. *p ≤ 0.05

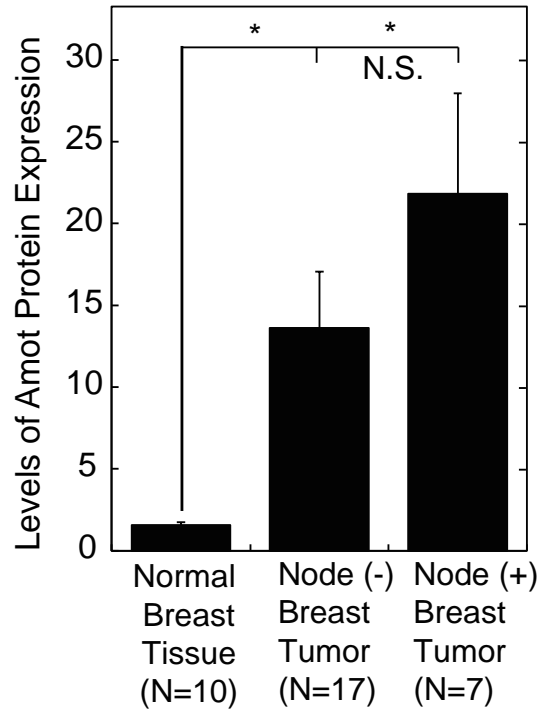


Figure 4-5. High Amot expression does not correlate with node-positive breast tumors than with node-negative breast tumors. Quantification of average pixel intensity of Amot expression in normal breast tissues vs. node negative and node positive breast tumors by Zen Axiovision Image Processing Software. Levels of Amot were normalized to nuclei count. Normal breast tissue: N=10. Node negative breast tumor tissue: N= 17. Node positive breast tumor tissue: N=7. SEM. *p ≤ 0.05

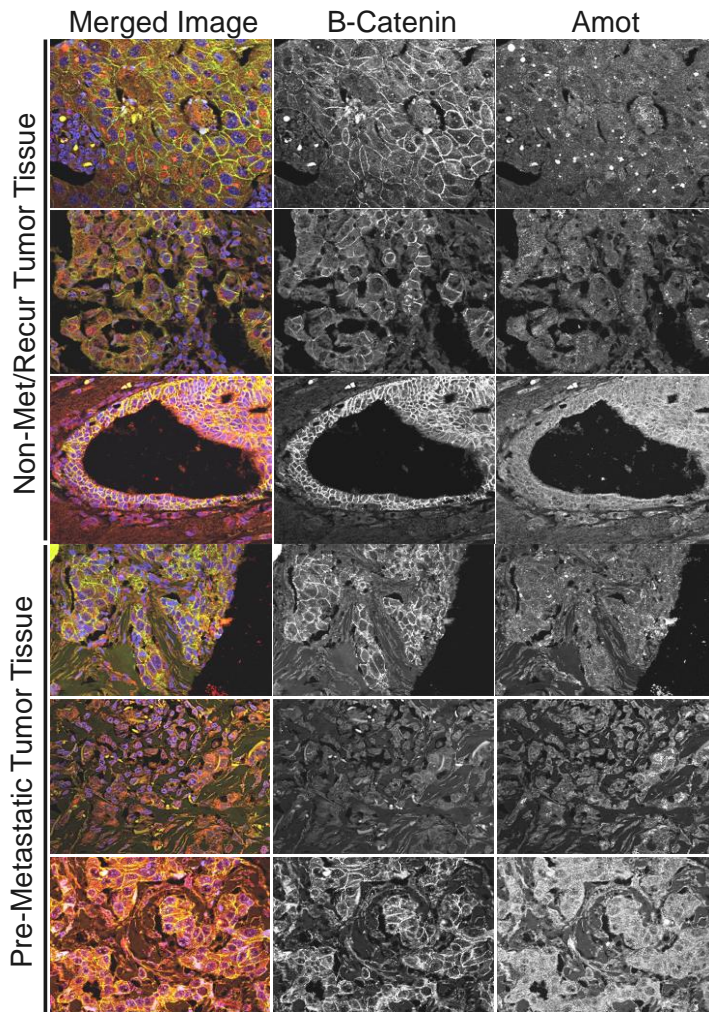
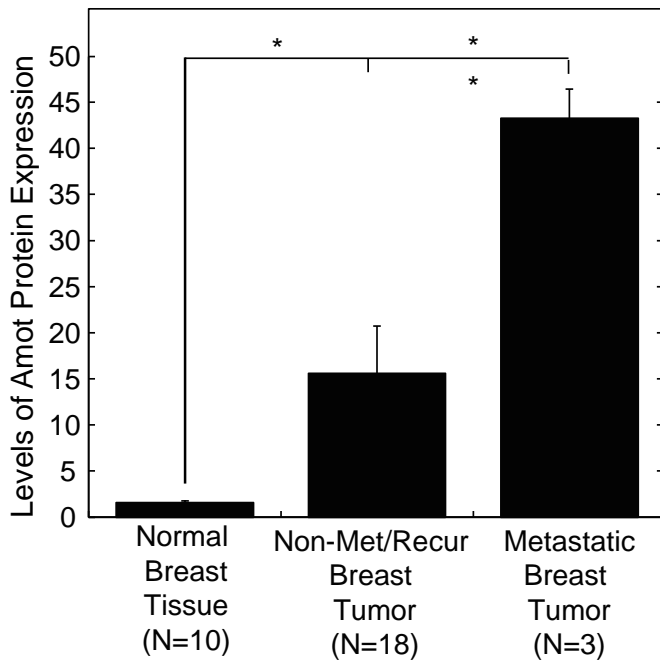


Figure 4-6. Comparison of Amot protein expression between non-metastatic / non-recurrent breast tumor tissues, and pre-metastatic breast tumor tissues. A. Immunofluorescent staining of Total Amot (in red). Beta-catenin (green) marks polarized epithelial tissue and Hoescht (blue) marks cell nuclei. B. Quantification of average pixel intensity of Amot expression in A. by Zen Axiovision Image Processing Software. Levels of Amot were normalized to nuclei count. Normal breast tissue: N=10. Non-metastatic / non-recurrent breast tumor tissue: N=18. Metastatic breast tumor tissue N=3. SEM. * $p \leq 0.05$.



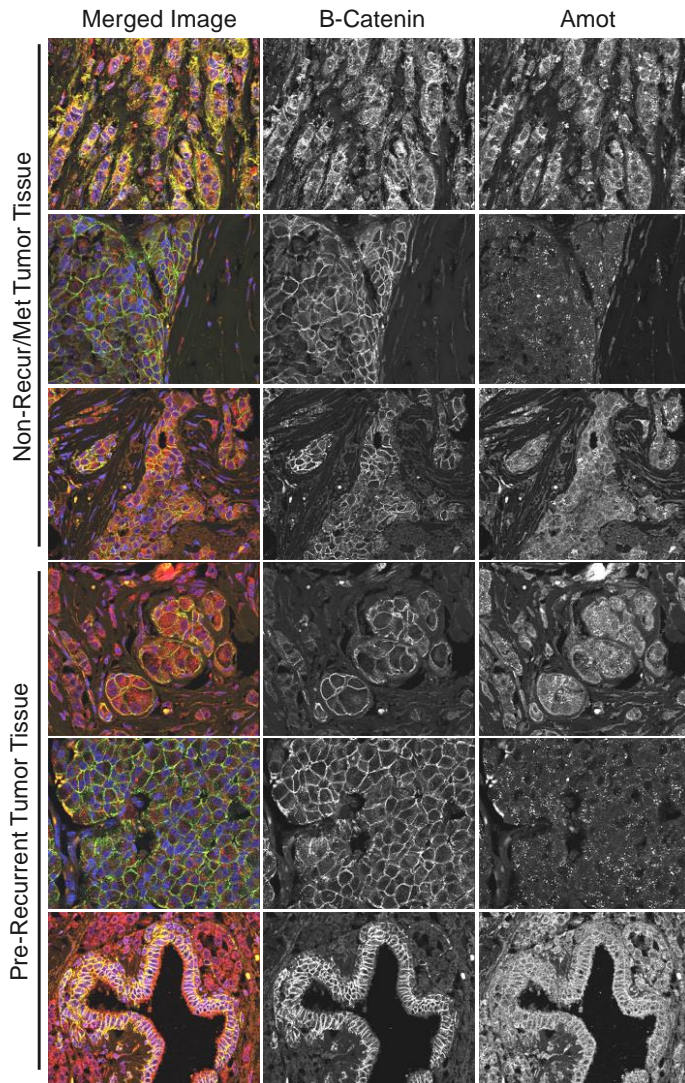
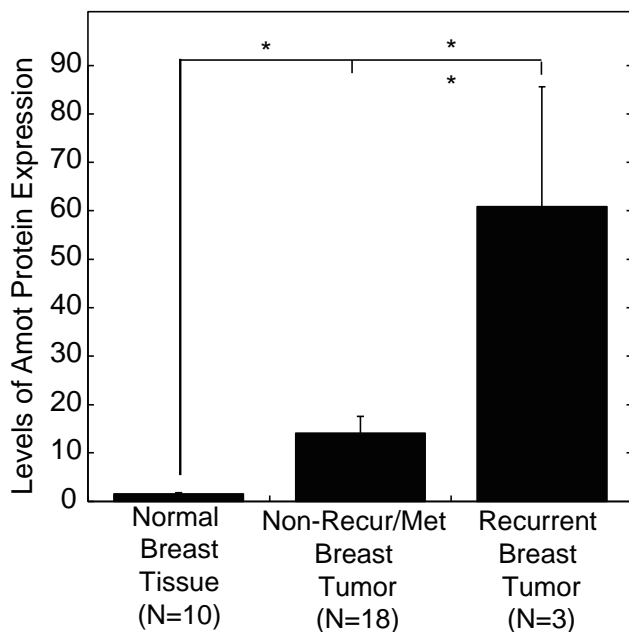


Figure 4-7. Comparison of Amot protein expression between non-recurrent breast tumor tissues and pre-locally recurring breast tumor tissue. A. Immunofluorescent staining of Total Amot (in red). Beta-catenin (green) marks polarized epithelial tissue and Hoescht (blue) marks cell nuclei. B. Quantification of average pixel intensity of Amot expression in A. by Zen Axiovision Image Processing Software. Levels of Amot were normalized to nuclei count. Normal breast tissue: N=10. Non-metastatic / non-recurrent breast tumor tissue: N=18. Recurrent breast tumor N=3. SEM. * $p \leq 0.05$.



recurrence also related positively to Amot protein levels, in which recurrent tumors exhibit a greater than 4-fold increase in Amot (Fig 4-7A: B). Jiang *et al.* found no difference in transcript levels between recurrent and non-recurrent tissues. Interestingly, only one of the three metastatic patients and one of three recurrent patients was diagnosed as node-positive, a factor clinically classified as a major predictor of tumor aggressiveness. This may implicate the presence of excess Amot protein levels as an additional predictor of aggressiveness in breast tumors.

To further develop this theory, we sought to understand the role of Amot as a potential driver of a transition from DCIS to IDC. Although non-obligate, DCIS as a precursor to IDC occurs in nearly 40 % of cases [7]. The comparison of representative samples from these cases, along with the remaining 60% of IDC cases, provide a solid model for studying the significance of a protein in driving a DCIS to IDC transition. These tumors provided us the opportunity to investigate differences in Amot expression in invasive tumors with or without a predominant presence of DCIS lesions. IDC tumors with a high presence of DCIS lesions are undergoing multiple DCIS to IDC transitional events, whereas IDC tumors with the absence of DCIS are less likely to have undergone transition, and rather the invasive disease developed *de novo* [161,162]. IDC tumors with DCIS revealed a 4-fold elevation of Amot over those tumors lacking DCIS lesions, indicating the strong correlation of amplified Amot in tumors that have undergone DCIS to IDC transitions (Fig 4-8). This is the first study to discover increased Amot levels in DCIS to IDC transitions.

The expression level of Amot protein is indeed a key piece of evidence to help us understand its role in DCIS to IDC transitions. However, the ability to examine the dynamic localization and patterning of the Amot staining within the tissue structure and the cells as it related to β -Catenin is a major advantage of tissue imaging as opposed to IHC and immunoblot analysis. It is crucial to investigate Amot with respect to organ and subcellular localization as it compares to the clinical characteristics we have analyzed in this cohort. To accomplish this, we analyzed the localization of Amot expression in subcellular compartments across all of the samples.

We identified the presence of Amot in three unique manners within the tumor tissue: junctional, punctae, and nuclear / perinuclear (Fig 4-9A). The presence of Amot at apical junctions was a staining pattern most similar to that of normal ductal structures. This localization indicates a more polarized and growth-arrested phenotype, where unphosphorylated Amot 130 sequesters YAP1 at polarity protein complexes associated with tight and adherens junctions [138,163]. We pooled all of the tissues that exhibited Amot junctional staining and found them all to possess predominant DCIS lesions. The average tumor grade of these samples was 1.75 +/- 0.8. In these, we observed that Amot is apically localized in the highly polarized cells, identifiable by the highly organized pattern of beta-catenin staining. However, the cells that are appearing to establish regions of micro-invasion tend to possess an altered Amot localization and pattern; here, a more punctate aggregation of Amot staining was observed.

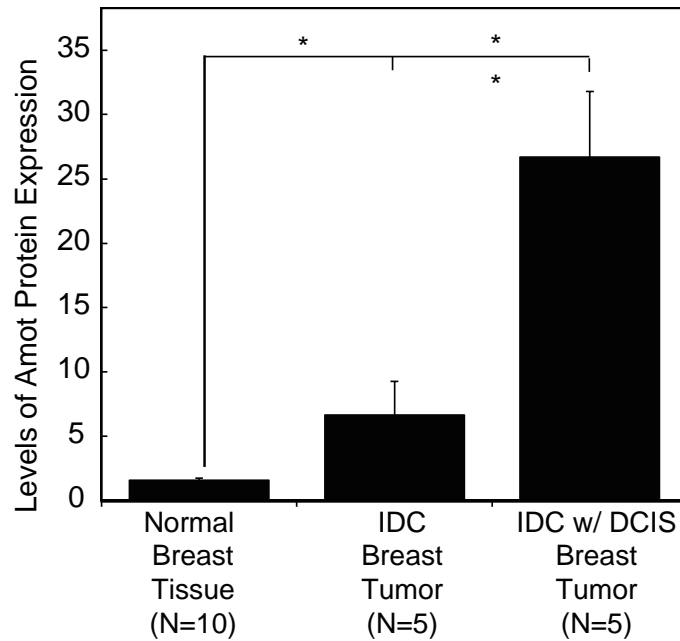


Figure 4-8. Amot protein levels are more greatly elevated in IDC breast tumors with predominant presence of DCIS than in IDC breast tumors that lack the presence of DCIS. The quantification of average pixel intensity of Amot protein expression in normal breast tissues vs IDC tumors without presence of DCIS and IDC with presence of DCIS by Zen Axiovision Image Processing Software. Levels of Amot were normalized to nuclei count. Normal breast tissue: N=10. IDC (DCIS -) breast tumor tissue: N= 5. IDC (DCIS +) breast tumor tissue: N=5. SEM. * $p \leq 0.05$.

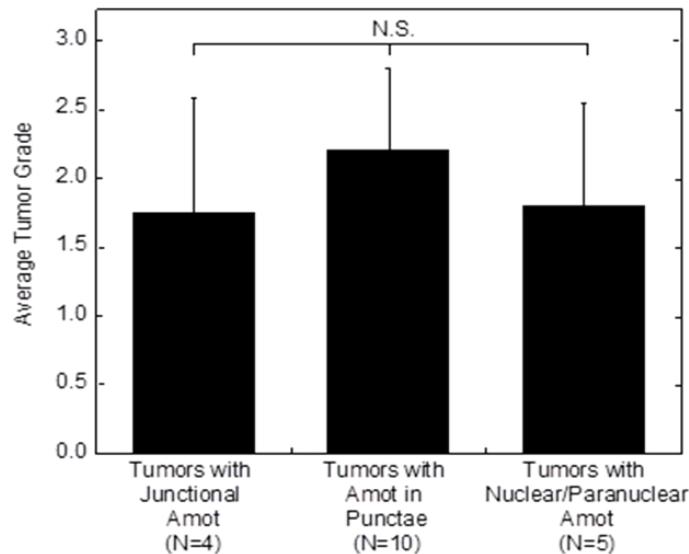
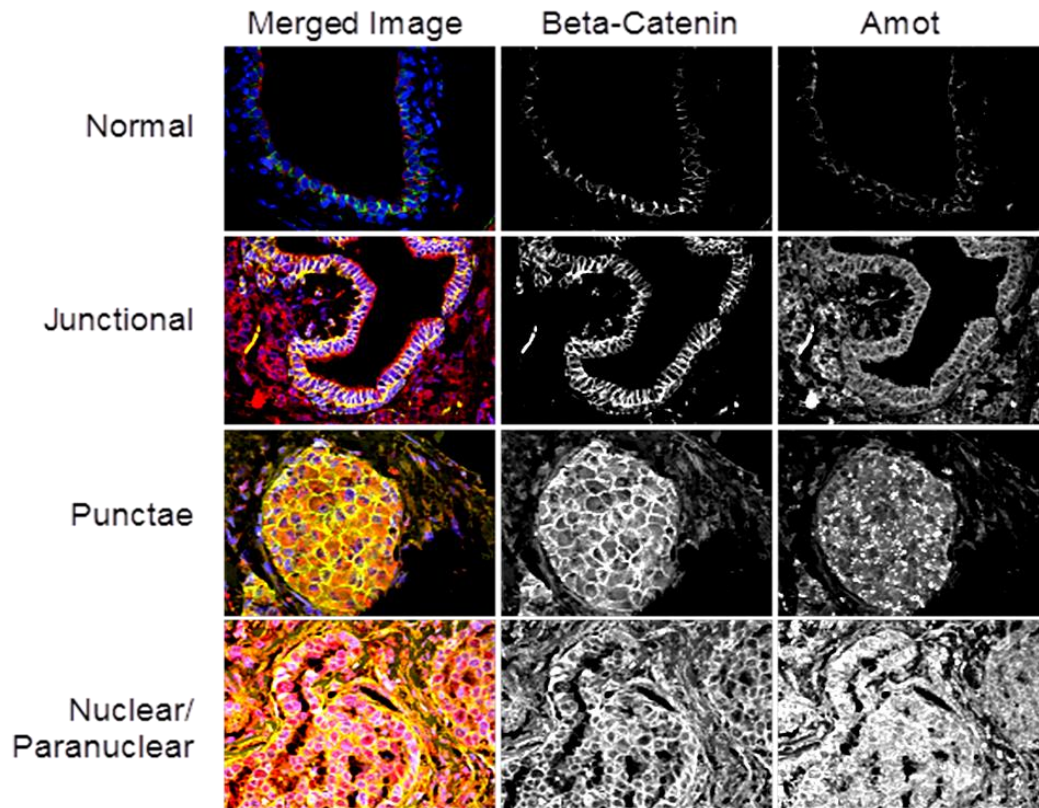


Figure 4-9. The pattern of Amot staining and localization is variable in tumor tissues verses normal breast tissue. A. Dual immunofluorescence staining of total Amot and polarized epithelial marker β -Catenin displays the presence of Amot in different locations including at apical junctions, in aggregate punctae, and in nuclear and paranuclear compartments. B. The tumor grades of the tissues exhibiting the presence of Amot in these different subcellular compartment were compared. Tumors with: junctional Amot (N=4), Amot in punctae (N=10), and nuclear/paranuclear Amot (N=5). SEM. ANOVA. * $n \leq 0.05$

The presence of Total Amot at juxta nuclear punctae has been proposed to mark the association of Amot p80 to the lipid raft-enriched membranes of juxta nuclear recycling endosomes [166]. In cells exhibiting a pro-migratory phenotype, it is on these endosomes by which Amot 80 co-localizes with pro-migratory protein functioning to traffic toward the leading migratory edge of the plasma membrane [164]. This is consistent with the patterning of exogenous Amot 80 staining in fixed cells (data not shown), where the signal occurs predominantly in large, dense, aggregates near the nucleus. Sixty percent of the patients with tumors we found exhibiting this pattern of Amot staining possessed predominant DCIS lesions and thirty percent experienced a metastatic or recurring event. The average tumor grade of the tumors displaying punctal Amot staining was found to be 2.2 +/- 0.6.

Additionally, we saw a more diffuse staining of Amot occurring in and around the nucleus. Reports have surfaced previously implicating the nuclear translocation of the Amot130-YAP1 complex, and even go so far as to demonstrate the ability of Amot 130 to function as a transcriptional co-activator alongside its binding partner YAP1 [139,165]. We found five samples in our cohort that demonstrate Amot nuclear and/or para-nuclear staining. Still, there is much more to understand about how the presence of Amot in the nucleus alters its governance of YAP1. These tissues possessed an average tumor grade of 1.8 +/- 0.7, and sixty percent of these tissues were diagnosed as IDC that lacked the presence of DCIS lesions. In comparing all of these groups of tumors, we found

no significant difference in tumor grade with respect to the distinct localization and patterning of Amot (Fig 4-10B).

A limitation of this study was that we could not report a correlation with regard to Her2 status, as every tissue we were able to analyze was Her2 negative. A recent study, Barutello *et al.* 2015, examined female Her2+ mice which were born and fed from mothers that were injected with the anti-angiogenic vaccine against Amot, first reported by Holmgren *et al.* 2006. High levels of anti-Amot antibodies were present in the sera of these mice and these levels correlated with significant delays in Her2+ tumor growth [166,167]. Analysis of more blocks from the TMA, in which more samples may provide more variety with regard to Her2 status, would allow for this correlation to be made in the future.

Contrasting with Jiang *et al.* published, we found that Amot protein expression was indeed high in recurrent tumor tissues versus non-recurrent tumor tissues. We also found no significant difference in Amot levels between tumors derived from the mammary duct versus the mammary lobule, nor did we observe a difference in levels between node positive and node negative tumors. Conclusively, we have supported the mRNA evidence for elevated Amot levels in breast cancers with respect to several clinical and histological features. First, we found that Amot protein expression was elevated in breast cancer over normal breast tissues. We also found that Amot levels were higher in metastatic versus non-metastatic breast tumor tissues [130].

Our further analysis that expanded the study by Jiang *et al.* sought to investigate the changes in Amot levels in tumors undergoing DCIS to IDC transitions, versus those tumors that arose *de novo*. We found a significant increase in Amot protein expression in the transitioning tumors, implicating Amot as a potential player in this process. All of these transitioning tumors possessed an Amot staining pattern associated with the promotion of a migratory phenotype.

Ultimately, we are interested in continuing this work in additional blocks in the tumor microarray. The ability to investigate how Amot protein expression and staining pattern associate with patient survival and Her2 status would further complement the initial work we have completed, and possibly add support to the potential for the anti-Amot vaccine to move into clinical trials.

**CHAPTER 5: A SINGLE PROMOTER GOVERNS THE TRANSCRIPTIONAL
ACTIVATION OF THE LONG (130 KDA) ISOFORM AND THE SHORT (80
KDA) ISOFORM OF ANGIOMOTIN**

5.1. Introduction

The Angiomotin proteins are highly conserved and generally function as scaffolding proteins within the HIPPO growth control pathway in the breast and in other tissues [168]. First published in 2001 by Troyanovsky *et al.*, Angiomotin was initially identified as an 80 kDa protein that binds angiostatin and that induces the migration of endothelial cells [169]. To date, 123 studies discussing Angiomotin have been published. Angiomotin was also found to be directly involved in chemotaxis [169,170]. It was subsequently appreciated that the *AMOT* gene yields two distinct isoforms. Amot p130 is a 130 kDa protein comprised of 1084 amino acids coded for by ten translated exons. Amot p80 is an 80 kDa protein comprised of 675 amino acids coded for by nine translated exons. Because only exon 1 of the 10 translated exons that code for Amot 130 is not shared with Amot 80, it was reported by Bratt *et al.* 2005 that these two isoforms are generated through alternative splicing [129]. Literature discussing the existence of these two isoforms did not appear until 2005, and the seventeen studies published since then regarding their localizations and functions are quite controversial. Amot p130 was first recognized in endothelial cells where it was found to localize at tight junctions and on actin fibers [137]. Amot p80 was found to colocalize with Amot 130 at the tight junctions, but not on actin fibers. Amot p80 was also found to be present at lamellipodia of migrating cells, suggesting its role in driving cell movement and migration [129]. Since then, both isoforms have also been found to exist perinuclearly [164], as well as intranuclearly [139]. Most reports also find that Amot 80 acts as a dominant negative regulator of Amot 130.

This was initially found to redirect Amot and its associated apical polarity protein complexes to juxta nuclear endosomes resulting in a loss of tight junction integrity [164]. Unpublished work from our lab finds that Amot 80 also redirects the Amot 130/YAP1 complex away from cell junctions to juxta nuclear endosomes. While Amot 130 was initially reported to drive epithelial apical polarity and to inhibit cell growth and migration, it is now appreciated that it functions in this manner only in the presence of low levels of Amot 80 and when phosphorylated by LATS 1/2 [136]; Ranahan *et al.* unpublished. This study seeks to identify the manner by which the transcription of Amot 130 and Amot 80 are controlled. This, in turn, may provide insights into how such expression is upregulated to promote cancer initiation, promotion, and progression.

5.2 Methods and Materials

Genetic inactivation of Amot via CRISPR.

Complementary guide RNAs of 18 base pairs were designed to target specific regions of the Amot genome upstream of pan sequences. Annealed guide RNA sequences were cloned into a clustered regularly interspaced short palindromic repeats (CRISPR) lenti-viral plasmid (Sigma). HEK 293T cells were stably infected with the Amot transcription start site (TSS) CRISPR target construct or the empty CRISPR control. Cells then underwent puromycin selection for a duration of two weeks; clones were isolated and passaged prior to harvest.

5' Rapid Amplification of cDNA Ends (5' RACE) of human cDNA.

Total RNA was harvested from HEK 293T and MDA-MB-468 cells using Trisol-chloroform extraction. The 5' RNA ligase-mediated rapid amplification of cDNA (RLM-RACE) reactions were performed using the First Choice RLM-RACE protocol (Ambion). Complementary DNA (cDNA) was synthesized from the linker-ligated RNA using reverse transcriptase and random octamers. PCR amplification of the linker-ligated cDNA was performed using the 5' RLM-RACE Kit Outer Linker Primer and 3' Primers designed to specifically target each individual Amot isoform.

Synthesis of the Angiotensin Promoter.

The Amot Promoter was synthesized by GenScript DNA Synthesis Services and corresponds to GrCh 38 position 112840700 to 112842172 which includes the most 5' transcriptional start site (experimentally discovered) and flanking Kpn1 and HindIII restriction sites. Kpn1 and HindIII sites were utilized in cloning the Amot Promoter insert into a pGL3 Basic Luciferase Vector backbone. Naturally occurring restriction sites within the sequence include: Two Apa1 sites, one EcoR1 site, one Mlu1 site, and one Sac1 site. Diagnostic digestions for all the sites demonstrated successful cutting of the Mlu1 site. The Mlu1 site occurs between the two RNA polymerase 2A binding regions identified by ENCODE in the Amot promoter. This Mlu1 site was then utilized to successfully replace the wild type promoter sequence with another synthesized sequence in which all 5

occurring SP1 transcription factor binding sites were mutated construct to determine the regulatory region most important for *AMOT* gene transcription

Genomic Bioinformatics

The following databases were employed to build the various diagrams depicting the genomic structure of the *AMOT* gene: National Center for Biotechnology Information (NCBI): Expressed Sequence Tags (EST), Gene, and Basic Local Alignment Search Tool (BLAST), Ensembl Genome Browser, University of California Santa Cruz (UCSC): Genome Browser, GeneBlat, and Encyclopedia of DNA Elements (ENCODE). Information provided by these databases was used to build comprehensive diagrams, align PCR sequencing data, investigate potential splicing patterns, and identify key promoter elements and potential regulatory factors.

5.3. Results

The location of the *Amot* promoter has been proposed to lie either immediately upstream of the first exon of *Amot* 130 [128] or in an unidentified region almost 20,000 base pairs upstream of this location. Upon investigating the expressed sequence tags (ESTs) that shared sequences with exons that encode *Amot*, multiple non-coding exonic sequences were found to occur upstream of the known *Amot* p130 coding exons. Further, these exons were joined alternatively to lack the first coding exon but contain the second coding exon so that they likely also contribute to the expression of *Amot* p80. Based on the

genomic structure of the *AMOT* gene, there is also evidence to potentially support the existence of two distinguishable promoters (Fig 5-1). We set out to identify the transcriptional start site(s) for the *AMOT* gene and then use this to define the location(s) of the Amot promoter(s).

For this purpose, a diagram of the genomic architecture of the *AMOT* gene was compiled from a variety of genomic databases. The consensus was that the *AMOT* gene has a total of thirteen exons, three of which occur in the 5' leader region upstream of both Amot 130 and Amot 80 translational start sites (Fig 5-1). The analysis of the expressed sequence tags (ESTs) aligning with Amot p130 verses Amot p80 yielded overwhelming evidence to support a single promoter upstream of exon 1 between ChrX(-) 112842172-112840700 (Fig 5-1; Fig 5-2). However, an additional region of active chromatin to which RNA Polymerase 2A and transcription factors bind occurring between ChrX(-) 112835473-112832385 indicated a potential second promoter just upstream of the start of exon 2 (Fig 5-1). Determining the location of the promoter element(s) that regulate the activation of the Amot isoforms required us to define the transcriptional start site(s) for Amot 130 and Amot 80. To accomplish this, we first had to characterize the 5' regulatory region of the *AMOT* gene. According to our investigation of Amot across multiple nucleotide databases, including NCBI, Ensembl, and UCSC genome browser, it appears that one transcriptional start site is recognized as the sole transcriptional start site (TSS) controlling the transcriptional activation of both Amot isoforms. Interestingly, the region upstream if this location lacks both common promoter sequence motifs TATA or

CCAAT, but analysis of UCSC Encyclopedia of DNA Elements (ENCODE) database indicates a concentrated region of transcriptional factor and RNA polymerase binding, as well as active open chromatin at a location further upstream of the indicated TSS. This led us to experimentally validate the actual TSS site(s) for Angiomotin using the 5' Rapid Amplification of cDNA Ends (5' RACE) method [171].

In order to ensure that only true TSS(s) would be identified from the 5' RACE experiments, we used cDNA libraries prepared from HEK 293T and MDA-MB-468 cells in which the 5' mRNA cap of the extracted RNA was removed and replaced with a 20 base pair DNA linker. The subsequent polymerase chain reaction (PCR) amplification utilized the 5' primer sequence that anneals to the linker DNA and a 3' primer sequences that complement either the Amot 130 (exon 4) or the Amot 80 (exon 2) specific-noncoding exons. The PCR amplification products were then cloned and the consequent libraries were exhaustively sequenced. This sequencing revealed a consensus from both the 293T and MDA-MB-468 cell lines for three closely spaced transcription start sites before exon 1 (Fig 5-3). This supports the premise that a single promoter controls the expression of both Amot 80 and Amot 130 transcripts.

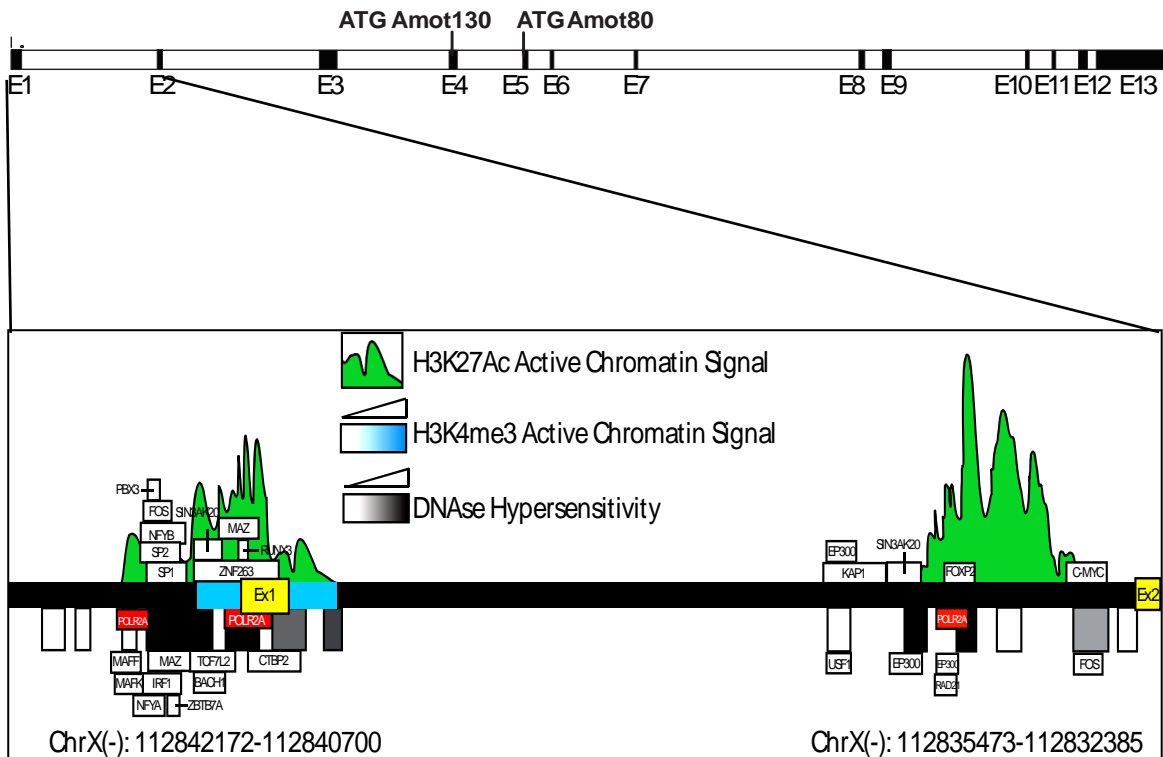


Figure 5-1. A Schematic of the potential promoter regions of the Amot gene. The compiled illustration of the location of H3K27Ac and H3K4me3 active chromatin histone mark signals, DNase hypersensitivity, binding of RNA polymerase 2A and transcription with respect to the Exon1 and Exon 2 positions depicts the potential regions of transcriptional start sites along the Amot gene.

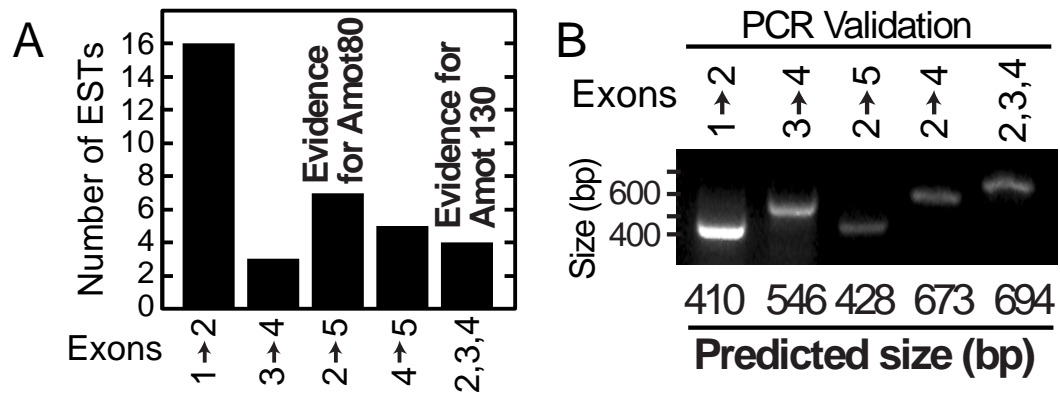


Figure 5-2. The analysis of Amot cDNAs highlight the potential for alternative splicing of the Amot gene. A. Expressed Sequence Tags (ESTs) from the UCSC genome browser revealed the frequencies of various Amot exon-exon junction combinations. The exon-exon junction between 1-2 anneals to both isoforms. The exon-exon junction between 2-5 anneals to Amot 80, and excludes exon 3 and 4. The exon-exon junction between 2-3-4 and 4-5 anneals to Amot 130. B. Quantitative RT-PCR was performed amplifying the various exon-exon junction combinations.

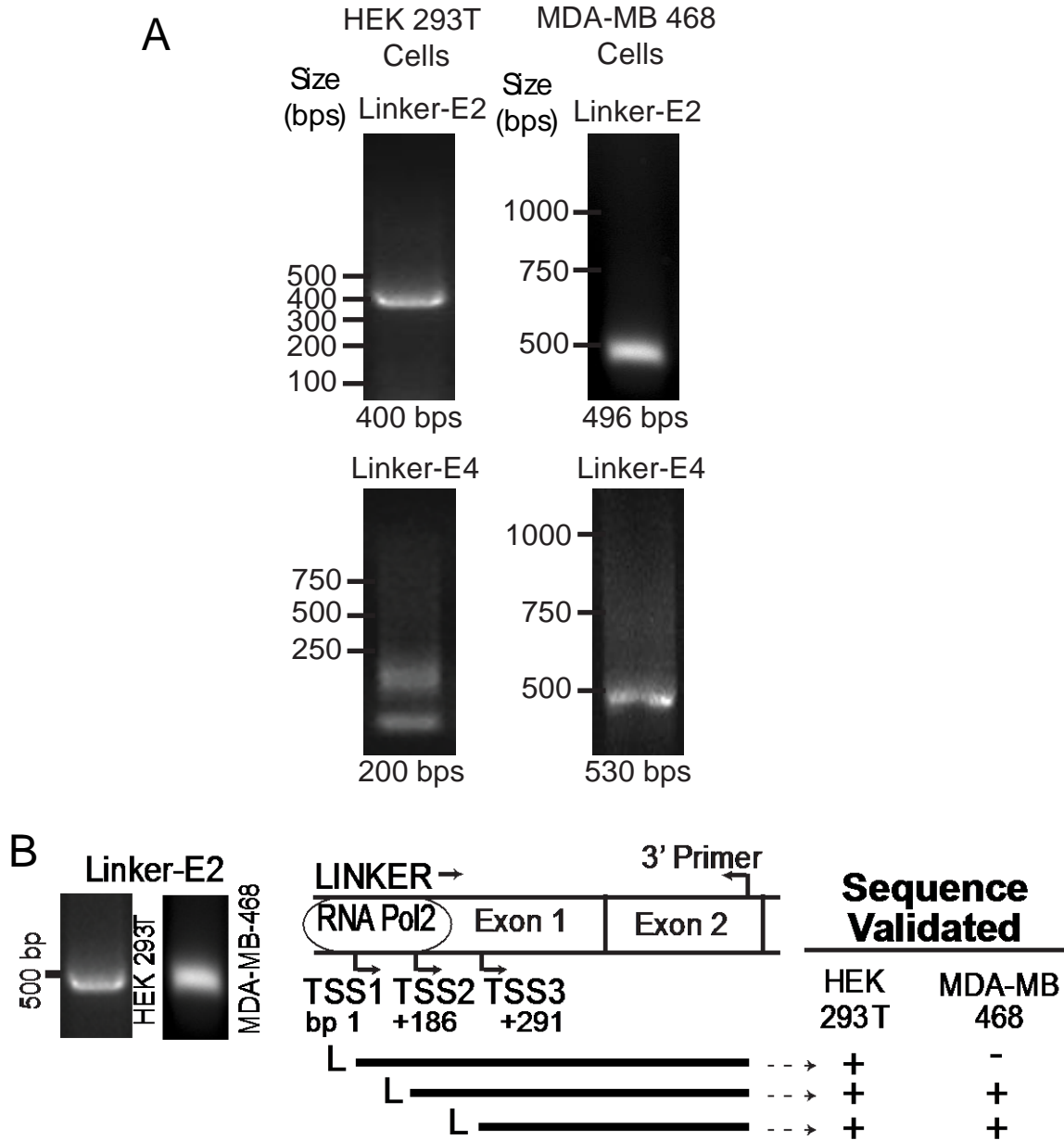


Figure 5-3. A single transcription start site and promoter regulate the expression of Amot 130 and Amot 80. A. 1 % Gel imaging of PCR products resulting from 5' RNA Amplification of cDNA Ends (RACE) experiments performed in MDA-MB-468 and HEK 293T cells. B. cDNAs resulting from 5' RACE experiments in both HEK 293T and MDA-MB-468 cells were synthesized and PCR was ran using primers that anneal to either the Amot 80 specific Exon 2 or Amot 130 specific Exon 4. PCR product sequencing identified three novel transcription start sites for the Amot gene.

More definitive confirmation that the transcription of both Amot isoforms were regulated by a single promoter was provided by the dramatic loss of protein expression of both Amot p130 and Amot p80 in cells in which a CRISPR/CAS9 plasmid had been stably introduced that contained a small guide RNA (sgRNA) targeting the most 5' TSSs in exon 1 (Fig 5-4A-B). Disruption of this site was validated by genomic sequencing (Fig 5-4C-D). Taken together, both Amot isoforms are found to be expressed from a single promoter upstream of exon 1. While this data is consistent with the recent report of a promoter lying upstream of exon 1, this study did not define a TSS nor did they show how this fairly undefined region controlled Amot 80 versus Amot 130 expression [172]. Although the results from the 5' RACE indicated multiple TSS locations along the *AMOT* gene, these sites appear not to be mutually exclusive.

In order to identify which transcripts are expressed from TSS1, reverse transcriptase PCR (RT-PCR) was performed using primers designed to anneal to the exons unique to each isoform and amplify various exonic combinations along the *AMOT* gene (Fig 5-2B; 5-5B). The amplification of exons 2 to 5 produced a PCR product that was shorter than the product resulting from the amplification of exons 2-4 and 3-5. This finding further supports the theory that the both Amot isoforms are made from the alternative pre-mRNA splicing in which exons 3 and 4 are removed from the transcript coding for Amot 80, and are not the result from the activation of multiple Amot Promoters (Fig 5-6). This is reminiscent of AmotL1, which produces similar long and short isoforms from alternative splicing [134].

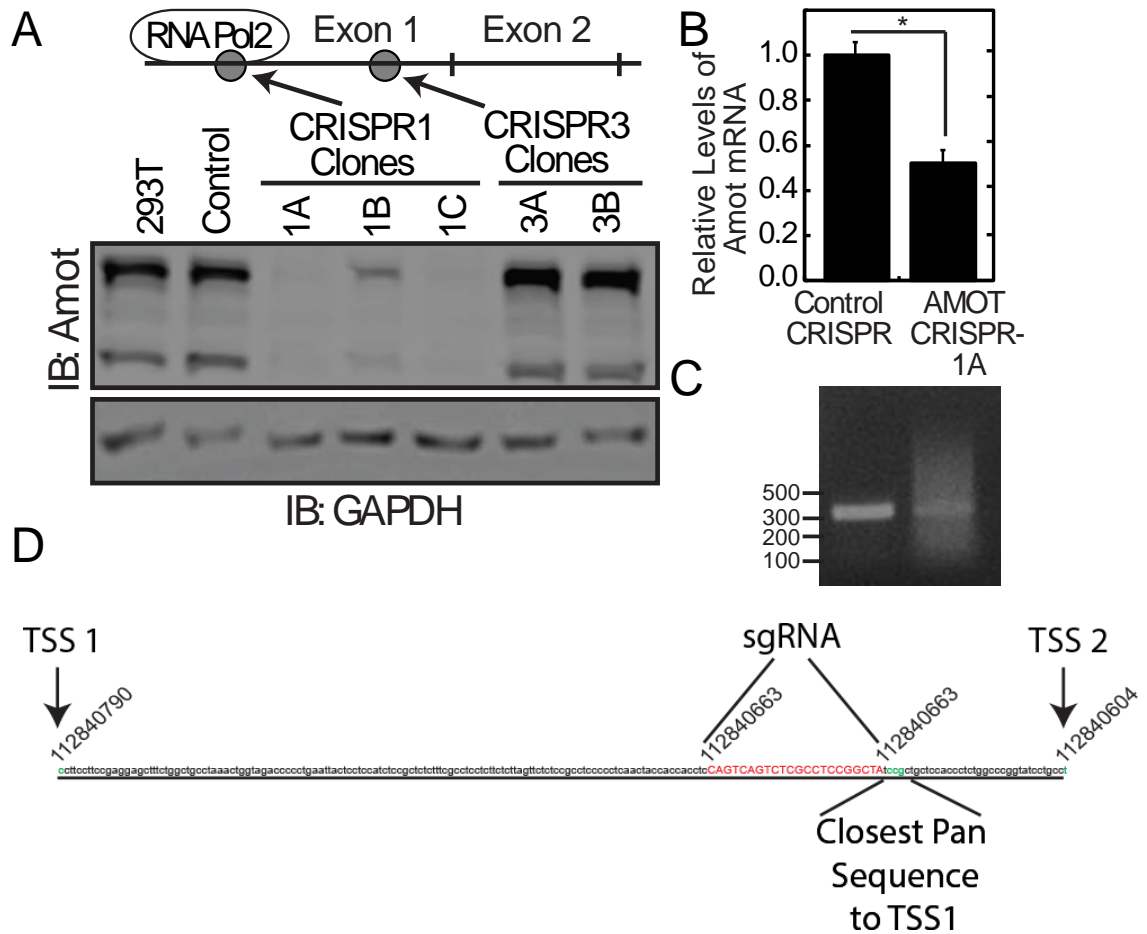


Figure 5-4. Genetic inactivation of the most 5' transcription start site eliminates mRNA and protein expression of both Amot isoforms. A. HEK 293T cells infected with lentiviral plasmids inserted with CRISPR guide RNAs targeting regions of the Amot gene near the TSSs found experimentally with the 5' RACE were immunoblotted and probed for Amot and GAPDH. B. Total Amot mRNA levels were detected by qRT-PCR of HEK 293T cells infected with Amot CRISPR 1, puromycin selected clone 1A. N=3, S.D., Student's T-test, *p < 0.01. C. 1 % Gel imaging of PCR products from the amplification of genomic DNA from CRISPR Control or Amot CRISPR 1A cells with primers flanking the 18 base pair guide RNA sequence. D. The compiled map of the location of the Amot CRISPR guide RNA relative to the experimentally verified TSS 1 and 2.

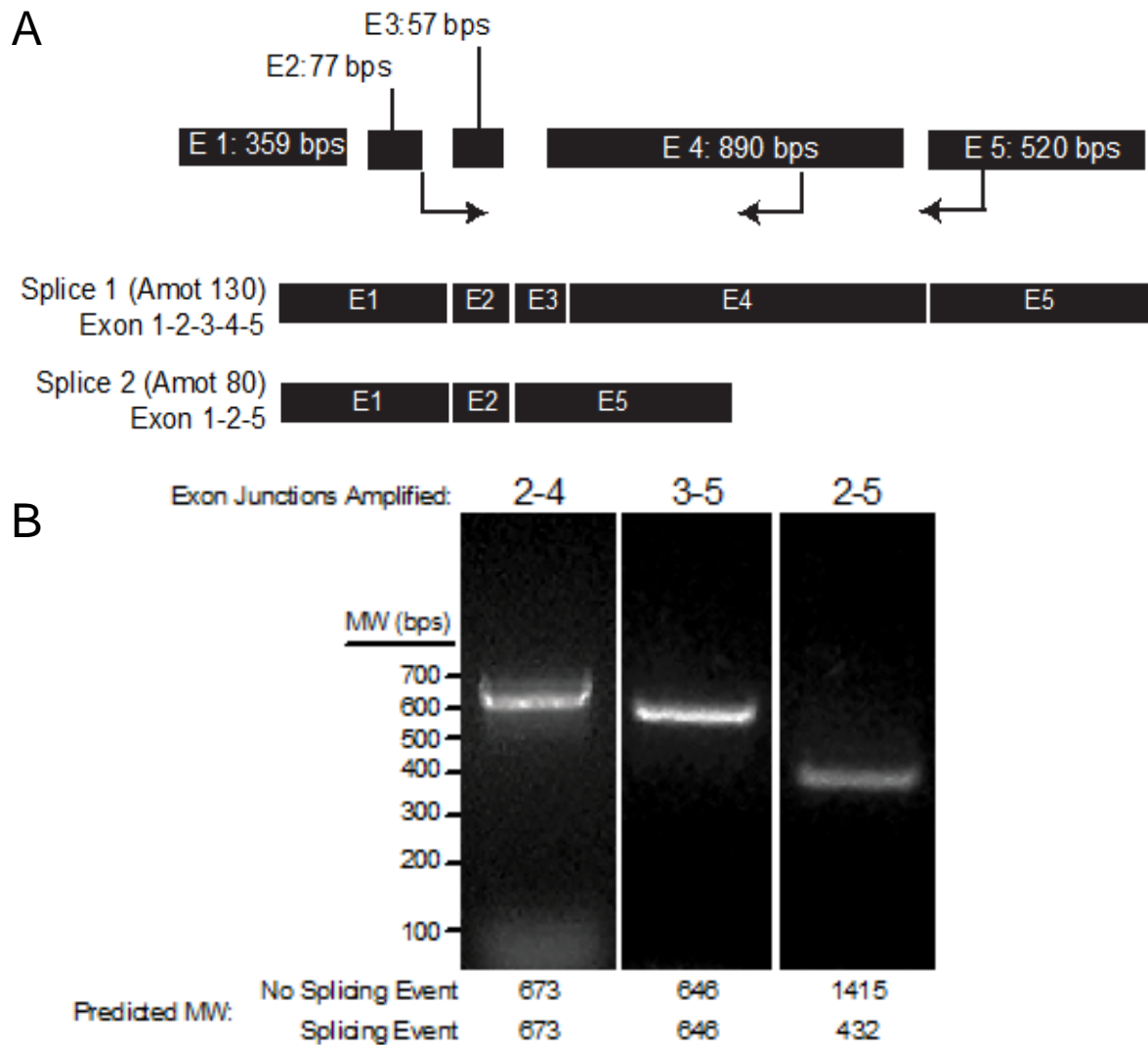


Figure 5-5. The Amot gene has a splice junction between exons 2 and 5.
 A. Schematic of the alternative splicing of Amot to produce the Amot 80 isoform. B. 1 % Gel imaging of the PCR amplification of the exon-exon junctions between exons 2-4, 3-5, and 2-5. The predicted molecular weights (M.W.) of the transcripts with or without the splicing event are displayed.

The identification of Amot isoform specific untranslated exons provides the opportunity to design novel primer sets that distinguish Amot 130 and Amot 80 transcript levels. Therefore, we designed primer sets for quantitative RT-PCR via SYBR green, which require amplicon lengths between 70 and 150 base pairs, and melting temperatures between 59 and 61 C. For the specific detection of Amot 130, we designed a primer set to amplify the exon junction between exons 3 and 4. For the detection of Amot 80, we designed a primer set to amplify the exon junction between exons 2 and 5. Total Amot detection employed a primer set that detects in exon 9. To verify these primer sets, we exploited an observation that our lab has made with respect to the differential silencing of the Amot isoforms by the Amot shRNA construct. This construct demonstrated that Total Amot knockdown by shRNA resulted in the silencing of Amot 130 at 48 hrs post infection, and Amot 80 72 hours post infection (Fig 5-7A). This differential knockdown created a perfect opportunity to validate these Amot isoform-specific primer sets via RT-PCR (Fig 5-7B).

The characterization of the Amot promoter guided our development of a luciferase-based reporter construct (pGL3.1 basic) containing 1500 base pairs upstream of exon 1. The exact length of this putative promoter was predicted based on a comprehensive analysis including the location of the active chromatin regions, DNase I hypersensitivity sites (DHSs), and the concentration of transcription factor binding near the RACE validated TSS. Active chromatin was delineated by histone H3K27Ac and H3K4me3 marks which mark active regions

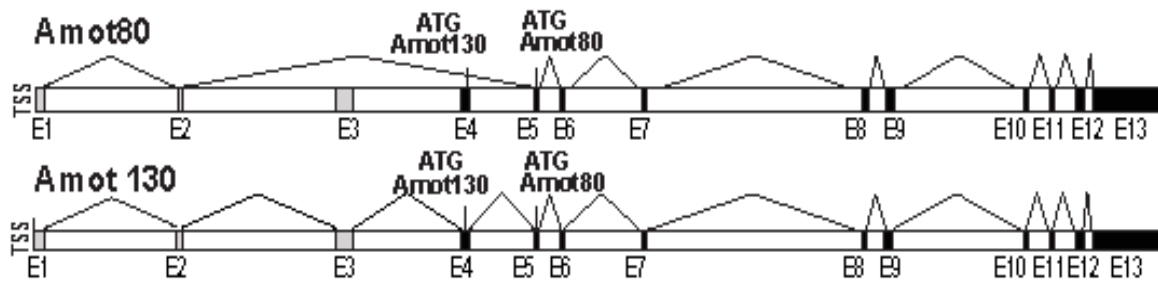


Figure 5-6. The Amot isoforms display alternative exon junctions. Compiled illustration of the unique exon splicing of the 5' leader region yielding two Amot isoforms generated from a single transcription start site.

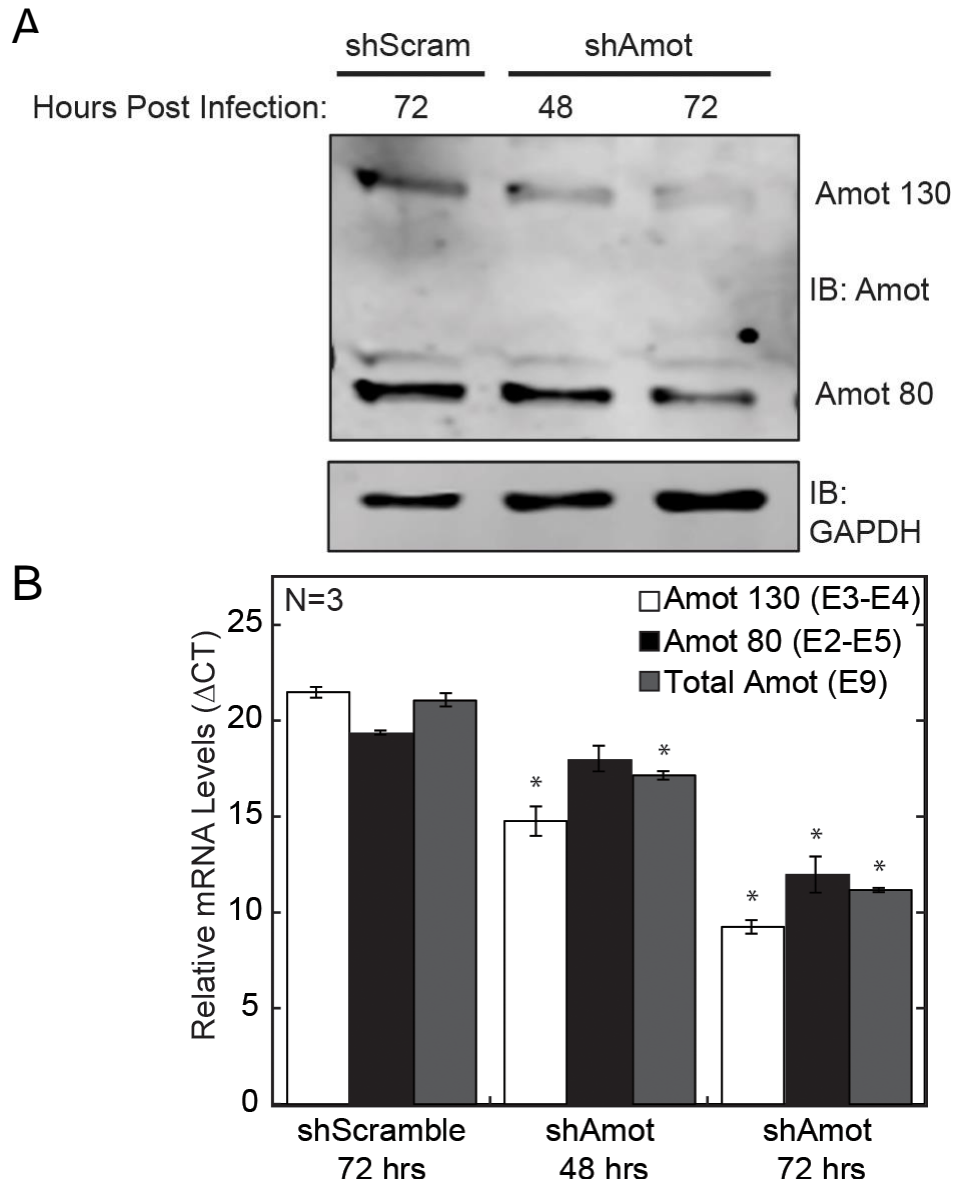


Figure 5-7. The Amot isoform specific exons in the 5' leader region provide the opportunity to design primer sets that can distinguish the transcriptional activation of Amot 80 versus Amot 130. A. MDA-MB-468 cells infected with Amot shRNA lentivirus were collected after 24 hours to enrich for cells specifically silenced for Amot 130, or after 72 hours to enrich for cells that exhibited the knockdown of both isoforms when compared to control. B. The Amot isoform-specific primer sets were used to amplify cDNA from the cells in A. The Amot 130 primer set amplified across the exon-exon junction between exons 3-4, the Amot 80 primer set amplified between exons 2-5, and the Total Amot primer set amplified the region in exon 9. N=3. SD. $P \leq 0.05$.

with high DNA accessibility in the ENCODE database. DNase I hypersensitivity is a direct measure of regions of highly active DNA regions, as euchromatic DNA is far more sensitive to cleavage than heterochromatic DNA by DNase enzymes. The relative darkness of the band, and its corresponding score between 0 and 1000, is related to the signal strength reported from the investigators and is normalized according to UCSC regCluster, a universal scoring standard regulated by UCSC. A score greater than 100 is considered significant (Fig 5-1). Transcription factor and polymerase binding was found in the compilation of chromatin immunoprecipitation sequencing (ChIP-Seq) data from the ENCODE project, which provides the location of the binding region(s) and the specific DNA consensus motif site(s) of all of the transcription factor and polymerase proteins that occupy a promoter. Additionally, ENCODE provides the cluster score of each transcription factor, which is a number between 1-1000 that is relative to the signal strength reported from the investigators and normalized by the UCSC transcription factor binding site (TFBS) cluster standard. A cluster score greater than 300 is considered to be significant (Fig 5-8A) [96].

The full length Amot promoter reporter construct was then transfected into cells alongside a renilla transfection control vector. Promoter activity determined by the measurement of ratio of luciferase expression to renilla expression via luminometer detection. The cells were subjected to treatment with IL-6, which exhibited increased promoter activity. In addition, a co-treatment with IL-6 and a STAT3 inhibitor (C188-9), which functions to compete for STAT3 SH2 domain

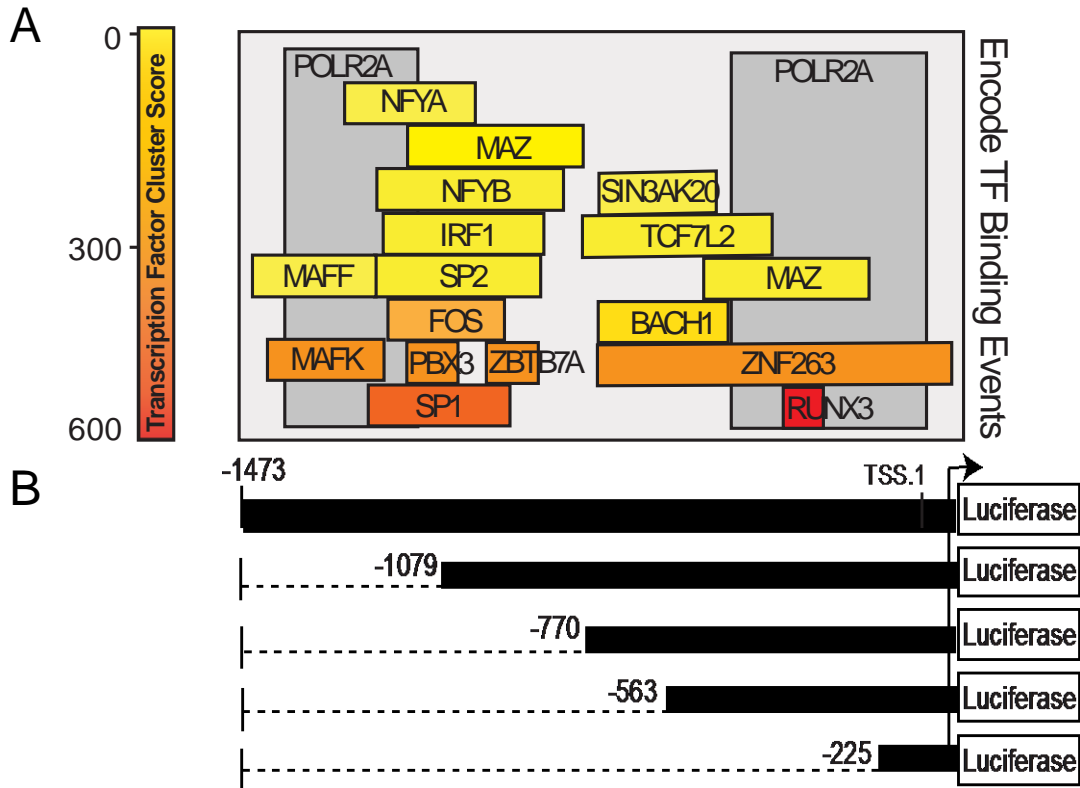


Figure 5-8. A schematic of the Amot promoter and the subsequent serial deletion reporter constructs and the transcription factors found to bind the region. A map depicting ENCODE transcription factor binding in the region 1450 base pairs upstream of TSS1. Transcription factors are plotted and color coded according to their cluster scores. B. The full Amot promoter along with four serial deletion constructs are depicted which gradually eliminate unique regions of transcription factor and RNA Pol2A binding of the Amot promoter. These constructs were all inserted into the pGL3 Basic Luciferase plasmid.

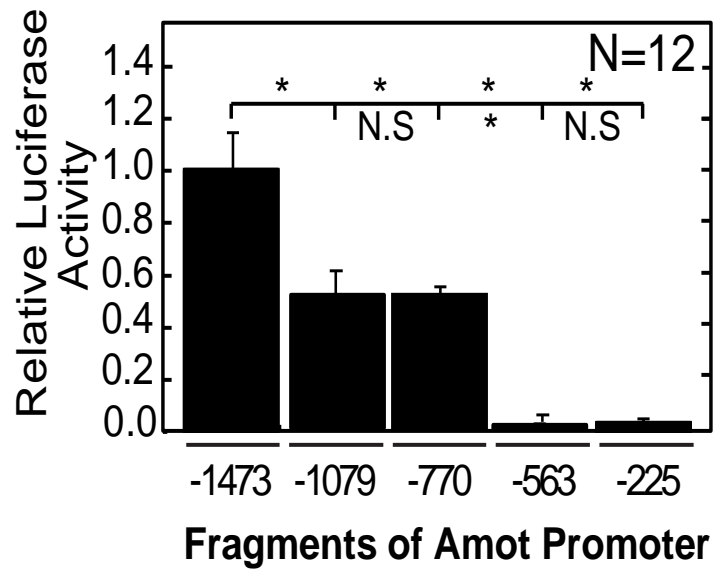


Figure 5-9. Amot promoter activity requires the binding of the transcription factors that occur between -563 and -1473. A. The serial deletion constructs in addition to the full promoter were each transfected into HEK 293T cells for a duration of 20 hrs and measured for luciferase activity. N=12, S.E., Student's t-test, *p < 0.01.

binding, blocked the amplification of Amot promoter activity by IL-6. Both of these results were in agreement with endogenous immunoblot data (shown in Fig 6-6; Fig 6-3D).

A series of deletion constructs that were shortened at the ends farthest from exon 1 were then cloned into the pGL3 basic vector (Fig 5-8B). These were designed for the key transcription factors necessary for Amot promoter activity. The full length reporter and the four deletion reporters were transfected into cells and they were measured for luciferase activity. This analysis found that the region between -563 and -1473 base pairs of the reporter is critical for basal Amot promoter activity, indicating the high significance of the transcription factor and polymerase binding that occupies that region. In contrast, it appears that the transcription factors that bind in the region between -1 and -563 are fully sufficient in activating the Amot promoter (Fig 5-9). This data aided in narrowing down the list of transcription factors that are key in the transcriptional regulation of the Amot isoforms.

5.4 Discussion

In this study, we sought to determine the regulatory mechanism governing the transcription of the unique isoforms of Amot: Amot 130 and Amot 80. The correlation of Total AMOT mRNA and protein levels with highly aggressive breast tumors, along with the numerous studies that debate the specific roles and functions of the Amot isoforms in cellular programs relevant to breast cancer indicate a strong need for a greater understanding of how these unique isoforms

are made at the transcriptional level [130,131]. Not only did we identify the single transcription start site of the *AMOT* gene, indicating that both isoforms are indeed controlled by a single promoter (Fig 5-3; 5-4), we have determined that these unique gene products are generated through alternative splicing (Fig 5-2; 5-5). Our data strongly demonstrated that the *AMOT* gene is spliced in the following way: Exon 1-2 splices directly into exon 5 for the production of the dominant negative Amot 80 isoform. The excision of exon 4 from Amot 80 is a key event in controlling the translation to favor Amot 80 expression, as the start methionine responsible for the translation of the Amot 130 isoform is present in exon 4. Therefore, Amot 130 undergoes no splicing; its mRNA contains all 12 exons (Fig 5-6). Our appreciation of the unique exons comprising the Amot isoforms led us to create Amot isoform specific qRT-PCR primer sets that will allow us to distinguish Amot 130 and Amot 80 transcript levels (Fig 5-7B). The generation of this reagent may be a key method in determining what is driving the alternative splicing to favor one isoform over the other, as well as understanding how the ratio of Amot 130 to Amot 80 transcript and protein levels contribute to breast cancer. Because Total *AMOT* mRNA levels have been shown to correlate strongly with reduced survival of breast cancer patients [130], the detection of the Amot isoform transcript ratio could become an even more specific diagnostic tool as we discover more about the distinct roles of the isoforms in breast cancer. Additionally, our work identified and fully mapped out the key regulatory region for the *AMOT* gene (Fig 5-8A), and we have begun to narrow down the identities of several transcription factors that appear to be greatly responsible for Amot

promoter activity (Fig 5-8; 5-9). The results from this study have provided a number of insights to determine what controls the expression of the Amot isoforms.

**CHAPTER 6: SPECIFICITY PROTEIN 1 INDUCES THE EXPRESSION OF
ANGIOMOTIN IN RESPONSE TO IL-6/STAT3 ACTIVATION TO MEDIATE
YAP1 DEPENDENT GROWTH OF BREAST CANCER CELLS**

6.1. Introduction

An inflammatory tumor microenvironment secretes a variety of cytokine effectors. Some of these include Interferon gamma $IFN\gamma$, tumor necrosis factor alpha ($TNF\alpha$), and interleukin 6 (IL-6). All three of these cytokines correlate with the 50 % of DCIS cases with inflammatory microenvironments and have been reported to promote the progression of breast cancer [38,121,173-176]. IL-6 and $IFN\gamma$ have both been shown to innervate the promotion of growth and survival through the STAT family members, the activation of which has been shown to foster the nuclear accumulation of YAP1 [121,177]. The mechanism of signaling between the activation of STAT3 and the translocation of YAP1 has not been investigated. As we have discussed the significance of the Amot isoforms in the control of YAP1 nuclear translocation, we sought to answer whether Amot is required for STAT3 induced YAP1 activation.

6.2 Methods and Materials

3-Dimensional Matrigel© Culture

Matrigel© was thawed from $-20\text{ }^{\circ}\text{C}$ on ice for a duration of 4 hours. Matrigel© was then plated and incubated at $37\text{ }^{\circ}\text{C}$ for a duration of 5 minutes. Approximately 250,000 cells were seeded into the Matrigel© and covered in media until the Matrigel© was submerged. Cells were cultured for a duration of four days, and media was changed once every 2 days. Cultures were then harvested for RNA and/or protein for analysis.

Interleukin (IL-6) Treatment Assays

Interleukin 6 (IL-6) (PeproTech) was diluted to 1 µg/mL stock in 0.2% bovine serum albumin (BSA) / water and stored at -80 °C until use. Per PeproTech's records, this lot of IL-6 scored a 50% active concentration (AC₅₀) of 0.1 ng/mL for a duration of 64 hours. For multi-day assays, IL-6 media was changed once every 48 hours to ensure consistent molecular activity. IL-6 was diluted to the following concentrations in Optimem © for various assays: 0.03 ng/mL, 0.1 ng/mL, 0.3 ng/mL, 1.0 ng/mL, 3.0 ng/mL, 10 ng/mL, and 100 ng/mL. Vehicle control media was prepared with BSA to mimic the highest concentration of IL-6 being tested. For 3-dimensional Matrigel© assays, IL-6 and BSA Vehicle were diluted in Complete DMEM for MCF7 and MDA-MB-468 cells, or Complete Matrigel© Assay Medium (MCF10A media supplemented with 5% Matrigel©) for pre-tumorigenic MCF10A cells.

Verteporfin Treatment Assays

Verteporfin was diluted to 1M in a DMSO stock and stored at -80 °C until use. It was diluted to a concentration of 1 µM for cell based assays. Control cells were treated with DMSO. Verteporfin and control media was changed once every 48 hours to ensure high activity. Detection of CTGF levels via qRT-PCR confirmed reduced YAP1-TEAD transcriptional targets in response to Verteporfin.

Mithramycin Treatment Assays

Mithramycin was obtained from Dr. Mircea Ivan's laboratory (IUSM) at a 20M DMSO stock. It was diluted to a concentration of 20 mM for cell based assays. Control cells were treated with DMSO. Mithramycin and control media was changed once every 24 hours to ensure high activity. Immunoblot confirmed reduced Sp1 levels in response to Mithramycin.

C188-9 Treatment Assays

C188-9 STAT3 inhibitor was obtained from Dr. Teresa Zimmers laboratory (IUSM) and was diluted to a stock concentration of 30 mM. It was diluted to a concentration of 30 μ M for cell based assays. Control cells were treated with DMSO. C188-9 and control media was changed once every 24 hours to ensure high activity. Immunoblot confirmed reduced STAT3 levels in response to C188-9.

Tissue Digestion and Harvest

Mouse myocardial STAT3 WT and KO tissues were obtained from Dr. Xin-Yuan Fu's laboratory (IUSM) and post hepatectic and control mouse muscle tissues were obtained from Dr. Teresa Zimmer's laboratory. In both instances, tissue samples were transferred back to the Wells' lab in liquid nitrogen. The frozen tissue was ground with a cold mortar and pestle and transferred to round bottom tubes for sonication and homogenization in 2 mLs of Tri-Reagent. RNA extraction proceeded as described in Chapter 2 of this dissertation.

Stereo Imaging

Stereo imaging was conducted on a Nikon SMz 1500 Model C-BD115 120V, 50-60 Hz under 10X or magnifications.

Quantification of Stereo Imaging

ImageJ software was used to quantify the cross-sectional area (in pixels²) of 3-D mammary acinar colonies cultured in Matrigel®.

6.3 Results

Our initial investigation into the potential convergence of inflammation with the dysregulation of HIPPO signaling examined the impacts of various cytokines that are commonly found in breast cancers on the Amot promoter activity, as well as YAP1 and TAZ protein levels in MDA-MB-468 cells. Interleukin 6, Tumor Necrosis Factor- α , and Interferon- γ are three commonly secreted cytokines found to correlate in aggressive breast cancers. We found that the cytokine that induced the greatest impact on both Amot promoter activity and YAP1 and Taz protein expression levels was IL-6. IFN γ and TNF α showed no increase in YAP1 levels and only IFN γ showed an increase in Amot promoter activity (Fig 6-1A; B). This IL-6 data is in agreement with the studies showing the requirement of YAP1 in liver regeneration, a process tightly controlled by IL-6 [118,178,179]. Additionally, YAP1 levels were seen to increase dramatically in post hepatectomized livers, in direct correlation with PSTAT3 levels [180-182]. In collaborative work with Dr. Teresa Zimmers, we examined the changes in the levels of YAP1 target

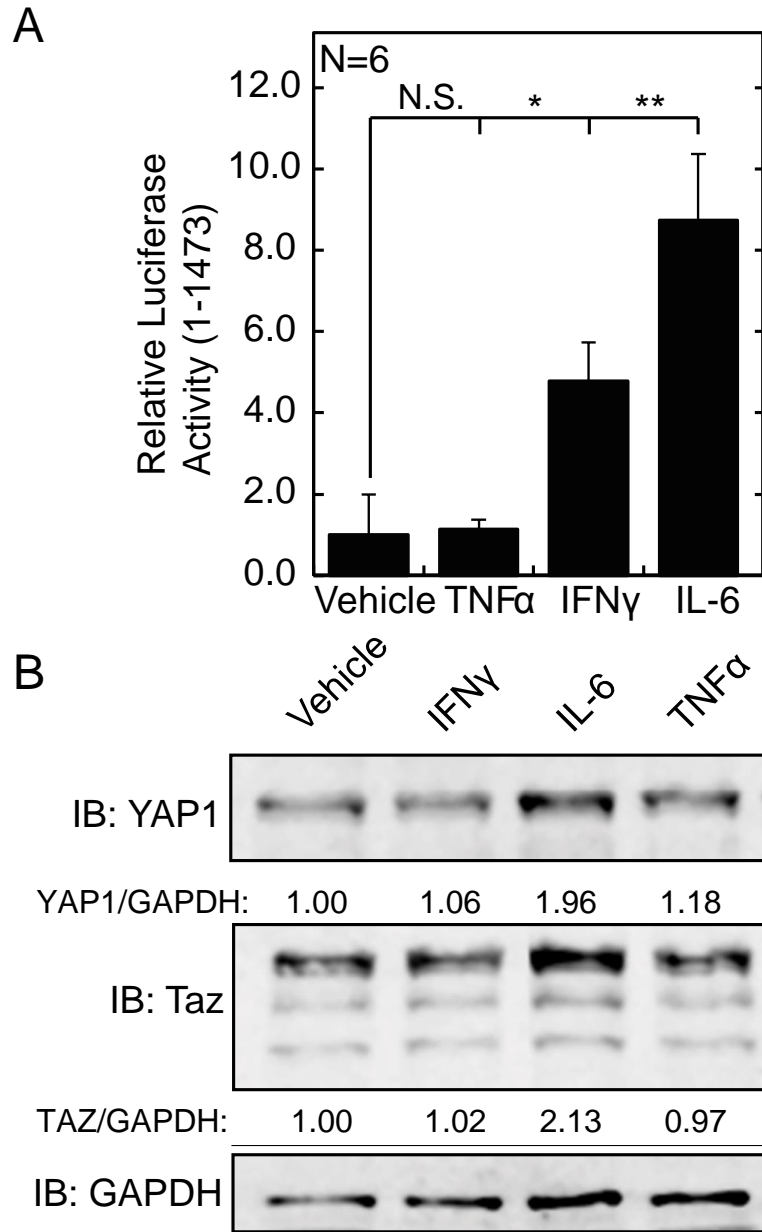


Figure 6-1. Of the three most common cytokines found in breast cancer, IL-6 induced the greatest elevation of Amot promoter activity as well as YAP1 and Taz protein levels. A. The full length Amot promoter luciferase construct was transfected into HEK 293T cells and treated with 0.5 ng/mL TNF α , IFN γ , IL-6, or 0.1% BSA/DMSO control for a duration of 20 hours and luciferase activity was detected. N=6, S.E., Student's t-test, *p < 0.01. B. MCF10A cells treated with TNF α , IFN γ , IL-6, or 0.1% BSA/DMSO control for a duration of 24 hours were harvested for immunoblot and probed for YAP1, Taz, and GAPDH loading control.

gene *CTGF* in the cachexic muscle tissue of post hepatectomy mice as compared to controls. Liver regeneration is widely implicated in driving up serum IL-6 concentrations, leading to the direct induction of muscle tissue de-differentiation rendering muscles cachexic [183]. In the post hepatectomy muscle tissue, we saw a marked increase in *CTGF* and *TOTAL AMOT* transcript levels, correlating with the elevated levels of known cachexia marker *PAX7*, when compared to control tissue (Fig 6-2) [184]. This work demonstrated the first connection of pro-inflammatory signaling to the de-differentiation of tissue and the dysregulation of HIPPO signaling to favor the production of *CTGF* via elevated *AMOT* levels. We thus sought to explore this connection in breast cancer cells.

In order to determine that the increase of *CTGF* transcript levels by IL-6 is indeed YAP1 dependent, YAP1 nuclear translocation in response to IL-6 was detected via fixed-cell immunofluorescent staining of YAP1. Treatment with IL-6 resulted in a dramatic increase in the presence of YAP1 (shown in green) inside the nucleus (stained in blue) (Fig 6-3A). Intra-nuclear YAP1 has been verified to correlate with a pro-growth and –survival phenotype, where it functions as a transcriptional co-activator of many transcription factors, which, in turn, stimulates the expression of genes that foster growth and anti-apoptotic cell programming. Ectopic expression of CA-STAT3 resulted in an increase in total YAP1 levels and a marginal decrease in the ratio of phosphorylated YAP1 over Total YAP1 (Fig 6-3B). The phosphorylated state of YAP1 has been verified to remain cytosolic, rendering the coactivating function of nuclear YAP1 inoperable [185]. Likewise, we saw no change in the ratio of phosphorylated LATS1 over

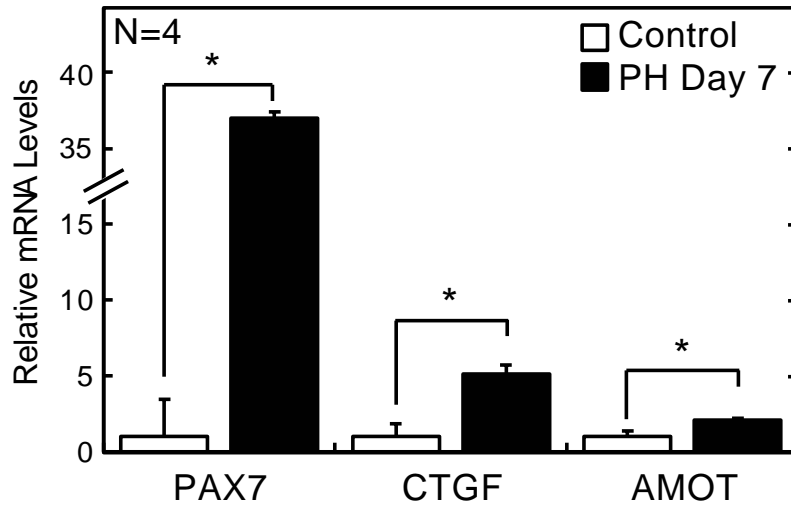


Figure 6-2. CTGF and Amot mRNA levels correlate with positive cachexia marker Pax7 in muscle tissue from post-hepatectomic mice. Muscle tissue was extracted from mice seven days after undergoing partial hepatectomies (PH Day 7) or control mice. These tissues were harvested and analyzed for measured for *CTGF*, *TOTAL AMOT* and muscle cachexia marker *PAX7*, mRNA levels via qRT-PCR. N=4, S.E. Student's t-test, *p < 0.005.

total LATS1 in the same cells, highlighting that the impact of IL-6 on HIPPO signaling is likely innervates another HIPPO protein (Fig 6-3B). Conversely, total YAP1 levels were also found to be reduced upon the silencing of STAT3 by shRNA (Fig 6-3C). These data were further supported by the data showing that CTGF mRNA levels were increased in response to treatment with IL-6, and decreased in response to the silencing of STAT3 by shRNA (Fig 6-3D;E). Note that the elevated CTGF levels also correlated with enhanced growth of normal mammary acini induced by IL-6 (Fig 6-3D).

Taking into account that the impact of IL-6 on YAP1 is not through the deactivation of the LATS1 kinase, along with the preliminary data showing the enhanced Amot promoter activity and total transcript levels by IL-6, we sought to further study the impact of IL-6 on Amot-dependent YAP1 activity. Firstly, we investigated whether modulations in the IL-6 pathway produced differential effects on the levels of Amot 130 versus Amot 80 transcript levels. The levels of *AMOT 130*, *AMOT 80*, *TOTAL AMOT*, and *STAT3* transcripts were compared between a mouse myocardial STAT3 knockout (KO) and wild type (WT) control mouse. While we found that all *AMOT* transcripts correlated strongly with *STAT3* levels, these data demonstrated no distinguishable difference between the effects of IL-6 pathway modulation on *AMOT 130* versus *AMOT 80* transcript levels (Fig 6-4A; B). This implied that alternative splicing of the *AMOT* gene was not affected by the activation or silencing of STAT3, and thus we sought no reason to study this further. For all remaining experiments, we decided to focus on detecting only the *TOTAL AMOT* transcript levels. In response to IL-6

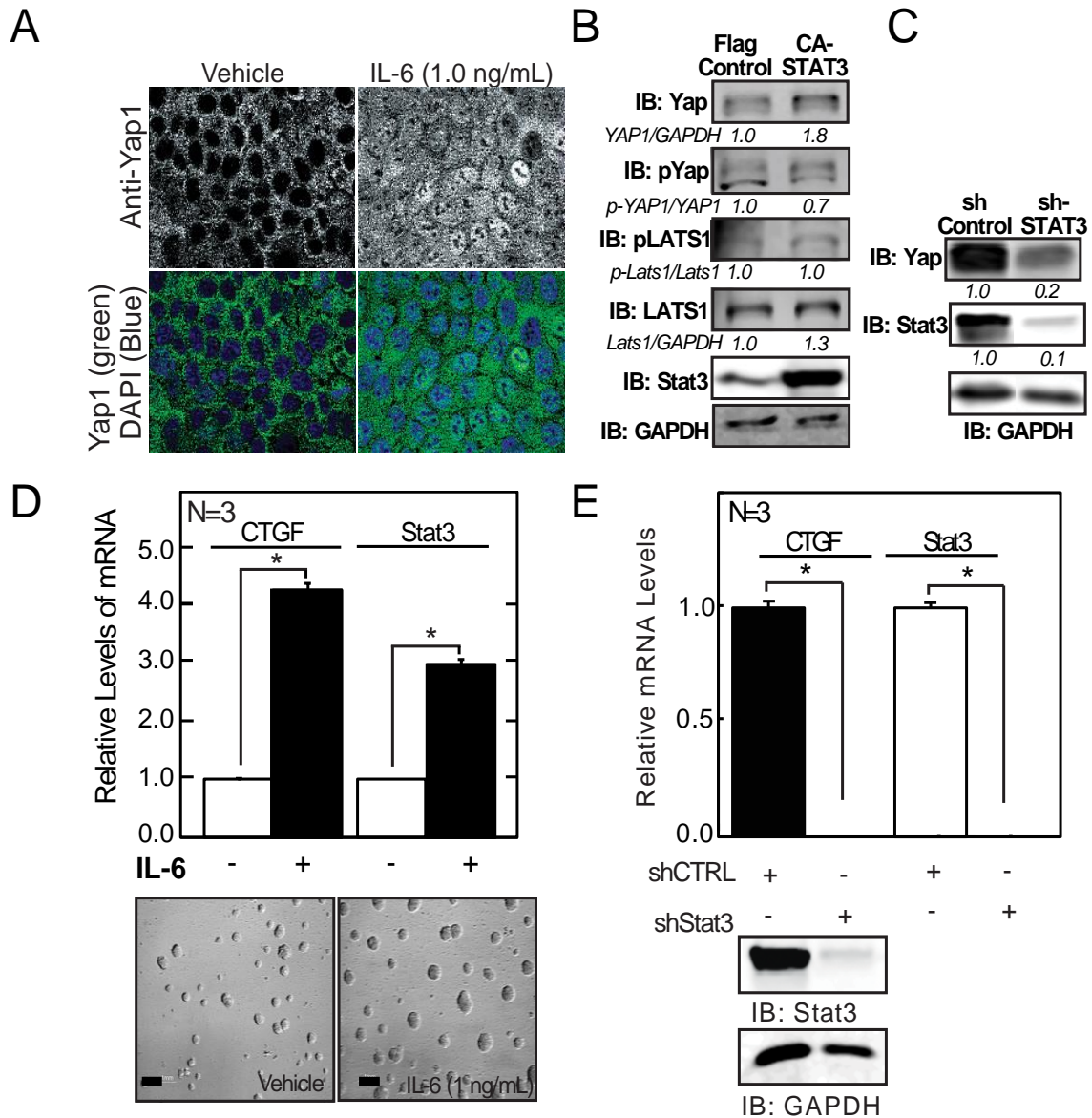


Figure 6-3. IL-6 drives the nuclear translocation of YAP1, elevates YAP1 levels and increases the levels of YAP1 target gene CTGF through the activation of STAT3, independently of LATS1. A. MCF7 cells were plated onto glass coverslips, treated with IL-6, PFA fixed and stained for YAP1 (in green) and nuclei (in blue). B-C. MDA-MB-468 cells stably expressing the constitutively active form of STAT3, STAT3 shRNA, or control were harvested for immunoblot and probed for HIPPO pathway proteins and GAPDH loading control. D. MCF10A cells treated with IL-6 and grown in a laminin rich 3D Matrigel© environment were imaged and then harvested and measured for CTGF and STAT3 mRNA levels via qRT-PCR. N=3. SD. * $p \leq 0.01$. E. STAT3 depleted (shRNA) MDA-MB-468 cells were harvested and measured for CTGF and STAT3 mRNA levels via qRT-PCR. N=3. SD. * $p \leq 0.01$.

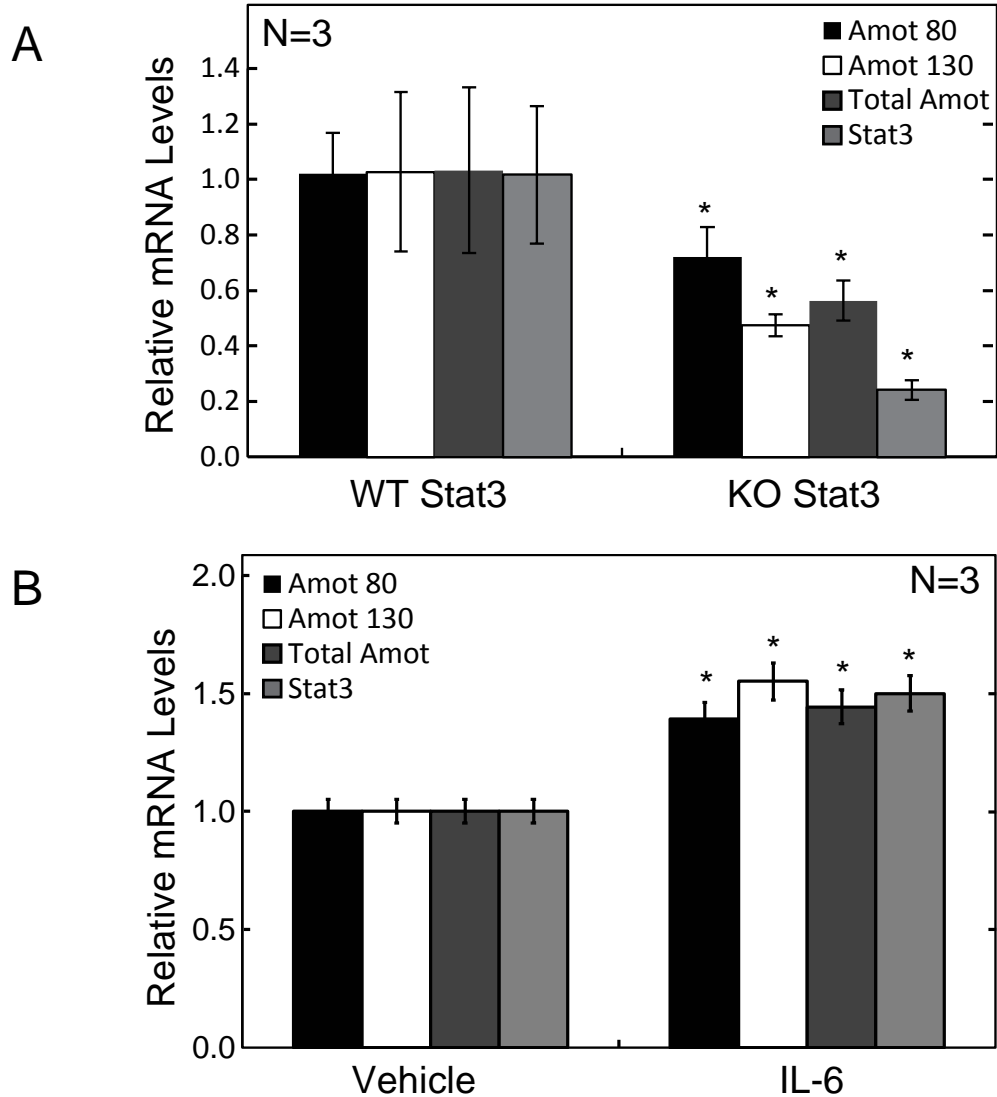


Figure 6-4. The Amot isoform-specific transcripts are not differentially regulated by IL-6/STAT3 signaling. A-B. *AMOT 80*, *AMOT 130*, *TOTAL AMOT*, and *STAT3* mRNA were detected in hearts from mice expressing a myocardial *STAT3* adenoviral knockout genotype and compared to wild type (A) or MDA-MB-468 cells treated with 0.1 ng/mL IL-6 for a duration of 24 hours. N=3, S.D., Student's t-test, * $p < 0.01$.

treatment, Total Amot transcript levels correlated strongly with *STAT3* transcript levels in MDA-MB-468 cells (Fig 6-5A), which are canonically increased in response to IL-6 activated signaling. This demonstrates that IL-6 signaling has a transcriptional impact on Amot expression.

Additionally, treatment with increasing concentrations of IL-6 for a duration of 24 hrs was found to enhance the protein expression of both Amot 130 and Amot 80 in MDA-MB-468s (Fig 6-5B). This increase in Amot protein levels occurred only after an IL-6 treatment duration of at least 12 hours and most strongly after 24 hrs, indicating an indirect activation (Fig 6-5C). Furthermore, the ectopic expression of CA-STAT3 yielded an increase in both Amot isoform protein and transcript expression (Fig 6-6A). The silencing of STAT3 via shRNA or STAT3 inhibitor (C188-9) resulted in reduced *TOTAL AMOT* transcript and protein levels in MDA-MB-468 cells, even in response to IL-6 treatment (Fig 6-6C-D). This data supports the requirement of STAT3 for the increase of Total Amot resulting from IL-6. Additionally, exogenous expression of a dominant negative form of STAT3 (D.N. STAT3) also resulted in a dramatic reduction of Amot protein levels (Fig 6-6B). For this reason, the postulation of a potential transcriptional effect of IL-6 signaling on Amot expression arose.

To understand the potential mechanism of Amot transcriptional activation in response to IL-6, the promoter of Amot was investigated. Treatment of cells transfected with the full length Amot promoter with IL-6 resulted in a greater than 3-fold activation over cells treated with vehicle control. Treatment with STAT3 inhibitor C188-9 alone yielded no activation over control, and a combined

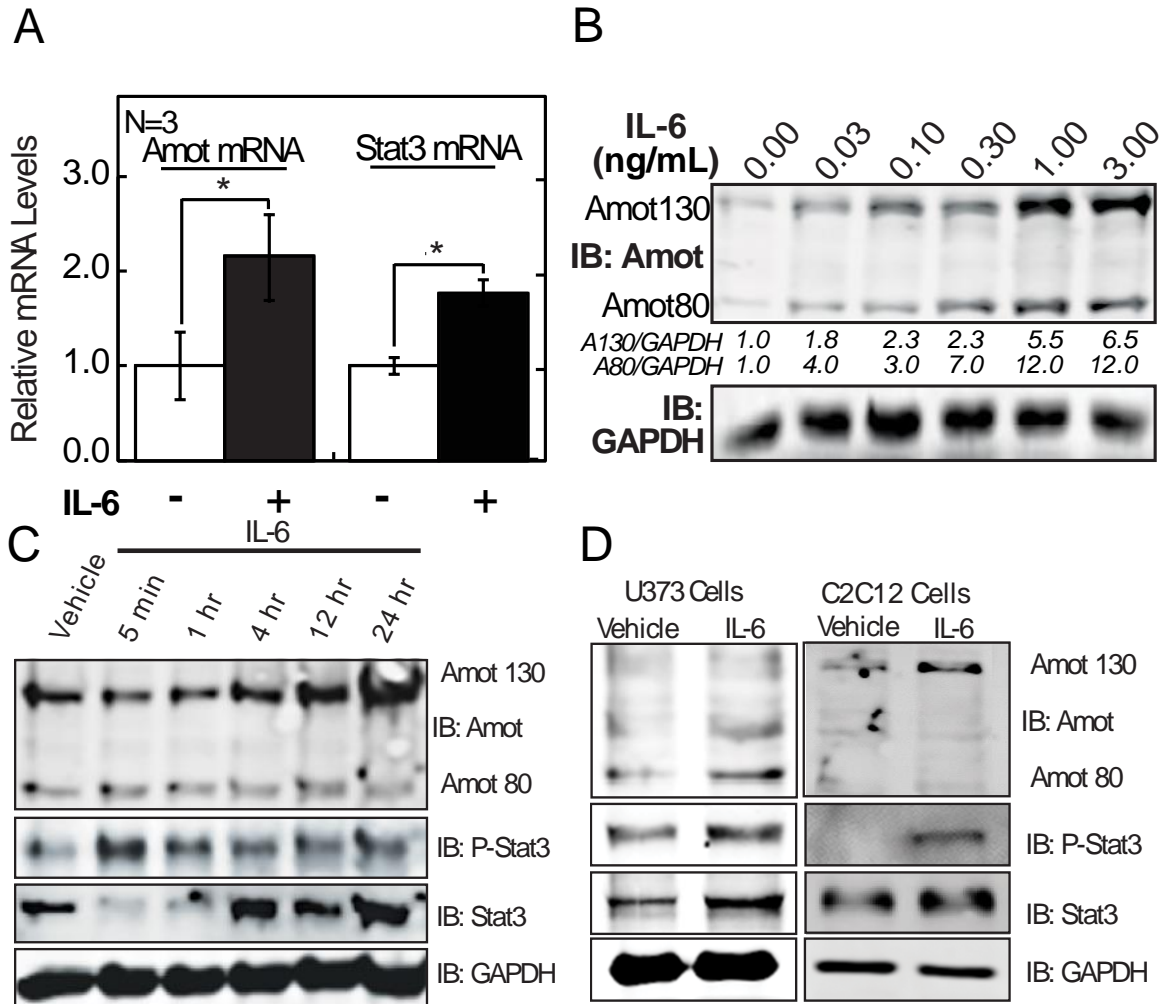


Figure 6-5. Treatment with IL-6 correlates with elevated Total Amot transcript and Amot p130 and Amot p80 protein levels. A. MDA-MB-468 cells treated with 0.1 ng/mL IL-6 for a duration of 24 hrs were harvested and measured for *CTGF* and *STAT3* mRNA levels via qRT-PCR. N=3. SD. * $p \leq 0.01$. B. MDA-MB-468 cells were treated with increasing concentrations of IL-6 for a duration of 12hrs, harvested for immunoblot, and probed for Amot and GAPDH loading control. C. MDA-MB-468s treated with 0.1 ng/mL IL-6 for variable durations of time (5 minutes-24 hours) were harvested for protein and probed for Amot, P (Y705) STAT3, STAT3, and GAPDH loading control.

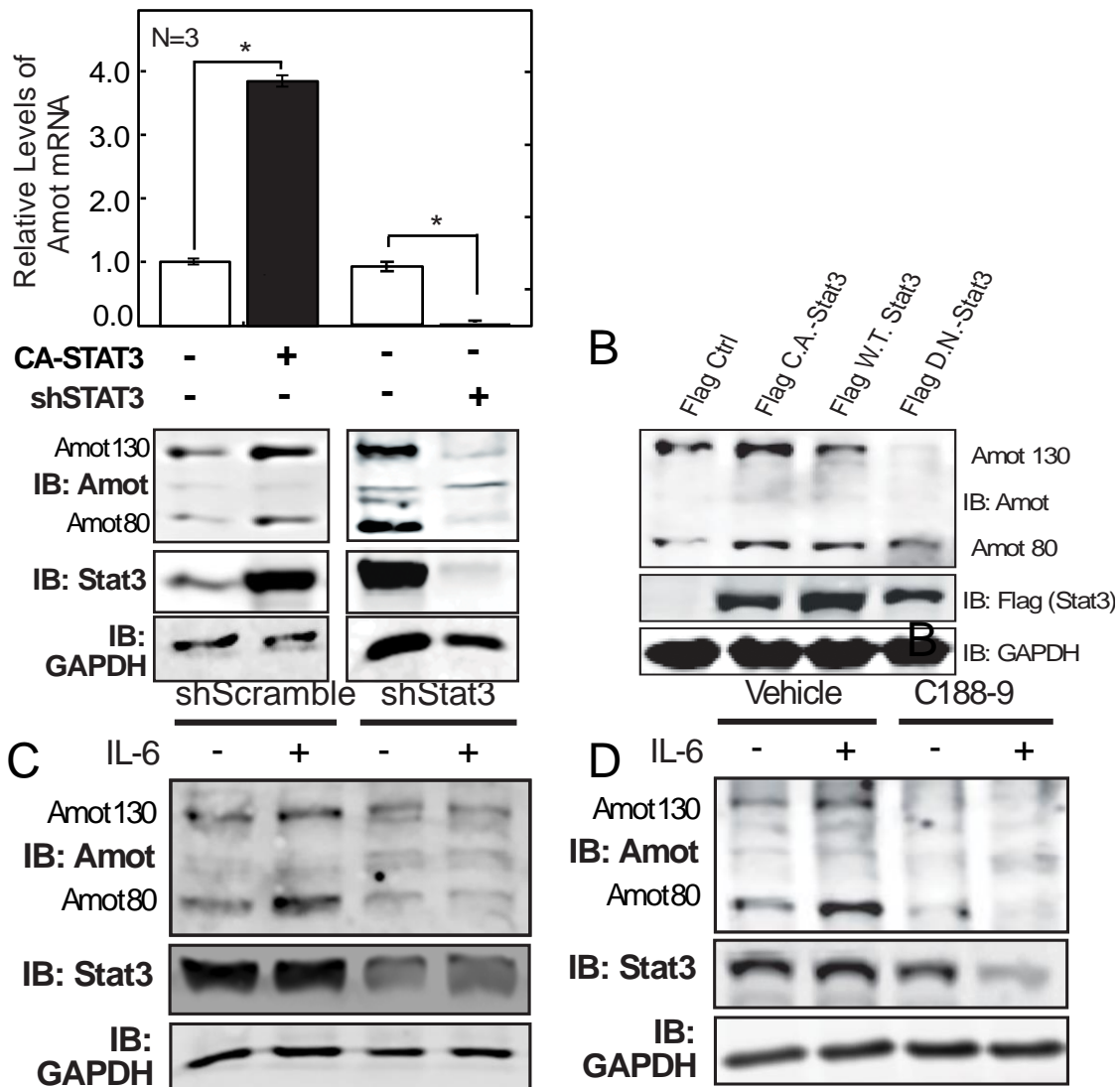


Figure 6-6. The elevation of Amot transcript and protein levels by IL-6 requires the activation of STAT3. A. MDA-MB-468 cells stably expressing constitutively active STAT3 (CA-STAT3), STAT3 shRNA, or control were harvested for immunoblot and probed for Amot, STAT3, and GAPDH loading control and measured for *CTGF* and *STAT3* mRNA levels via qRT-PCR. N=3. SD. * $p \leq 0.01$. B. MDA-MB-468 cells stably expressing the following flag-tagged forms of STAT3: CA-STAT3, wild type (WT STAT3), dominant negative (D.N. STAT3) were harvested for immunoblot and probed for Amot, Flag, and GAPDH loading control. C. MDA-MB-468 cells in 2-D culture infected with shScramble or shSTAT3 lentivirus and treated with 0.1 ng/mL IL-6 were harvested for protein and probed for Total Amot, STAT3, and GAPDH loading control. D. MDA-MB-468 cells in 2-D culture treated with 0.1 ng/mL IL-6, 30 μ M C188-9 STAT3 inhibitor, IL-6 and C188-9, or 0.1% BSA/DMSO control for 24 hours were harvested for protein and probed for Amot, P(Y705)-STAT3, STAT3 and GAPDH loading control.

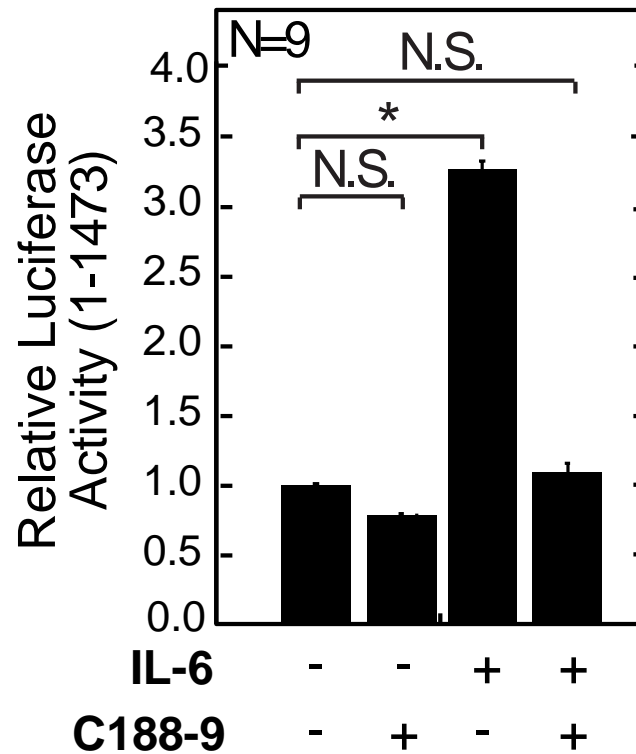


Figure 6-7. IL-6 elevates the Amot promoter activity above basal levels through STAT3. The full length Amot promoter luciferase construct was transfected into HEK 293T cells and treated with 0.5 ng/mL IL-6, 30 uM C188-9 STAT3 inhibitor, IL-6 and C188-9, or 0.1% BSA/DMSO control for a duration of 20 hours and luciferase activity was detected. N=9, S.E.M., Student's t-test, *p < 0.01.

treatment of IL-6 and C188-9 also yielded no activation (Fig 6-7). These data not only indicate the robust ability of IL-6 to activate the Amot promoter, but further demonstrate the requirement of active STAT3 to induce this effect. Commonly, this signaling induces transcriptional activation through the binding of phospho-STAT3 homodimers to promoters [83]. Interestingly, the ENCODE database lacked any occurrence of STAT3 in the active chromatin region of the Amot promoter that comprises this reporter construct (Fig 6-8A). This demonstrated the need to further analyze the transcription factors that do occur in this region and their responsiveness to IL-6/STAT3 signaling. To narrow down the search, four serial deletions of the reporter construct were transfected into cells treated with IL-6 or vehicle control and tested for luciferase activity. The full length Amot promoter construct was activated by IL-6 as expected. In addition, a deletion of 394 base pairs from the 5' end of the full length promoter construct was still responsive to IL-6, despite a reduced basal activation. Finally, the remaining serial deletion constructs were no longer IL-6 responsive. The basal promoter activity was also nearly completely lost once 910 base pairs from the 5' end of the full length was deleted (Fig 6-8B). These data indicated that the most relevant region of the Amot promoter with respect to responsiveness to IL-6 treatment occurs between locales -1079 and -770 base pairs (Fig 6-8A; B). As discussed in Chapter 5, data obtained from ENCODE's Chip-Sequencing catalog revealed the identities of the transcription factors that bind this critical region as NFYA, MAZ, NFYB, IRF1, Sp2, FOS, PBX3, ZBTB7A, and Sp1 (Fig 5-8A). The factors occurring in this region that have demonstrated activation in response to

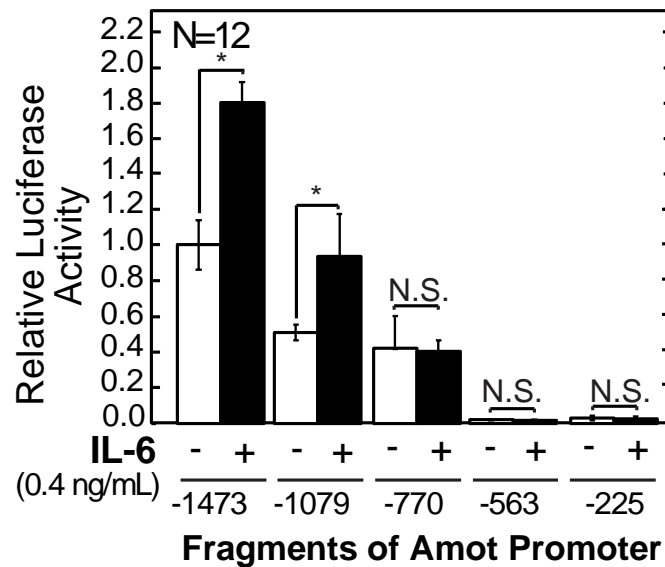
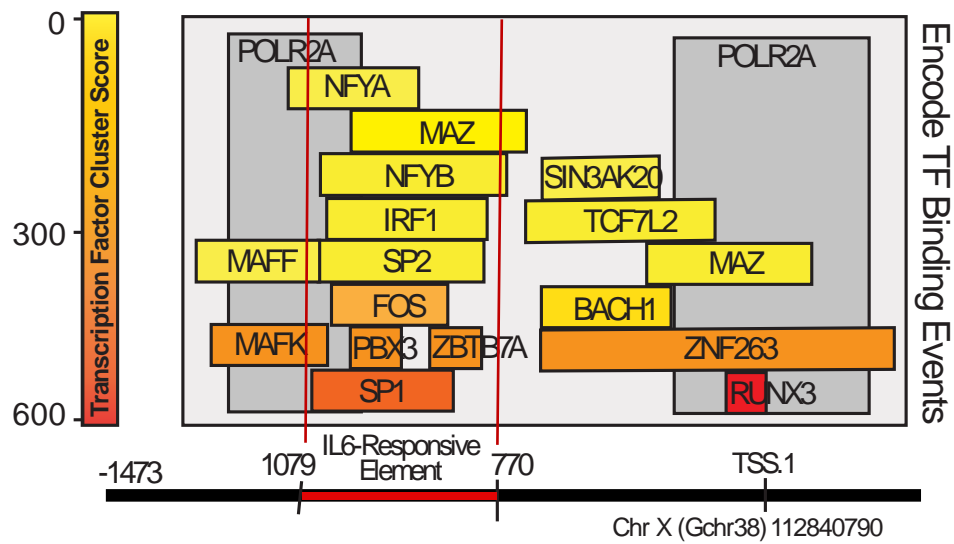


Figure 6-8. The Amot promoter is activated by IL-6 within a responsive region between -770 and -1079 bps. The serial deletion constructs (-1079, -770, -563, -225) in addition to the full promoter (-1473) were each transfected into HEK 293T cells and treated with 0.5 ng/mL IL-6 or vehicle control for a duration of 20 hrs and measured for luciferase activity. N=9, S.E., Student's T-test, *p < 0.01. The transcription factors binding the predominant IL-6 responsive region between -770 and -1079 were mapped.

IL-6 are interferon regulatory factor 1 (IRF1) and Specificity Protein 1 (Sp1) [87,88,93,94,173,186-188]. Likewise, ENCODE revealed that of all the factors binding the IL-6 responsive element, Sp1 exhibited the greatest cluster score, a measurement representing the signal strength detected via transcription factor Chip-Sequencing experiments. Finally, data from over 700 breast cancer tissue samples in The Cancer Genome Atlas (TCGA) showed the positive correlation between *AMOT* and *SP1* transcript levels. It can be noted here that the majority of the >700 breast tumor tissues analyzed in the TCGA came from surgical excisions of DCIS tumors. This was also matched with a significant positive correlation with *STAT3* transcript levels, a canonical transcriptional output from IL-6 stimulation. (Fig 6-9). Literature demonstrated that active STAT3 not only stimulates the nuclear translocation of Sp1, but also correlated with elevated Sp1 transcript and protein expression [87,88,93,186]. Taken together, these pieces of evidence lend strong support to the hypothesis that IL-6 activates STAT3 to foster enhanced Sp1 transcription factor binding to the *Amot* promoter and subsequent activation of *Amot* expression.

The importance of Sp1 binding to the *Amot* promoter was investigated via testing the impact of point mutations in the five SpX motif sites (GGGCGGG) occurring within the IL-6 responsive element on the ability of IL-6 to induce promoter activation. Through the detection of luciferase activity, cells transfected with the 5X Sp1 mutant promoter revealed a dramatic reduction in the activation of the *Amot* promoter in response to treatment with IL-6 as compared to treatment of cells expressing the control promoter (Fig 6-10A). The wild type

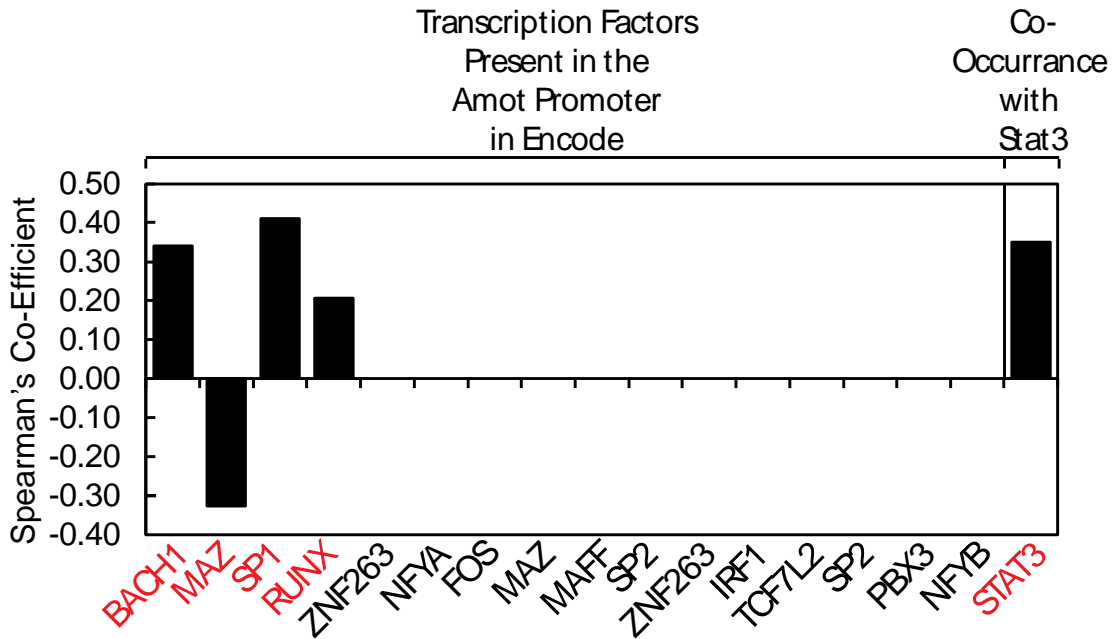


Figure 6-9. Amot transcript levels significantly correlate with the transcript levels of the Amot promoter transcription factor binders BACH1, MAZ, SP1, and RUNX as well as STAT3 transcript levels in breast cancer tumors. Analysis of >700 breast tumor tissues in The Cancer Genome Atlas (TCGA) sought out significant correlations ($\geq \pm 0.3$) between the transcript levels of *AMOT* and the transcript levels of the transcription factors found to bind the Amot promoter. High correlative transcripts are labelled in red, and the correlation between *AMOT* and *STAT3* transcript levels was also highlighted. *MAFK*, *SIN3AK20*, and *ZBTB7A* are not present in TCGA and thus were unable to be analyzed.

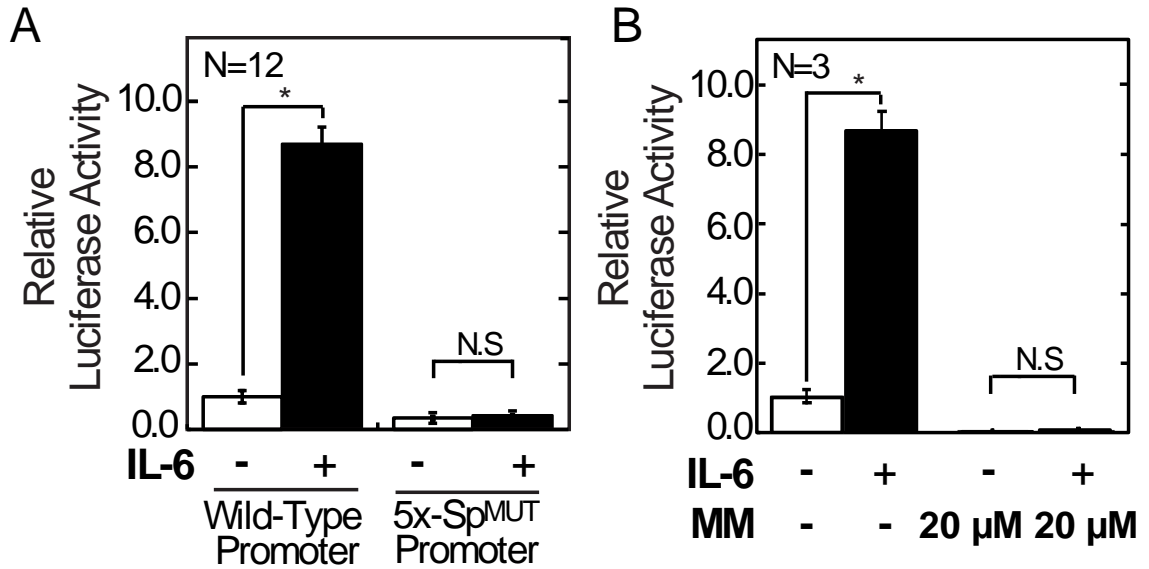


Figure 6-10. Sp1 is required for the induction of Amot promoter activity by IL-6. A. HEK 293T cells transfected with an Amot promoter luciferase construct in which all five Sp GC box binding motifs existing in the IL-6 responsive element were mutated and were treated with 0.5 ng/mL IL-6 or vehicle control for a duration of 20 hrs. Luciferase activity was measured and compared to the wild type Amot promoter. N=12, S.E., Student's t-test, *p < 0.01. B. HEK 293T cells were transfected with the full length Amot promoter, treated with 0.5 ng/mL IL-6, 20 μ M Mithromycin (MM), IL-6 and MM, or vehicle control for a duration of 20 hrs, and measured for luciferase activity. N=3, S.E., Student's t-test, *p < 0.01.

promoter was also tested against treatment with 20 μ M Mithramycin (MM) in the presence or absence of IL-6 (Fig 6-10B). MM is an antibiotic produced by *Streptomyces argillaceus* that inhibits transcription factor binding to GC-rich motifs in a competitive manner [91,189,190]. It is in this way that MM prohibits Sp1 DNA binding capacities and has lended itself to a wide variety of anti-cancer studies in every tissue type from the breast and cervix to the bones and brain [89-92,189-192]. Comparable to the impact of Sp GC motif point mutants on Amot promoter activity, treatment with MM on top of IL-6 inhibited the ability of IL-6 to activate the Amot promoter (Fig 6-10B). As a follow up to this result, the impact of infection of Sp1 short hairpin RNA (shRNA) lentivirus and MM treatment on Amot transcript and protein levels was detected via RT-PCR and immunoblot. These data yielded a reduction of Amot transcript levels in both cases of Sp1 disruption (Fig 6-11A-B).

Studies have shown the requirement of Sp1 in the activation of CTGF [193-195]. These studies focus on the fact that Sp1 binds the promoter of CTGF. ENCODE shows that Sp1 binds the CTGF promoter with a cluster score of 477 out of 1000 [96]. Here, we show that the induction of CTGF transcription by IL-6 was inhibited by the silencing and inactivation of Sp1 by shRNA in both SKBR3 (Her2+) and MCF7 (ER+) cells (Fig 6-12A; B; 6-13B). In addition, the IL-6 induced growth phenotype was also mitigated by the silencing of Sp1 by shRNA in Her2+ breast cancer cells (Fig 6-13A; C). These data are in agreement with that from multiple groups that have shown that Sp1 is required for the induction of growth by pro-inflammatory factors [74,89,90,92,195]. In parallel, the

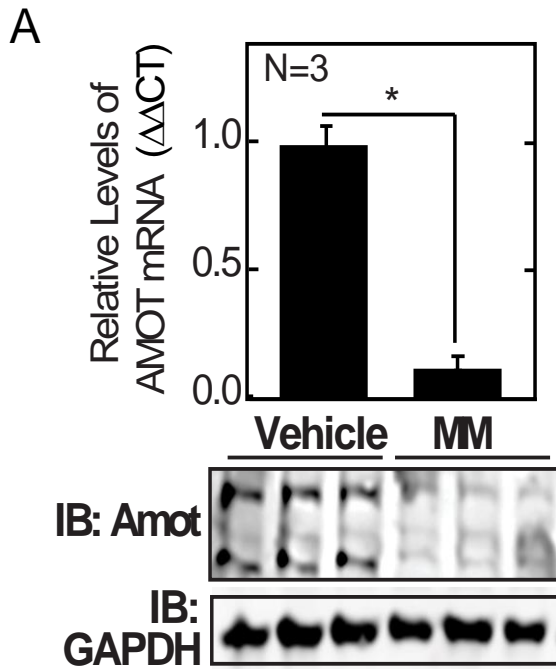
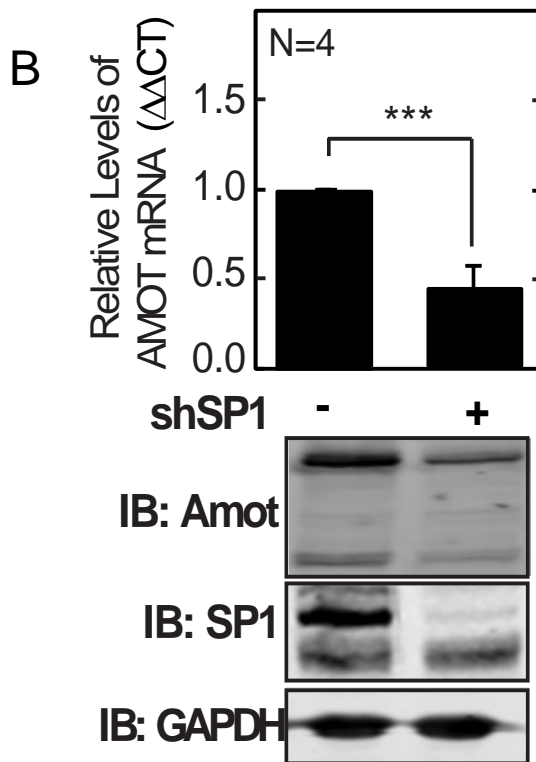


Figure 6-11. Sp1 is required for Amot expression. A. MDA-MB-468s were treated with 20 μM MM and measured for *TOTAL AMOT* mRNA and protein levels. N=3, S.D., Student's t-test, * $p < 0.01$. B. HEK 293T cells were infected with Sp1 shRNA lentivirus and measured for Total Amot mRNA and protein levels N=3, S.D., Student's t-test, * $p < 0.01$.



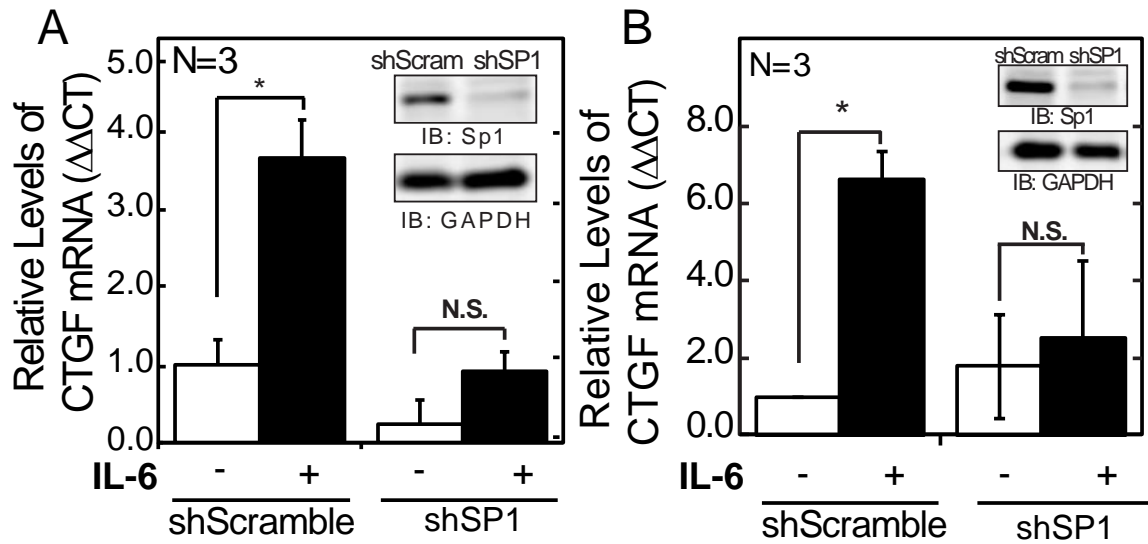


Figure 6-12. Sp1 depletion inhibits the elevation of CTGF transcript levels by IL-6. SKBR3 (A) and MCF7 (B) cells infected with Sp1 shRNA or shScramble virus were treated with 1 ng/mL IL-6 for a duration of 24 hours and harvested for RNA. The levels of *CTGF* and *STAT3* mRNA were detected via qRT-PCR. Silencing was confirmed by immunoblot.

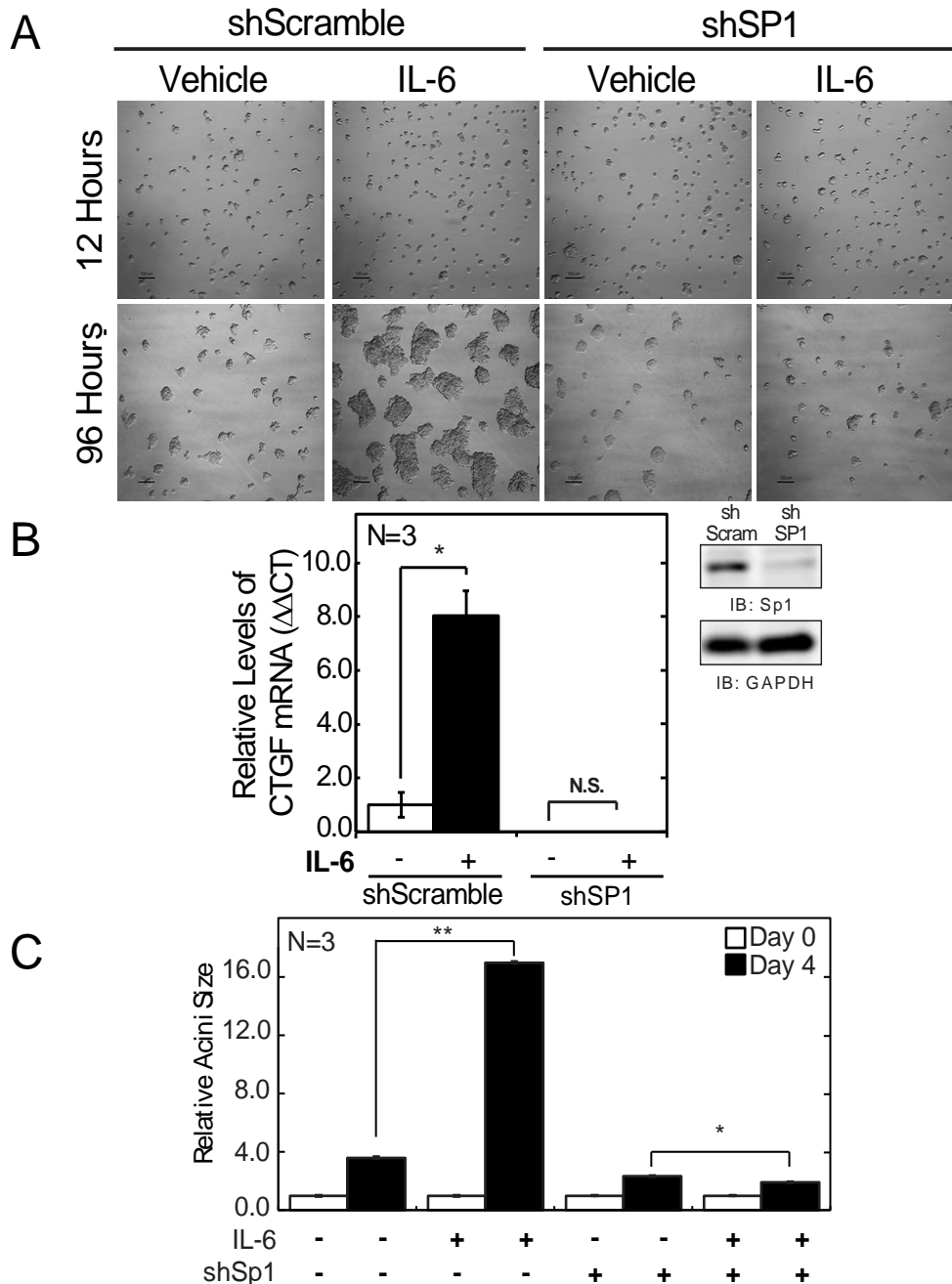


Figure 6-13. IL-6 requires Sp1 to induce CTGF transcription and growth in poorly differentiated Her2+ breast cancer cells. A-B. SKBR3 cells infected with Sp1 shRNA were seeded into a laminin-rich 3D Matrigel© environment, treated with 0.1 ng/mL IL-6 or vehicle control for a duration of 4 days, and measured for CTGF mRNA levels. N=3, S.D., Student's t-test, *p < 0.01. Cells were confirmed for silencing via immunoblot. C. Cells from A were imaged and the cross sectional area of the acini was quantified with ImageJ software. N=3, S.E., *p < 0.01, **p < 0.001. *Note: this experiment was attempted in MDA-MB-468 cells and yielded dramatic and rapid cell death.

significance of the Amot isoforms to this signaling was also demonstrated in cells infected with the Amot CRISPR, shRNA, or corresponding control plasmids, and treated with IL-6 or vehicle control. Upon the silencing of Amot, the induction of CTGF transcription by IL-6 was lost. This effect was seen in Amot silenced Her2+ and triple negative cells, where IL-6 also lacked the expansive growth phenotype seen in the control cells. (Fig 6-14; 6-15; 6-16). Unfortunately, our efforts to investigate whether IL-6 signaling favors the unphosphorylated form of the Amot p130 protein, and thereby enhancing its stability, remain unsuccessful. However, the dramatic loss of CTGF signaling upon the inhibition of the Amot TSS and a more than 50 % reduction in Amot transcript levels in the Amot CRISPR 1A cells indeed suggests the relevance of Amot promoter activity followed by elevated Amot transcription to this system (Fig 6-14). These data demonstrate two possible theories.

Treatment of YAP1-silenced cells with IL-6 not only resulted in a mitigated growth phenotype, but also exhibited reduced CTGF mRNA levels when compared to control cells (Fig 6-16A-C). Verteporfin (VP), an inhibitor of the YAP1-TEAD interaction currently employed in treating macular degeneration [196,197], was used to test the specific requirement of the YAP1-dependent coactivation of TEAD on the stimulation of CTGF transcript levels in response IL-6. Treatment with VP alone or VP in combination with IL-6 demonstrated that the inhibition of the coactivation of TEAD by YAP1 and subsequent lack of CTGF transcript elevation may be sufficient to mitigate the IL-6 growth phenotype (Fig

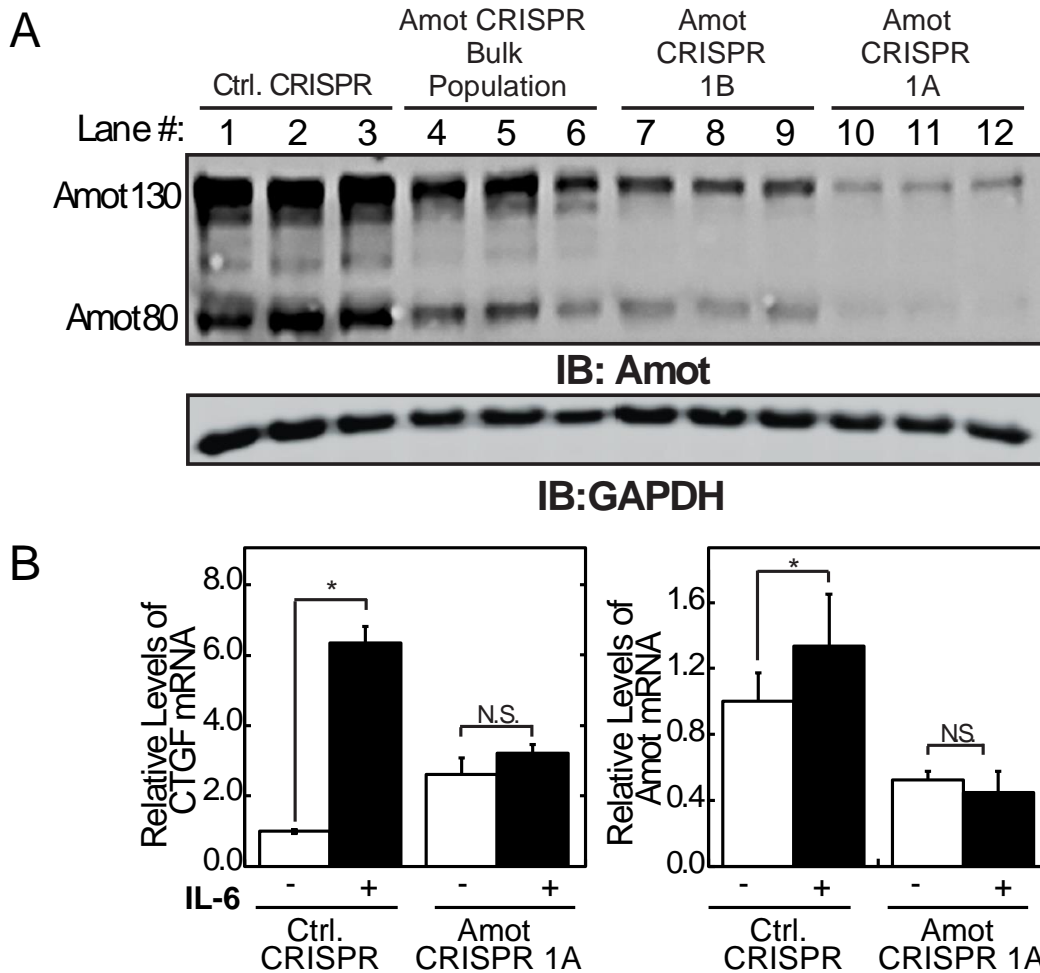


Figure 6-14. The inactivation of Amot by CRISPR inhibits the elevation of CTGF by IL-6. A. HEK 293T cells infected with Amot CRISPR 1 were puromycin selected and clones were picked (CRISPR clone 1A or CRISPR clone 1B) or allowed to establish a bulk population. Cells were harvested for protein and probed for Amot and GAPDH loading control. B. CRISPR clone 1A and control cells from (A) treated with 1 ng/mL IL-6 for a duration of 24 hours were harvested for RNA and of CTGF and Amot mRNA levels were detected via qRT-PCR.

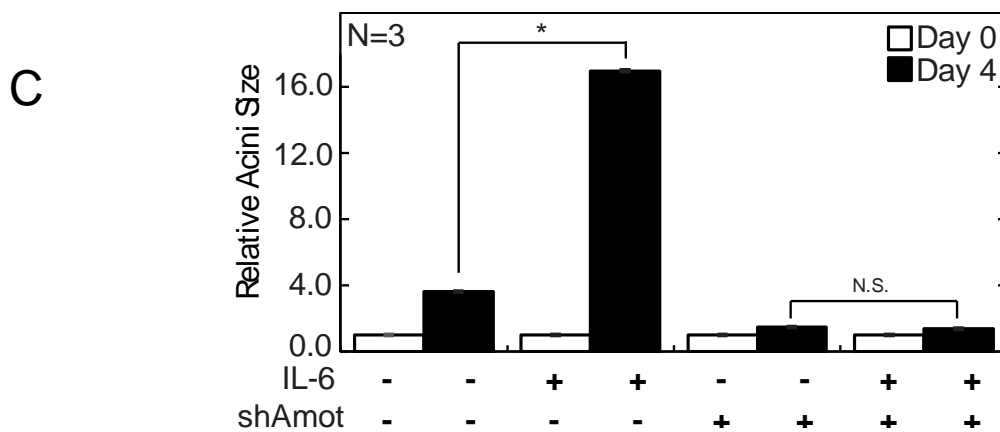
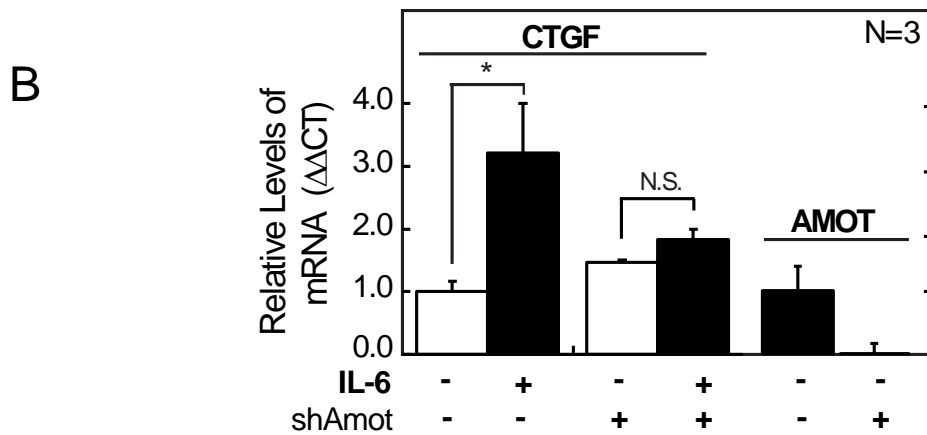
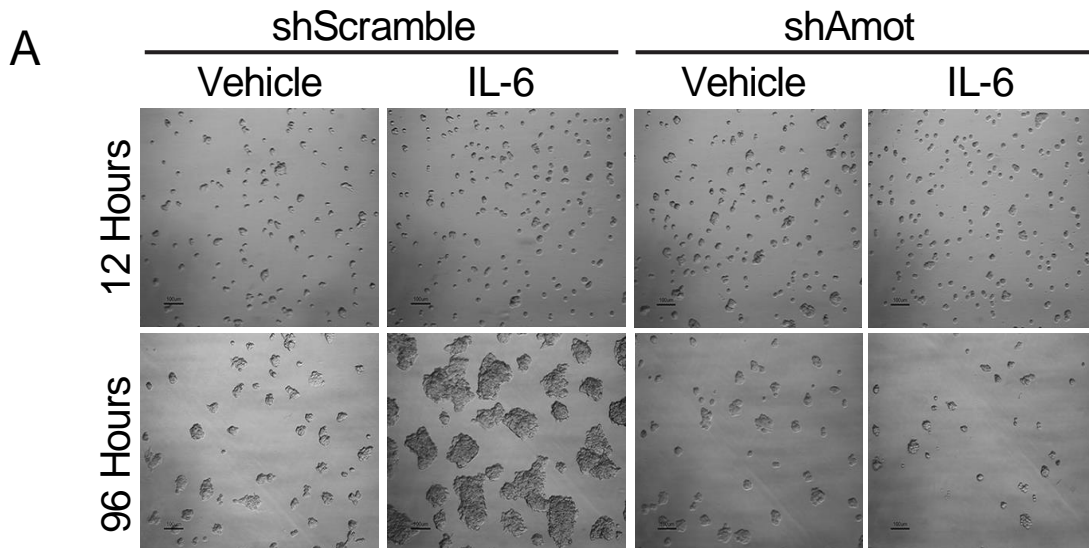


Figure 6-15. IL-6 requires Amot to induce CTGF transcription and growth in poorly differentiated Her2+ breast cancer cells. A-B. SKBR3 cells infected with Amot shRNA were seeded into a laminin-rich 3D Matrigel© environment, treated with 0.1 ng/mL IL-6 or vehicle control for a duration of 4 days, and measured for CTGF mRNA levels. N=3, S.D., Student's t-test, *p < 0.01. Cells were confirmed for silencing via immunoblot. C. Cells from A were imaged and the cross sectional area of the acini was quantified with ImageJ software. N=3. S.E.. *p < 0.01. **p < 0.001.

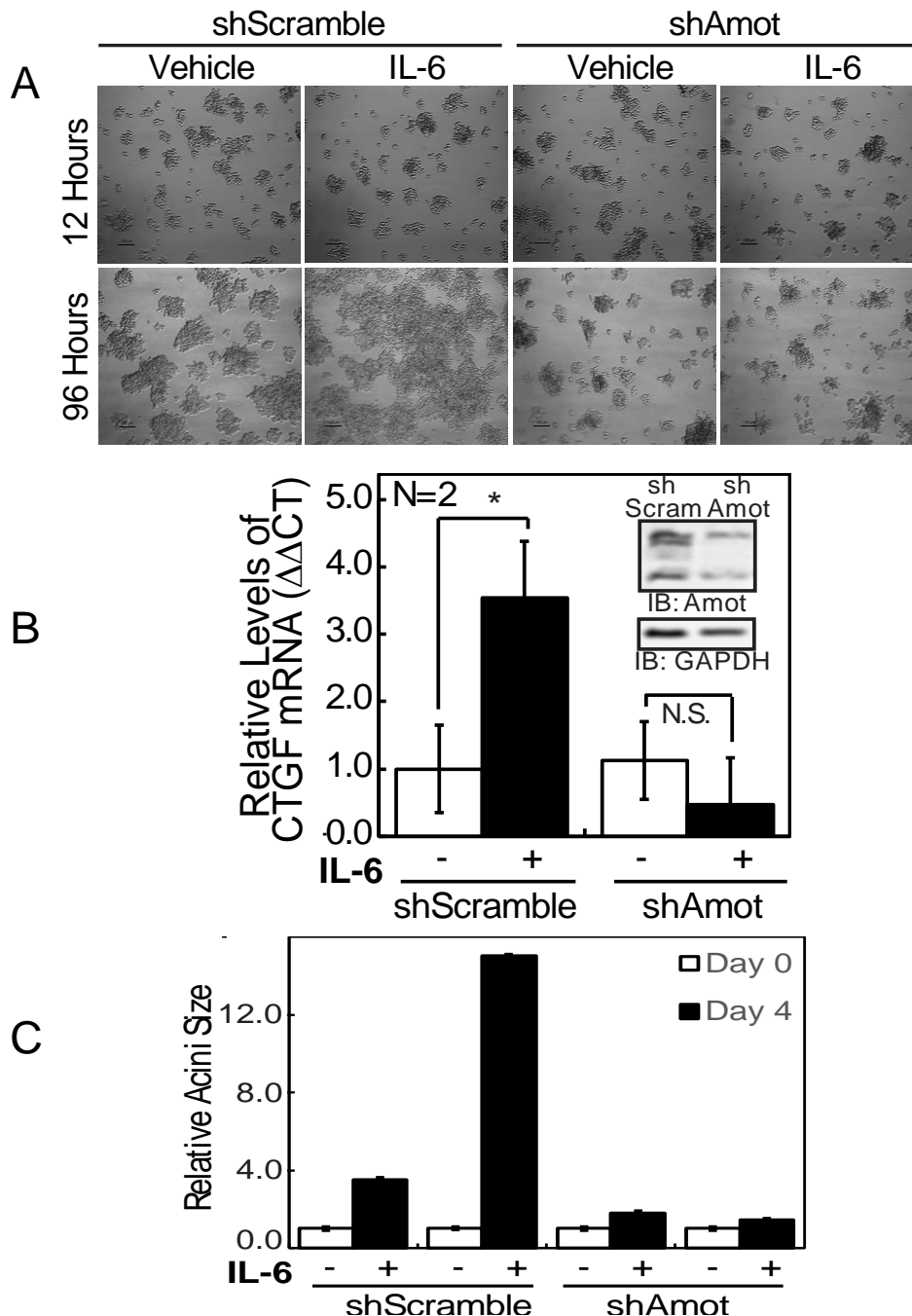


Figure 6-16. IL-6 requires Amot to induce CTGF transcription and growth in moderately differentiated triple negative breast cancer cells. A-B. MDA-MB-468 cells infected with Amot shRNA were seeded into a lamini-rich 3D Matrigel environment, treated with 0.1 ng/mL IL-6 or vehicle control for a duration of 4 days, and measured for CTGF mRNA levels. N=3, S.D., Student's TTest, *p< 0.01. Cells were confirmed for silencing via immunoblot (B). C. Cells from A were imaged and the cross sectional area of the acini was quantified with ImageJ software. N=3, S.E., *p<0.01, **p<0.001.

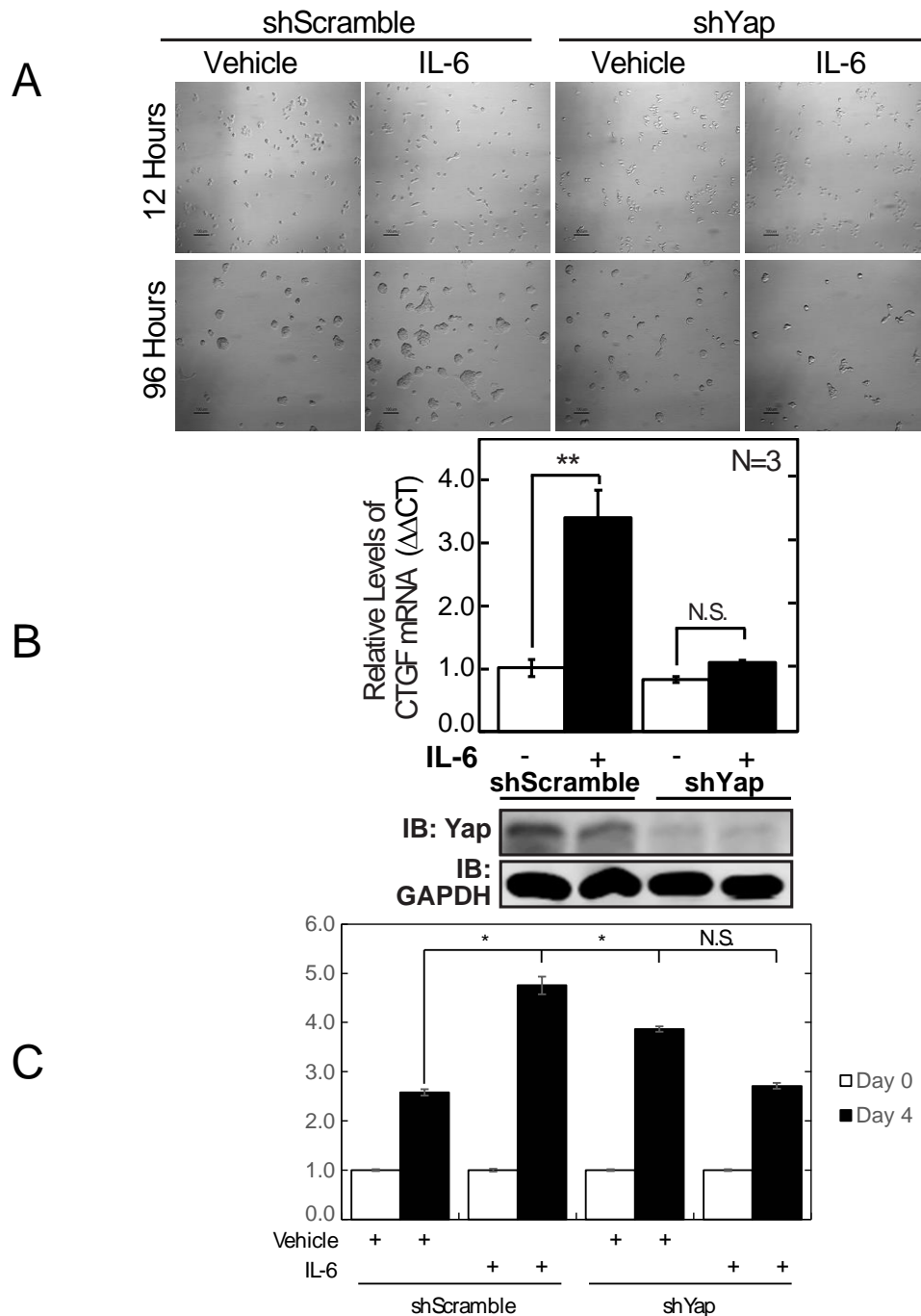


Figure 6-17. IL-6 requires YAP1 to induce CTGF transcription and growth in moderately differentiated ER + breast cancer cells. A-B. MCF7 cells infected with YAP11 shRNA were seeded into a laminin-rich 3D Matrigel environment, treated with 0.1 ng/mL IL-6 or vehicle control for a duration of 4 days, and measured for CTGF mRNA levels. N=3, S.D., Student's t-test, *p < 0.01. Cells were confirmed for silencing via immunoblot (B). C. Cells from A were imaged and the cross sectional area of the acini was quantified with ImageJ software. N=3, S.E., *p < 0.01, **p < 0.001. *Note: this experiment was attempted in MDA-MB-468 cells and SKBR3s and yielded dramatic and rapid cell death.

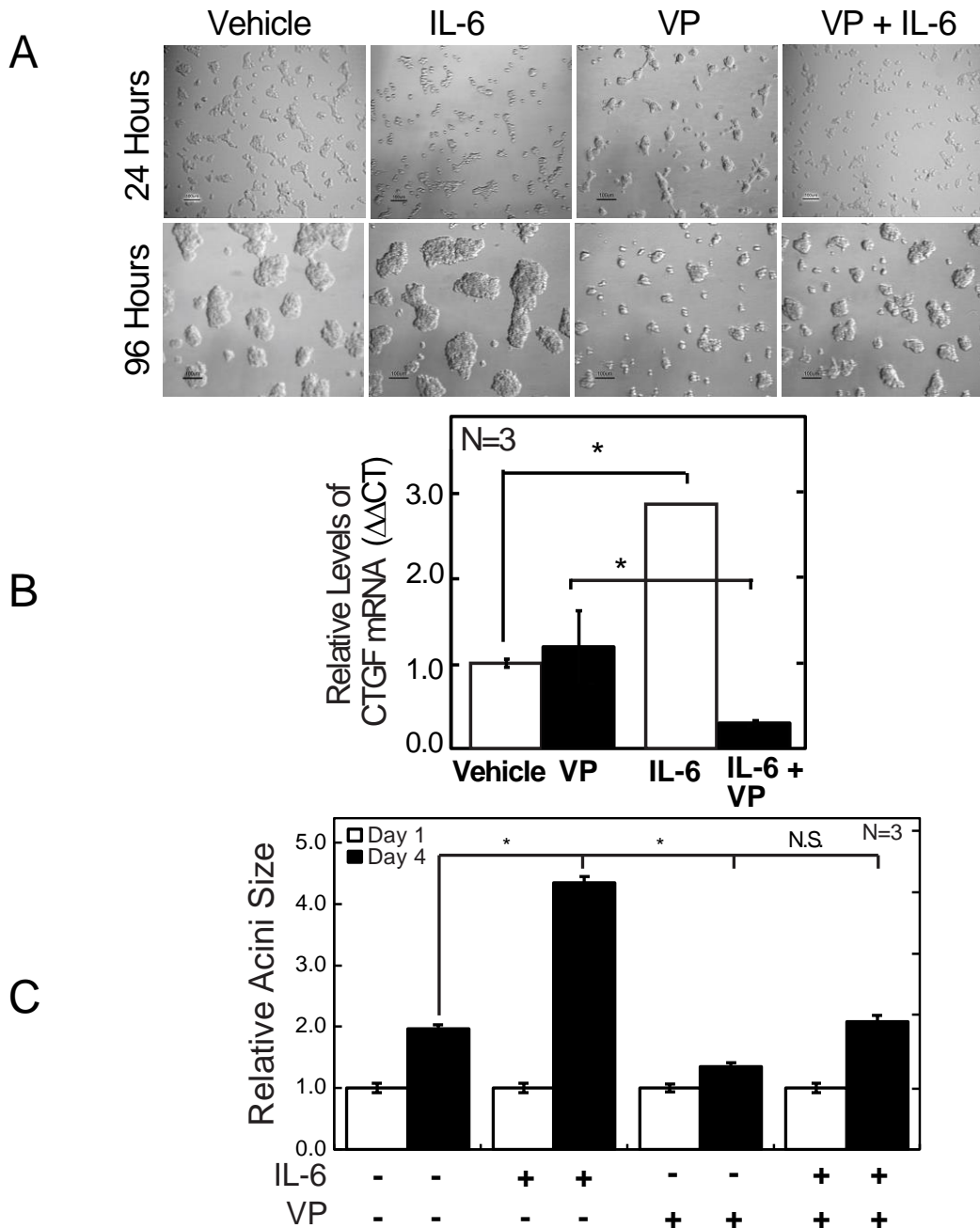


Figure 6-18. IL-6 requires the coactivation of TEAD by YAP1 to induce CTGF transcription and growth in moderately differentiated ER + breast cancer cells. A-B. MCF7 cells were seeded into a laminin-rich 3D Matrigel® environment, treated with treated with 0.1 ng/mL IL-6, 1 μ M Verteporfin (VP), IL-6 and VP, or vehicle control for a duration of 4 days, and measured for CTGF mRNA levels. N=3, S.D., Student's t-test, * $p < 0.01$. C. Cells from A were imaged and the cross sectional area of the acini was quantified with ImageJ software. N=3, S.E., * $p < 0.01$, ** $p < 0.001$. *Note: this experiment was attempted in MDA-MB-468 cells and SKBR3s and yielded dramatic and rapid cell death.

6-17A-C). The direct induction of CTGF transcription by the co-activation of the TEAD transcription factor by YAP1 to stimulate the CTGF promoter is widely published [103-106,117,119,139,198-201]. ENCODE shows that TEAD binding of the CTGF promoter produced a strong signal with a cluster score of 1000 [96].

In addition to the validated binding of Sp1 and TEAD4 to the CTGF promoter, ENCODE also shows that STAT3 binds the CTGF promoter with cluster score of 137 [96]. The observation of the correlated binding of TEAD, Sp1, and STAT3 on the CTGF promoter, in combination with the convergence of YAP1-TEAD, STAT3, and Sp1 signaling in the promotion of cell growth, led us to wonder if other genes were regulated by the simultaneous binding of these three transcription factors. To determine the identities of these genes, we first cross referenced YAP1 occupied gene promoters with TEAD occupied gene promoters found in chromatin immunoprecipitation assays by Zhao *et al.* 2008 in order to select for the YAP1-TEAD complex activated genes [202]. Subsequently we configured the transcription factor binding site (TFBS) track in ENCODE to isolate the binding of TEAD4, Sp1, and STAT3. We then searched the genes of all 1,968 YAP1-TEAD occupied promoters. We recorded whether Sp1 and/or STAT3 binding occurred within 3 kilobases upstream of the TSS of each gene. A total of 451 genes were not found in the UCSC genome browser, so these genes were thrown out. Our analysis resulted in the creation of four distinct gene lists: 1) 531 gene promoters bound by the YAP1-TEAD complex, 2) 471 gene promoters bound by both Sp1 and YAP1-TEAD, 3) 117 gene promoters bound by STAT3 YAP1-TEAD, and 4) 398 gene promoters bound by STAT3, Sp1, and

YAP1-TEAD. We then set out to compare the oncogenic impact of the four different gene lists. For this task we employed the Database for Annotation, Visualization and Integrated Discovery (DAVID) functional annotation software, a database that clusters genes based on various parameters including cellular function, correlation to diseases, protein domains, subcellular localizations, and many others. The OFFICIAL_GENE_SYMBOL of the genes in all four gene lists were uploaded separately and analyzed for KEGG Pathway(s) and gene-disease associations. Interestingly, the DAVID analysis found that only the genes simultaneously bound by YAP1-TEAD, Sp1, and STAT3 correlated with cancer-associated diseases (Fig 6-19). No other parameters available in DAVID showed notable differences between the four gene lists [203]. This novel finding further establishes the importance of the converged signaling between HIPPO pathway dysregulation and the pro-inflammatory secretion of IL-6 to drive nuclear STAT3 and Sp1.

6.4 Discussion

As discussed in Chapter 4, high Amot expression in breast cancer has been shown to correlate with a poor prognosis and a marked reduction in patient survival [132]. A vast amount of work completed by the Wells group and others has demonstrated the significance of the Angiomotins with regard to directing intracellular YAP1 localization in a context-dependent manner. It is regarded that this correlation of Amot to poor prognosis is due to its function as a prominent driver of YAP1 nuclear translocation to foster a pro-growth and pro-survival phenotype through the activation of YAP1 target genes such as *CTGF*. The link

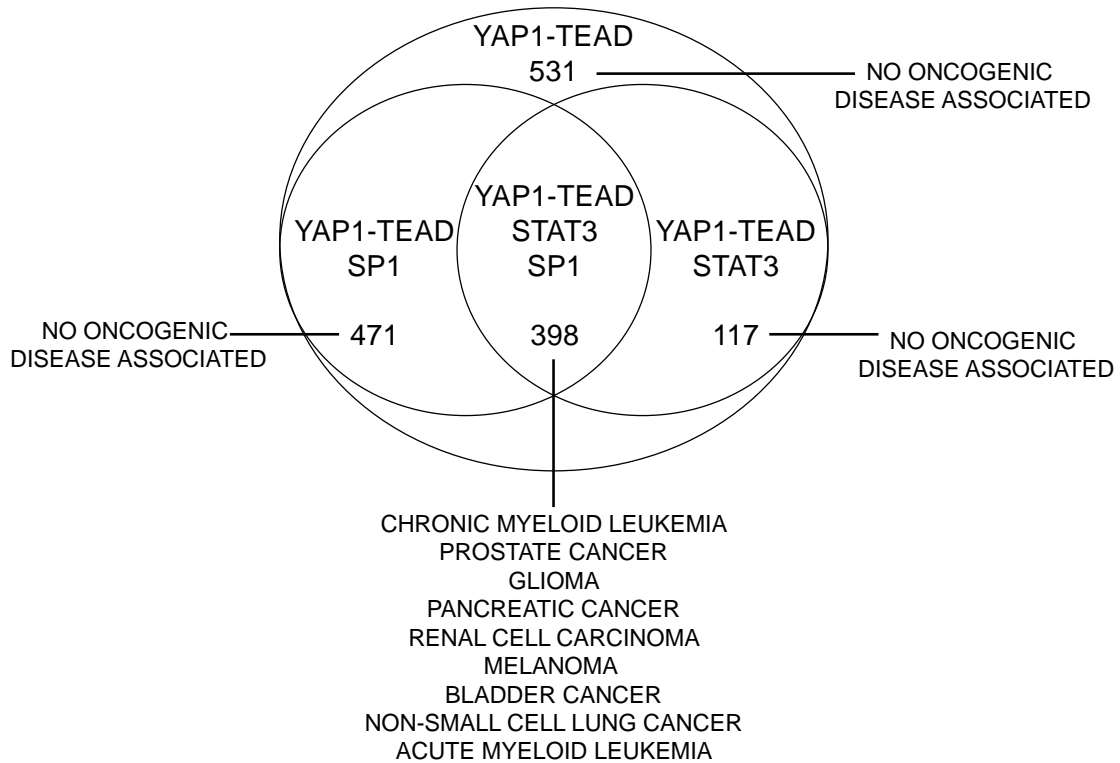


Figure 6-19. Genes that are simultaneously bound by YAP1-TEAD, Sp1, and STAT3 correlate with cancer associated genes, in contrast to genes that are bound by only YAP1-TEAD, by Sp1 and YAP1-TEAD, or by STAT3 and YAP1-TEAD. Genes of YAP1-TEAD occupied promoters were observed for Sp1 and/or STAT3 binding using the Encyclopedia of DNA Elements (ENCODE) in the UCSC genome browser. The resulting gene lists were analyzed using the Database for Annotation, Visualization and Integrated Discovery (DAVID) software for the clustering against the parameter of cancer-associated diseases.

between IL-6 and/or STAT3 signaling to YAP1 pro-growth signaling only first appeared in the literature in 2014; four studies have demonstrated this connection in breast, liver, intestine, and adipocytes [121,177,182,204]. An impressive 91 studies dating back to 2001 have shown a connection between IL-6 and CTGF. However, very little has been done to elucidate the mechanism by which IL-6 activates YAP1 and/or elevates CTGF transcripts. In preliminary experiments, there was indeed a time-dependent influence of IL-6 on Amot protein levels (Fig 6-5C) but not on YAP1 protein levels; This proposed a potential for Amot-dependent YAP1 nuclear trans-localization to be critically important in the signaling between IL-6 and CTGF.

The fact that the elevation of Amot promoter activity in response to IL-6 is returned to basal levels by STAT3 inhibition (Fig 6-7), yet the reduction of basal STAT3 levels by shRNA yielded Amot protein levels that were markedly reduced in comparison to control highlight the potential for enhanced protein degradation in addition to reduced transcriptional activation of Amot upon reduced basal STAT3 levels (Fig 6-6A). All of these data, despite the fact that no STAT3 binding occurs in the Amot promoter, indicate that IL-6/STAT3 activate the Amot promoter through another IL-6 responsive transcription factor.

Both STAT3 and Sp1 have demonstrated abilities to independently activate over 3000 promoters in the cell [87]. Additionally, it is widely known that activated STAT3 can function to recruit Sp1 to the nucleus to enhance Sp1 DNA binding activity and activation of growth and survival genes [93]. The literature supports the ability of Sp1 to directly bind and strongly activate CTGF,

independent of Amot [74]. However, our data show that this signaling, with regard to CTGF promoter activity, is mitigated in conditions where Amot or YAP1 are silenced, or YAP1 is inhibited (Fig 6-15-6-18). This demonstrates that the activation of the CTGF promoter by IL-6 exploits the activation of YAP1 by Amot. Sp1 binding of the Amot promoter is therefore required in order for IL-6 to induce cell growth (Fig 6-18).

Altogether, this work has provided novel insights into the location of the start of transcription of the *AMOT* gene, a primary mechanism of transcriptional control of the Amot isoforms, and the necessity of the Amot isoforms to direct growth and signaling in response to IL-6.

CHAPTER 7: DISCUSSION

For this dissertation, we sought to address whether the dysregulation of HIPPO signaling, through the increased expression of the Angiotensin isoforms, plays a role in DCIS to IDC transitions in mammary tissue. To answer this broad question, we focused our efforts in addressing a number of specific points expanded upon below.

7.1 Total Amot expression levels are greater and its subcellular localization is altered in more aggressive forms of breast cancers.

The first point we addressed was to associate the histologic measures of Amot protein expression and subcellular localizations with reports of enhanced levels of Amot transcripts in breast tumors. Our data recapitulated the following results from Jiang *et al.* 2006 and Lv *et al.* 2015: We found that Amot protein expression is indeed elevated in breast cancers (Fig 4-2A), that it exhibits a 3-fold increase in pre-metastatic tumor samples than in those that did not metastasize (Fig 4-7), and that Amot levels show no direct correlation to estrogen or progesterone receptor statuses (Fig 4-3, 4-4) [132, 133].

Additionally, our work disagreed with Jiang *et al.* 2006 which reported that Amot mRNA levels are increased in tumors from patients diagnosed with the more aggressive node positive breast cancer disease, yet showed no marked increase in Amot mRNA in pre-recurrent tumor samples [132]. Our results, however, revealed no significant difference between samples from node positive versus node negative diagnoses (Fig 4-6), but surprisingly yielded a more than 3-

fold increase in Amot protein expression in pre-recurrent tumor samples over non-recurrent samples (Fig 4-8). The combination of the following findings strongly indicate the significance of Amot expression in highly aggressive forms of breast cancer: the rise of Amot mRNA in the more aggressive node-positive tumors [132], the proliferating cancer cells within the tumor exhibited the highest degree of Amot staining [133], elevated Amot mRNA correlated with a high hazard ratio [Bringman unpublished], and the correlation of increased Amot expression in pre-metastatic (Fig 4-7) [132] and pre-recurrent breast tumor samples (Fig 4-8).

Furthermore, our study extended beyond the current literature and provided insights into the incidence and roles of elevated Amot expression in those tumor samples undergoing the transition from DCIS to IDC. We found that Amot protein expression is over 4-fold higher in transitioning tumors, characterized as IDC with a predominant presence of DCIS, than in those tumors where IDC seemingly developed *de novo* (Fig 4-9). Our analysis of the staining pattern of Amot in the majority of these samples exhibited Amot occurring in juxta nuclear punctae (Fig 4-10). The staining of Amot in this pattern has strongly correlated with the high association of Amot 80 with proteins to drive a pro-migratory phenotype [166]. Additional work from the Wells lab has demonstrated that YAP1 co-localizes with the Amots exhibiting this same punctal pattern in fixed cell imaging of cells co-expressing Amot 130 and Amot 80 (data not shown). It is also important to note that as Amot 80 does not possess the motif required to bind YAP1 (Fig 1-10), Amot 130 is indeed necessary to this co-

localization of YAP1 to these juxta nuclear punctae, and therefore is evidence to support that this is a complex formation resulting from the dimerization of Amot 130 and Amot 80. This juxta nuclear Amot staining was also observed in cells within the tissue that appear to be in the process of invading the stroma.

In summation, this particular work adds significant information to the field of HIPPO signaling with respect to Amot expression in human breast cancer tissues. Not only are we the first to distinguish Amot as a potential marker of DCIS to IDC transitional events, but we are also the first to show explicit, highly specific Amot fluorescent staining in human breast tumor tissue samples. This accomplishment has allowed us to associate the levels of Amot with cells at different phases of differentiation by relating Amot localization to nuclear, diffuse, and junctional staining.

We would like to complete follow up studies that compare additional invasive breast tumor samples with and without predominant DCIS lesions using immunofluorescent imaging. The ability to perform immunoblot analyses on these tissues would also provide a quantifiable measure of the protein expression levels of the individual Amot isoforms. Furthermore, the imaging of additional samples could also aid in establishing stronger correlations between the various Amot staining patterns and clinical features of breast tumors, such as HER2 status, and patient follow up data, such as survivorship. Comprehensively, this work could result in the Amot isoforms becoming a prognostic marker of DCIS lesions at risk for transitioning to IDC and potentially prevent unnecessary surgeries for those DCIS patients that exhibit low Amot expression.

7.2 The mRNA expression of the Amot isoforms is controlled by a single promoter and result from alternative pre-mRNA splicing.

The potential role of Amot proteins in DCIS to IDC transitions motivated us to question how their expression is controlled. The literature is currently lacking of any thorough investigation into this, but rather focuses on the altered activity of Amot 130 due to mechanisms of post-translational modifications [117,128, 137,138]. Preliminary data, including TCGA analysis of over 700 breast tumor samples, supports the significance of Amot mRNA expression in aggressive breast cancers (Bringman unpublished). Moving forward, we concentrated heavily on molecular biology techniques in order to address our second point of this thesis work, which was to define the *AMOT* gene, its regulatory region(s), the promoter element(s) that control its transcription, and the manner in which the unique isoforms are expressed. Our work is the first to identify a single transcription start site controlling the mRNA expression of both Amot 130 and Amot 80 isoforms. This new information provided us with the following insights: 1. Both the Amot 130 and 80 isoforms are regulated by a single promoter upstream of GChr37: 112840790 2. These isoforms are results of alternative pre-mRNA splicing (Fig 5-2-5-5).

Regarding insight 1, the definition of a sole TSS not only highlights the specific set of transcription factors that are likely responsible for regulating Amot isoform transcription, it also dispels the likelihood that the active chromatin region upstream of exon 2 could be an additional regulatory element for the transcription of both or either isoform. With no H3K4me3 marks, this region of loosened

histones more likely serves as intron/exon boundary [206] (Fig 5-1). This result served as the basis for the design and study of the Amot promoter reporter construct; a reagent that possesses interminable potential for studying the regulation of Amot transcription. Furthermore, we verified the region of the Amot promoter that is key to driving Amot transcription, therefore narrowing down a subset of transcription factors that are significant to this system (Fig 5-8). As the Amot isoforms serve as the predominant director of YAP and TAZ subcellular localizations, the study of the transcription factors that modulate their expression is central to the understanding of HIPPO signaling.

With respect to insight 2, we identified the data that supports a notion that the field has been assuming for over a decade: the Amot isoforms are indeed splice variants of each other. Ascertaining the 5' leader exons unique to each isoform has provided our lab with the first ever primer sets to distinguish these gene products (Fig 5-7). These reagents hold the power both to aid in the identification of potential factors that drive the alternative splicing of the Amot isoforms as well as serve as the detection method to establish these isoforms as possible biomarkers for DCIS to IDC transitions.

To conclude, these data not only provide the field with a greater understanding of the *AMOT* gene architecture, but also yielded a set of biological tools for the detection and study of the transcriptional regulation of a key set of proteins that govern the activity of the YAP and TAZ oncogenes. These tools will allow for the future studies investigating which transcription factors are required

to modulate Amot transcription as well as which factors drive Amot 80 verses Amot 130 favored mRNA splicing.

7.3 The enhanced expression of pro-tumorigenic genes by IL-6 is Amot-dependent and requires coordinated Sp1, STAT3, and YAP1-TEAD promoter occupancy.

The concentrations of pro-inflammatory cytokines present in the mammary stroma and sera are greatly increased in patients that experienced a transition of DCIS to IDC [10,35,38]. To accompany our finding that Amot levels are higher in IDC tissues with predominant presence of DCIS lesions, we sought to define the impact of inflammatory cytokine induced signaling on Amot expression. To address this, we tested Amot promoter activity against three key cytokines in the promotion of breast cancer: IFN γ , TNF α , and IL-6. Treatment with IL-6 produced the greatest impact on Amot promoter activity (Fig 6-1A, 6-7, 6-8B); this is also in agreement with our mRNA and immunoblot analysis showing a dramatic induction of both Amot 130 and Amot 80 transcript and protein expression (Fig 6-2, 6-5, 6-6).

Regarding the question of how inflammation innervates dysregulated HIPPO signaling, we sought to establish the importance of Amot as an effector of inflammatory induced cell dedifferentiation and proliferation. Our data revealed that the stimulation of Amot depleted cells with IL-6 not only displayed a mitigated tumor phenotype, but also a markedly reduced cell growth and CTGF

transcriptional activation (Fig 6-14-6-16). We also observed a dramatic loss of both Amot and protein levels following the silencing of STAT3 (Fig 6-6), an event so widely demonstrated to radically impede tumor growth that it has fostered the generation of a plethora of STAT3 inhibitor drugs. The depletion of YAP1 protein levels was also observed in response to STAT3 silencing (Fig 6-6C), warranting our further investigation into the requirement of YAP protein for the IL-6 induced growth phenotype and CTGF transcriptional activation. This led to our novel discoveries that both YAP1 protein expression and its co-activation of TEAD are necessary and sufficient events in tumorigenic progression by IL-6 (Fig 6-17, 6-18). Additionally, because the CTGF promoter is directly bound and activated by the YAP-TEAD complex [110-128; 204], the loss of tumorigenic growth exhibited in Verteporfin-treated cells, despite stimulation by IL-6, only further raises the significance of CTGF to the efficiency of IL-6 to promote tumorigenesis in these cells.

Finally, our pursuit of the identification of the key factors in inflammatory based signaling that induce Amot transcription revealed that Sp1, a well-studied cooperative effector of IL-6 signaling [87,93,94] is not only required for enhancement of Amot expression by IL-6, but also the IL-6 induced activation of CTGF transcription. The impact of Sp1 on the activation of CTGF has been well-established in response to TGF β signaling [98], but never examined in response to stimulation by IL-6. Sp1 has, however, been implicated in the coordinate gene transcription with its sometimes binding partner PSTAT3, an event commonly stimulated by IL-6 signaling [93-94]. The fact that the Amot promoter does exhibit

Sp1 but not STAT3 binding (Fig 6-8A), and its activation in response to IL-6 is both STAT3 and Sp1 dependent (Fig 6-7, 6-8B, 6-10), raises the likelihood that the *AMOT* gene, like many others studied in the literature, is regulated by this concordant mechanism of IL-6 induced Sp1 and STAT3 cooperative promoter co-occupancy [93, 94]. Interestingly, ENCODE analysis revealed that the CTGF promoter is in fact bound by STAT3, Sp1, and TEAD4. Since CTGF mRNA levels are so tightly coupled to dysregulated HIPPO signaling that the transcript in fact serves as a chief control readout for nuclear YAP1 activity [110-128; 204], we decided to explore the frequency that STAT3 and Sp1 co-transcription factors co-occupy other gene promoters with validated YAP1-TEAD binding [204]. This effort resulted in the first comprehensive bioinformatic study of Sp1, STAT3, and YAP1-TEAD promoter co-occupancy. Surprisingly, ENCODE and DAVID analysis revealed that all of the pro-tumorigenic genes that are co-activated by YAP1-TEAD also exhibited binding by both STAT3 and Sp1. Conversely, the DAVID analysis revealed that no cancer-associated genes occurred within the 3 lists of gene promoter occupancy of 1) YAP1-TEAD alone, 2) Sp1 and YAP1-TEAD co-occupancy, and 3) STAT3 and YAP1-TEAD co-occupancy. Because the Amot isoforms serve as the predominant directors of YAP1-TEAD activity [117], and we have confirmed that the IL-6 induced pro-growth phenotype in breast cancer is both dependent upon the presence of Amot and the nuclear complex formation of YAP1-TEAD (Fig 6-14-6-18), this data only further supports the significance of this discovery that the innervation of pro-inflammatory IL-6 with

the down-regulation of HIPPO signaling to tumorigenic growth in breast cancer cells.

This collection of data is the first to define a mechanism by which pro-inflammatory IL-6 signaling in the microenvironment of breast cancer cells can drive the loss of intracellular polarity regulation by HIPPO signaling via enhanced Amot expression (Fig 6-5, 6-6). This, in turn, drives the YAP-nuclear translocation which fosters the pro-tumorigenic growth akin to the IL-6 signaling effect in the pro-inflammatory tumor microenvironment in a variety of cancers, including those arising from the mammary gland (Fig 6-3A, 6-17, 6-18) [81,82, 84-87]. As the literature has observed that levels of IL-6 are increased in transitioning IDC tumors [10, 35, 38], these findings support the likelihood that IL-6 and Amot levels are coordinately increased in IDC tumors with predominant DCIS lesions over de novo IDC.

Although the impacts of IL-6 signaling on TAZ levels and activity was only briefly touched upon, the fact that we saw the silencing and inactivation of YAP1 alone was sufficient to impede the IL-6 induced growth phenotype and CTGF transcription demonstrated either that: 1. TAZ alone is incapable of overcoming the loss of YAP activity, or 2. That the effect we see on YAP1 is actually mimetic of the effects on TAZ. Regardless of the answer, this sufficiently dispels the urge to study this particular interconnected signaling mechanism with respect to HIPPO transcriptional coactivator TAZ [107, 108]. However, the results from this work do highlight the potential for additional studies that investigate whether the activity and stability of the Amot proteins is impacted in response to IL-6. Our

preliminary analysis of whether treatment with IL-6 increases the stability of the Amot isoforms was inconclusive, but it certainly continues to be worthy of pursuing, particularly in the case of Amot 130 and its ability to be phosphorylated and targeted for degradation [137, 138]. In addition, our data showed that the transcriptional activation of the Amot isoforms through this mechanism did not exhibit alternative splicing (Fig 6-4), but our identification of the active region in the Amot promoter identifies a variety of transcription factors that could be impacted by signaling from other cytokines commonly present in a pro-inflammatory tumor microenvironment (Fig 6-8). Moreover, the opportunity to correlate Amot expression and staining patterns within tumor tissue samples exhibiting either greater phosphorylated STAT3 levels or an increased presence of activated lymphocytes and/or macrophages would provide further validation that this signaling mechanism is translationally relevant (Fig 1-2).

Additionally, this work raises a variety of questions regarding the role of the Amot isoforms in response to wound healing as well as in the mechanism of de-differentiation during an EMT event. While a number of studies discuss the possible connection of the Amots to these cellular processes, the research investigating these connections is still greatly deficient. The work we have done to establish the convergence of pro-inflammatory IL-6 signaling, a pathway heavily implicated in both the facilitation of wound healing and the driving of EMT events [70, 72, 75-77], with the dysregulation of HIPPO polarity signaling has created a solid foundation for its applications in wound healing and EMT studies.

APPENDIX – NUCLEOTIDE SEQUENCES

5' RACE PRIMERS

5' Linker Primer: 5'-

GCTGATGGCGATGAATGAACACTGCGTTTGCTGGCTTTGATGAAA-3'

3' Amot Exon 2 Primer: 5'-

AGCTAGCTGTTAATTAATCAGGCTTCGGTCCCGGGCC-3'

3' Amot Exon 4 Primer: 5'-

qRT-PCR PRIMERS

CTGF Forward: 5'-AGGAGTGGGTGTGTGACGA-3'

CTGF Reverse: 5'-CCAGGCAGTTGGCTCTAATC-3'

AMOT 130 Forward: 5'-AGAGGCACCACCAGCAATAGAGAAGC

AMOT 130 Reverse: 5'-GGGCGTCCCTCAGTCCTCATGC

AMOT 80 Forward: 5'-TAGCCGCTCACCGCAAGAAGC

AMOT 80 Reverse: 5'-TCTGCTCGCTCAAGTGGCTTGC

TOTAL AMOT Forward: 5'-GCATTCTCCTGGGTGGAGAC

TOTAL AMOT Reverse: 5'-GATTCCGTCCCACGTTCAAGT

STAT3 Forward: 5'-ACCTGCAGCAATACCATTGAC

STAT3 Reverse: 5'-AAGGTGAGGGACTCAAAGTGC

GAPDH Forward: 5'-CCAGGCAGTTGGCTCTAATC

GAPDH Reverse: 5'-CCAGGCAGTTGGCTCTAATC

18S rRNA Forward: 5'-CCGATAACGAACGAGACTCTGG

18S rRNA Reverse: 5'-TAGGGTAGGCACACGCTGAGCC

Pax7 Forward: 5'-AGCATCCTTAGCAACCCGAG

Pax7 Reverse: 5'-CTCCTGGCTTGGATGGAGTCG

REFERENCES

- 1 Khokha, R. & Werb, Z. Mammary Gland Reprogramming: Metalloproteinases Couple Form with Function. *Cold Spring Harbor Perspectives in Biology* **3**, doi:10.1101/cshperspect.a004333 (2011).
- 2 Kerlikowske, K. Epidemiology of ductal carcinoma *in situ*. *J Natl Cancer Inst Monogr* **2010**, 139-141, doi:10.1093/jncimonographs/lgq027 (2010).
- 3 Hussein, M. R. & Hassan, H. I. Analysis of the mononuclear inflammatory cell infiltrate in the normal breast, benign proliferative breast disease, *in situ* and infiltrating ductal breast carcinomas: preliminary observations. *J Clin Pathol* **59**, 972-977, doi:10.1136/jcp.2005.031252 (2006).
- 4 Polyak, K. Molecular markers for the diagnosis and management of ductal carcinoma *in situ*. *Journal of the National Cancer Institute. Monographs*. **2010**, 210-213, doi:10.1093/jncimonographs/lgq019 (2010).
- 5 Page, D. L. & Johnson, J. E. Controversies in the local management of invasive and non-invasive breast cancer. *Cancer Lett* **90**, 91-96 (1995).
- 6 Bleicher, R. J. Ductal carcinoma *in situ*. *Surg Clin North Am* **93**, 393-410, doi:10.1016/j.suc.2012.12.001 (2013).
- 7 Cowell, C. F., Weigelt, B., Sakr, R. A., Ng, C. K., Hicks, J., King, T. A. & Reis-Filho, J. S. Progression from ductal carcinoma *in situ* to invasive breast cancer: revisited. *Mol Oncol* **7**, 859-869, doi:10.1016/j.molonc.2013.07.005 (2013).
- 8 Society, A. C. Cancer Facts and Figures 2015. (2015).
- 9 McVeigh, T. P., Hughes, L. M., Miller, N., Sheehan, M., Keane, M., Sweeney, K. J. & Kerin, M. J. The impact of Oncotype DX testing on breast cancer management and chemotherapy prescribing patterns in a tertiary referral centre. *Eur J Cancer* **50**, 2763-2770, doi:10.1016/j.ejca.2014.08.002 (2014).
- 10 Beumer, I., Witteveen, A., Delahaye, L., Wehkamp, D., Snel, M., Dreezen, C., Zheng, J., Floore, A., Brink, G., Chan, B., Linn, S., Bernards, R., van 't Veer, L. & Glas, A. Equivalence of MammaPrint array types in clinical trials and diagnostics. *Breast Cancer Res Treat* **156**, 279-287, doi:10.1007/s10549-016-3764-5 (2016).
- 11 Sternlicht, M. D., Kedeshian, P., Shao, Z. M., Safarians, S. & Barsky, S. H. The human myoepithelial cell is a natural tumor suppressor. *Clin Cancer Res* **3**, 1949-1958 (1997).
- 12 Ranahan, W. P., Han, Z., Smith-Kinnaman, W., Nabinger, S. C., Heller, B., Herbert, B. S., Chan, R. & Wells, C. D. The adaptor protein AMOT promotes the proliferation of mammary epithelial cells via the prolonged activation of the extracellular signal-regulated kinases. *Cancer Research* **71**, 2203-2211, doi:10.1158/0008-5472.can-10-1995 (2011).
- 13 Hassiotou, F. & Geddes, D. Anatomy of the human mammary gland: Current status of knowledge. *Clinical Anatomy* **26**, 29-48, doi:10.1002/ca.22165 (2013).
- 14 Polyak, K. Breast cancer: origins and evolution. *Journal of Clinical Investigation* **117**, 3155-3163, doi:10.1172/jci33295 (2007).

- 15 Bombonati, A. & Sgroi, D. C. The molecular pathology of breast cancer progression. *Journal of Pathology* **223**, 307-317, doi:10.1002/path.2808 (2011).
- 16 Khokha, R. & Werb, Z. Mammary gland reprogramming: metalloproteinases couple form with function. *Cold Spring Harb Perspect Biol* **3**, doi:10.1101/cshperspect.a004333 (2011).
- 17 Bissell, M. J., Radisky, D. C., Rizki, A., Weaver, V. M. & Petersen, O. W. The organizing principle: microenvironmental influences in the normal and malignant breast. *Differentiation* **70**, 537-546, doi:10.1046/j.1432-0436.2002.700907.x (2002).
- 18 Xu, R., Boudreau, A. & Bissell, M. J. Tissue architecture and function: dynamic reciprocity via extra- and intra-cellular matrices. *Cancer Metastasis Rev* **28**, 167-176, doi:10.1007/s10555-008-9178-z (2009).
- 19 Cai, J., Zhang, N., Zheng, Y., de Wilde, R. F., Maitra, A. & Pan, D. The Hippo signaling pathway restricts the oncogenic potential of an intestinal regeneration program. *Genes Dev* **24**, 2383-2388, doi:10.1101/gad.1978810 (2010).
- 20 Coopman, P. & Djiane, A. Adherens Junction and E-Cadherin complex regulation by epithelial polarity. *Cell Mol Life Sci*, doi:10.1007/s00018-016-2260-8 (2016).
- 21 Elbediwy, A., Vincent-Mistiaen, Z. I. & Thompson, B. J. YAP and TAZ in epithelial stem cells: A sensor for cell polarity, mechanical forces and tissue damage. *Bioessays*, doi:10.1002/bies.201600037 (2016).
- 22 Ioannou, M. S. & McPherson, P. S. Rab-mediated membrane trafficking and the control of epithelial cell polarity. *J Cell Biol* **213**, 301-303, doi:10.1083/jcb.201604076 (2016).
- 23 Aneta, G., Tomas, V., Daniel, R. & Jan, B. Cell polarity signaling in the plasticity of cancer cell invasiveness. *Oncotarget*, doi:10.18632/oncotarget.7214 (2016).
- 24 Pasti, G. & Labouesse, M. Epithelial junctions, cytoskeleton, and polarity. *WormBook*, 1-35, doi:10.1895/wormbook.1.56.2 (2014).
- 25 Rodriguez-Boulan, E. & Macara, I. G. Organization and execution of the epithelial polarity programme. *Nat Rev Mol Cell Biol* **15**, 225-242, doi:10.1038/nrm3775 (2014).
- 26 Halder, G. & Johnson, R. L. Hippo signaling: growth control and beyond. *Development* **138**, 9-22, doi:10.1242/dev.045500 (2011).
- 27 Bao, Y., Hata, Y., Ikeda, M. & Withanage, K. Mammalian Hippo pathway: from development to cancer and beyond. *J Biochem* **149**, 361-379, doi:10.1093/jb/mvr021 (2011).
- 28 Reddy, B. V. & Irvine, K. D. Regulation of Hippo signaling by EGFR-MAPK signaling through Ajuba family proteins. *Dev Cell* **24**, 459-471, doi:10.1016/j.devcel.2013.01.020 (2013).
- 29 Herranz, H., Hong, X. & Cohen, S. M. Mutual repression by bantam miRNA and Capicua links the EGFR/MAPK and Hippo pathways in growth control. *Curr Biol* **22**, 651-657, doi:10.1016/j.cub.2012.02.050 (2012).

- 30 Yang, C. C., Graves, H. K., Moya, I. M., Tao, C., Hamaratoglu, F., Gladden, A. B. & Halder, G. Differential regulation of the Hippo pathway by adherens junctions and apical-basal cell polarity modules. *Proc Natl Acad Sci U S A* **112**, 1785-1790, doi:10.1073/pnas.1420850112 (2015).
- 31 Guyer, R. A. & Macara, I. G. Loss of the polarity protein PAR3 activates STAT3 signaling via an atypical protein kinase C (aPKC)/NF-kappaB/interleukin-6 (IL-6) axis in mouse mammary cells. *J Biol Chem* **290**, 8457-8468, doi:10.1074/jbc.M114.621011 (2015).
- 32 Feigin, M. E. & Muthuswamy, S. K. Polarity proteins regulate mammalian cell-cell junctions and cancer pathogenesis. *Curr Opin Cell Biol* **21**, 694-700, doi:10.1016/j.ceb.2009.07.003 (2009).
- 33 Gangadhar, T. C. & Vonderheide, R. H. Mitigating the toxic effects of anticancer immunotherapy. *Nat Rev Clin Oncol* **11**, 91-99, doi:10.1038/nrclinonc.2013.245 (2014).
- 34 Schafer, M. & Werner, S. Cancer as an overhealing wound: an old hypothesis revisited. *Nat Rev Mol Cell Biol* **9**, 628-638, doi:10.1038/nrm2455 (2008).
- 35 Grivennikov, S. I., Greten, F. R. & Karin, M. Immunity, inflammation, and cancer. *Cell* **140**, 883-899, doi:10.1016/j.cell.2010.01.025 (2010).
- 36 Hanahan, D. & Weinberg, R. A. Hallmarks of cancer: the next generation. *Cell* **144**, 646-674, doi:10.1016/j.cell.2011.02.013 (2011).
- 37 Shalapour, S. & Karin, M. Immunity, inflammation, and cancer: an eternal fight between good and evil. *J Clin Invest* **125**, 3347-3355, doi:10.1172/jci80007 (2015).
- 38 Karin, M. NF-kappaB as a critical link between inflammation and cancer. *Cold Spring Harb Perspect Biol* **1**, a000141, doi:10.1101/cshperspect.a000141 (2009).
- 39 de Martel, C. & Franceschi, S. Infections and cancer: established associations and new hypotheses. *Crit Rev Oncol Hematol* **70**, 183-194, doi:10.1016/j.critrevonc.2008.07.021 (2009).
- 40 de Martel, C., Plummer, M., Parsonnet, J., van Doorn, L. J. & Franceschi, S. Helicobacter species in cancers of the gallbladder and extrahepatic biliary tract. *Br J Cancer* **100**, 194-199, doi:10.1038/sj.bjc.6604780 (2009).
- 41 Takahashi, H., Ogata, H., Nishigaki, R., Broide, D. H. & Karin, M. Tobacco smoke promotes lung tumorigenesis by triggering IKKbeta- and JNK1-dependent inflammation. *Cancer Cell* **17**, 89-97, doi:10.1016/j.ccr.2009.12.008 (2010).
- 42 Ammirante, M., Luo, J. L., Grivennikov, S., Nedospasov, S. & Karin, M. B-cell-derived lymphotoxin promotes castration-resistant prostate cancer. *Nature* **464**, 302-305, doi:10.1038/nature08782 (2010).
- 43 Rodier, F., Coppe, J. P., Patil, C. K., Hoeijmakers, W. A., Munoz, D. P., Raza, S. R., Freund, A., Campeau, E., Davalos, A. R. & Campisi, J. Persistent DNA damage signalling triggers senescence-associated inflammatory cytokine secretion. *Nat Cell Biol* **11**, 973-979, doi:10.1038/ncb1909 (2009).

- 44 Zheng, L., Dai, H., Zhou, M., Li, M., Singh, P., Qiu, J., Tsark, W., Huang, Q., Kernstine, K., Zhang, X., Lin, D. & Shen, B. Fen1 mutations result in autoimmunity, chronic inflammation and cancers. *Nat Med* **13**, 812-819, doi:10.1038/nm1599 (2007).
- 45 Karin, M. & Clevers, H. Reparative inflammation takes charge of tissue regeneration. *Nature* **529**, 307-315, doi:10.1038/nature17039 (2016).
- 46 Ud-Din, S. & Bayat, A. Non-invasive objective devices for monitoring the inflammatory, proliferative and remodelling phases of cutaneous wound healing and skin scarring. *Exp Dermatol*, doi:10.1111/exd.13027 (2016).
- 47 Belmont, H. M., Abramson, S. B. & Lie, J. T. Pathology and pathogenesis of vascular injury in systemic lupus erythematosus. Interactions of inflammatory cells and activated endothelium. *Arthritis Rheum* **39**, 9-22 (1996).
- 48 Cazander, G., Jukema, G. N. & Nibbering, P. H. Complement activation and inhibition in wound healing. *Clin Dev Immunol* **2012**, 534291, doi:10.1155/2012/534291 (2012).
- 49 Enyedi, B. & Niethammer, P. Mechanisms of epithelial wound detection. *Trends Cell Biol* **25**, 398-407, doi:10.1016/j.tcb.2015.02.007 (2015).
- 50 Roca-Cusachs, P., Sunyer, R. & Trepast, X. Mechanical guidance of cell migration: lessons from chemotaxis. *Curr Opin Cell Biol* **25**, 543-549, doi:10.1016/j.ceb.2013.04.010 (2013).
- 51 Dinarello, C. A. Historical insights into cytokines. *Eur J Immunol* **37 Suppl 1**, S34-45, doi:10.1002/eji.200737772 (2007).
- 52 Kubo, M., Kikuchi, K., Nashiro, K., Kakinuma, T., Hayashi, N., Nanko, H. & Tamaki, K. Expression of fibrogenic cytokines in desmoplastic malignant melanoma. *Br J Dermatol* **139**, 192-197 (1998).
- 53 Maxson, S., Lopez, E. A., Yoo, D., Danilkovitch-Miagkova, A. & Leroux, M. A. Concise review: role of mesenchymal stem cells in wound repair. *Stem Cells Transl Med* **1**, 142-149, doi:10.5966/sctm.2011-0018 (2012).
- 54 Culav, E. M., Clark, C. H. & Merrilees, M. J. Connective tissues: matrix composition and its relevance to physical therapy. *Phys Ther* **79**, 308-319 (1999).
- 55 Birbrair, A., Zhang, T., Files, D. C., Mannava, S., Smith, T., Wang, Z. M., Messi, M. L., Mintz, A. & Delbono, O. Type-1 pericytes accumulate after tissue injury and produce collagen in an organ-dependent manner. *Stem Cell Res Ther* **5**, 122, doi:10.1186/scrt512 (2014).
- 56 Hens, J. R. & Wysolmerski, J. J. Key stages of mammary gland development: molecular mechanisms involved in the formation of the embryonic mammary gland. *Breast Cancer Res* **7**, 220-224, doi:10.1186/bcr1306 (2005).
- 57 Booth, A. J. & Bishop, D. K. TGF-beta, IL-6, IL-17 and CTGF direct multiple pathologies of chronic cardiac allograft rejection. *Immunotherapy* **2**, 511-520, doi:10.2217/imt.10.33 (2010).
- 58 Booth, A. J., Csencsits-Smith, K., Wood, S. C., Lu, G., Lipson, K. E. & Bishop, D. K. Connective tissue growth factor promotes fibrosis

- downstream of TGFbeta and IL-6 in chronic cardiac allograft rejection. *Am J Transplant* **10**, 220-230, doi:10.1111/j.1600-6143.2009.02826.x (2010).
- 59 Gressner, O. A., Peredniene, I. & Gressner, A. M. Connective tissue growth factor reacts as an IL-6/STAT3-regulated hepatic negative acute phase protein. *World J Gastroenterol* **17**, 151-163, doi:10.3748/wjg.v17.i2.151 (2011).
- 60 Kireeva, M. L., Latinkic, B. V., Kolesnikova, T. V., Chen, C. C., Yang, G. P., Abler, A. S. & Lau, L. F. Cyr61 and Fisp12 are both ECM-associated signaling molecules: activities, metabolism, and localization during development. *Exp Cell Res* **233**, 63-77, doi:10.1006/excr.1997.3548 (1997).
- 61 Li, G. M., Shi, Y., Li, D. G., Xie, Q., Guo, Q. & Jin, Y. X. [Effect of small interfering RNA targeting connective tissue growth factor on the synthesis and secretion of extracellular matrix in hepatic stellate cells]. *Zhonghua Gan Zang Bing Za Zhi* **12**, 526-529 (2004).
- 62 Xie, D., Nakachi, K., Wang, H., Elashoff, R. & Koeffler, H. P. Elevated levels of connective tissue growth factor, WISP-1, and CYR61 in primary breast cancers associated with more advanced features. *Cancer Res* **61**, 8917-8923 (2001).
- 63 Xie, D., Yin, D., Wang, H. J., Liu, G. T., Elashoff, R., Black, K. & Koeffler, H. P. Levels of expression of CYR61 and CTGF are prognostic for tumor progression and survival of individuals with gliomas. *Clin Cancer Res* **10**, 2072-2081 (2004).
- 64 Aikawa, T., Gunn, J., Spong, S. M., Klaus, S. J. & Korc, M. Connective tissue growth factor-specific antibody attenuates tumor growth, metastasis, and angiogenesis in an orthotopic mouse model of pancreatic cancer. *Mol Cancer Ther* **5**, 1108-1116, doi:10.1158/1535-7163.mct-05-0516 (2006).
- 65 Chen, P. P., Li, W. J., Wang, Y., Zhao, S., Li, D. Y., Feng, L. Y., Shi, X. L., Koeffler, H. P., Tong, X. J. & Xie, D. Expression of Cyr61, CTGF, and WISP-1 correlates with clinical features of lung cancer. *PLoS One* **2**, e534, doi:10.1371/journal.pone.0000534 (2007).
- 66 Kwon, S., Munroe, X., Crawley, S. C., Lee, H. Y., Spong, S., Bradham, D., Gum, J. R., Jr., Sleisenger, M. H. & Kim, Y. S. Expression of connective tissue growth factor in pancreatic cancer cell lines. *Int J Oncol* **31**, 693-703 (2007).
- 67 Ben Amar, M. & Wu, M. Re-epithelialization: advancing epithelium frontier during wound healing. *J R Soc Interface* **11**, 20131038, doi:10.1098/rsif.2013.1038 (2014).
- 68 Richardson, R., Metzger, M., Knyphausen, P., Ramezani, T., Slanchev, K., Kraus, C., Schmelzer, E. & Hammerschmidt, M. Re-epithelialization of cutaneous wounds in adult zebrafish uses a combination of mechanisms at play during wound closure in embryonic and adult mammals. *Development*, doi:10.1242/dev.130492 (2016).
- 69 Chang, H. M., Huang, W. Y., Lin, S. J., Huang, W. C., Shen, C. R., Mao, W. Y. & Shen, C. N. ABCG2 deficiency in skin impairs re-epithelialization

- in cutaneous wound healing. *Exp Dermatol* **25**, 355-361, doi:10.1111/exd.12936 (2016).
- 70 Qureshi, R., Arora, H. & Rizvi, M. A. EMT in cervical cancer: its role in tumour progression and response to therapy. *Cancer Lett* **356**, 321-331, doi:10.1016/j.canlet.2014.09.021 (2015).
- 71 Li, Y. M., Xu, S. C., Li, J., Han, K. Q., Pi, H. F., Zheng, L., Zuo, G. H., Huang, X. B., Li, H. Y., Zhao, H. Z., Yu, Z. P., Zhou, Z. & Liang, P. Epithelial-mesenchymal transition markers expressed in circulating tumor cells in hepatocellular carcinoma patients with different stages of disease. *Cell Death Dis* **4**, e831, doi:10.1038/cddis.2013.347 (2013).
- 72 Bharti, R., Dey, G. & Mandal, M. Cancer development, chemoresistance, epithelial to mesenchymal transition and stem cells: A snapshot of IL-6 mediated involvement. *Cancer Lett* **375**, 51-61, doi:10.1016/j.canlet.2016.02.048 (2016).
- 73 Cordenonsi, M., Zanconato, F., Azzolin, L., Forcato, M., Rosato, A., Frasson, C., Inui, M., Montagner, M., Parenti, A. R., Poletti, A., Daidone, M. G., Dupont, S., Basso, G., Bicciato, S. & Piccolo, S. The Hippo transducer TAZ confers cancer stem cell-related traits on breast cancer cells. *Cell* **147**, 759-772, doi:10.1016/j.cell.2011.09.048 (2011).
- 74 Jungert, K., Buck, A., von Wichert, G., Adler, G., Konig, A., Buchholz, M., Gress, T. M. & Ellenrieder, V. Sp1 is required for transforming growth factor-beta-induced mesenchymal transition and migration in pancreatic cancer cells. *Cancer Res* **67**, 1563-1570, doi:10.1158/0008-5472.can-06-1670 (2007).
- 75 Colomiere, M., Ward, A. C., Riley, C., Trenerry, M. K., Cameron-Smith, D., Findlay, J., Ackland, L. & Ahmed, N. Cross talk of signals between EGFR and IL-6R through JAK2/STAT3 mediate epithelial-mesenchymal transition in ovarian carcinomas. *Br J Cancer* **100**, 134-144, doi:10.1038/sj.bjc.6604794 (2009).
- 76 Yadav, A., Kumar, B., Datta, J., Teknos, T. N. & Kumar, P. IL-6 promotes head and neck tumor metastasis by inducing epithelial-mesenchymal transition via the JAK-STAT3-SNAIL signaling pathway. *Mol Cancer Res* **9**, 1658-1667, doi:10.1158/1541-7786.mcr-11-0271 (2011).
- 77 Rokavec, M., Oner, M. G., Li, H., Jackstadt, R., Jiang, L., Lodygin, D., Kaller, M., Horst, D., Ziegler, P. K., Schwitalla, S., Slotta-Huspenina, J., Bader, F. G., Greten, F. R. & Hermeking, H. IL-6R/STAT3/miR-34a feedback loop promotes EMT-mediated colorectal cancer invasion and metastasis. *J Clin Invest* **124**, 1853-1867, doi:10.1172/jci73531 (2014).
- 78 Logullo, A. F., Nonogaki, S., Pasini, F. S., Osorio, C. A., Soares, F. A. & Brentani, M. M. Concomitant expression of epithelial-mesenchymal transition biomarkers in breast ductal carcinoma: association with progression. *Oncol Rep* **23**, 313-320 (2010).
- 79 Hu, M., Carroll, D. K., Weremowicz, S., Chen, H., Carrasco, D., Richardson, A., Bissell, M., Violette, S., Gelman, R. S., Schnitt, S. & Polyak, K. (2008).

- 80 Hirano, T., Yasukawa, K., Harada, H., Taga, T., Watanabe, Y., Matsuda, T., Kashiwamura, S., Nakajima, K., Koyama, K., Iwamatsu, A. & et al. Complementary DNA for a novel human interleukin (BSF-2) that induces B lymphocytes to produce immunoglobulin. *Nature* **324**, 73-76, doi:10.1038/324073a0 (1986).
- 81 Hodge, D. R., Hurt, E. M. & Farrar, W. L. The role of IL-6 and STAT3 in inflammation and cancer. *Eur J Cancer* **41**, 2502-2512, doi:10.1016/j.ejca.2005.08.016 (2005).
- 82 Hsieh, F. C., Cheng, G. & Lin, J. Evaluation of potential Stat3-regulated genes in human breast cancer. *Biochem Biophys Res Commun* **335**, 292-299, doi:10.1016/j.bbrc.2005.07.075 (2005).
- 83 Zhong, Z., Wen, Z. & Darnell, J. E., Jr. Stat3: a STAT family member activated by tyrosine phosphorylation in response to epidermal growth factor and interleukin-6. *Science* **264**, 95-98 (1994).
- 84 Xu, Q., Briggs, J., Park, S., Niu, G., Kortylewski, M., Zhang, S., Gritsko, T., Turkson, J., Kay, H., Semenza, G. L., Cheng, J. Q., Jove, R. & Yu, H. Targeting Stat3 blocks both HIF-1 and VEGF expression induced by multiple oncogenic growth signaling pathways. *Oncogene* **24**, 5552-5560, doi:10.1038/sj.onc.1208719 (2005).
- 85 Yu, H., Kortylewski, M. & Pardoll, D. Crosstalk between cancer and immune cells: role of STAT3 in the tumour microenvironment. *Nat Rev Immunol* **7**, 41-51, doi:10.1038/nri1995 (2007).
- 86 Hodge, D. R., Xiao, W., Wang, L. H., Li, D. & Farrar, W. L. Activating mutations in STAT3 and STAT5 differentially affect cellular proliferation and apoptotic resistance in multiple myeloma cells. *Cancer Biol Ther* **3**, 188-194 (2004).
- 87 Huang, C. & Xie, K. Crosstalk of Sp1 and Stat3 signaling in pancreatic cancer pathogenesis. *Cytokine Growth Factor Rev* **23**, 25-35, doi:10.1016/j.cytogfr.2012.01.003 (2012).
- 88 Tapias, A., Ciudad, C. J., Roninson, I. B. & Noe, V. Regulation of Sp1 by cell cycle related proteins. *Cell Cycle* **7**, 2856-2867 (2008).
- 89 Lu, S. & Archer, M. C. Sp1 coordinately regulates de novo lipogenesis and proliferation in cancer cells. *Int J Cancer* **126**, 416-425, doi:10.1002/ijc.24761 (2010).
- 90 Kong, L. M., Liao, C. G., Fei, F., Guo, X., Xing, J. L. & Chen, Z. N. Transcription factor Sp1 regulates expression of cancer-associated molecule CD147 in human lung cancer. *Cancer Sci* **101**, 1463-1470, doi:10.1111/j.1349-7006.2010.01554.x (2010).
- 91 Choi, E. S., Nam, J. S., Jung, J. Y., Cho, N. P. & Cho, S. D. Modulation of specificity protein 1 by mithramycin A as a novel therapeutic strategy for cervical cancer. *Sci Rep* **4**, 7162, doi:10.1038/srep07162 (2014).
- 92 Zhang, J. P., Zhang, H., Wang, H. B., Li, Y. X., Liu, G. H., Xing, S., Li, M. Z. & Zeng, M. S. Down-regulation of Sp1 suppresses cell proliferation, clonogenicity and the expressions of stem cell markers in nasopharyngeal carcinoma. *J Transl Med* **12**, 222, doi:10.1186/s12967-014-0222-1 (2014).

- 93 Canaff, L., Zhou, X. & Hendy, G. N. The proinflammatory cytokine, interleukin-6, up-regulates calcium-sensing receptor gene transcription via Stat1/3 and Sp1/3. *J Biol Chem* **283**, 13586-13600, doi:10.1074/jbc.M708087200 (2008).
- 94 Cantwell, C. A., Sterneck, E. & Johnson, P. F. Interleukin-6-specific activation of the C/EBPdelta gene in hepatocytes is mediated by Stat3 and Sp1. *Mol Cell Biol* **18**, 2108-2117 (1998).
- 95 Shi, Q., Le, X., Abbruzzese, J. L., Peng, Z., Qian, C. N., Tang, H., Xiong, Q., Wang, B., Li, X. C. & Xie, K. Constitutive Sp1 activity is essential for differential constitutive expression of vascular endothelial growth factor in human pancreatic adenocarcinoma. *Cancer Res* **61**, 4143-4154 (2001).
- 96 An integrated encyclopedia of DNA elements in the human genome. *Nature* **489**, 57-74, doi:10.1038/nature11247 (2012).
- 97 Cicha, I., Yilmaz, A., Klein, M., Raithel, D., Brigstock, D. R., Daniel, W. G., Goppelt-Struebe, M. & Garlisch, C. D. Connective tissue growth factor is overexpressed in complicated atherosclerotic plaques and induces mononuclear cell chemotaxis in vitro. *Arterioscler Thromb Vasc Biol* **25**, 1008-1013, doi:10.1161/01.ATV.0000162173.27682.7b (2005).
- 98 Xie, S., Sukkar, M. B., Issa, R., Oltmanns, U., Nicholson, A. G. & Chung, K. F. Regulation of TGF-beta 1-induced connective tissue growth factor expression in airway smooth muscle cells. *Am J Physiol Lung Cell Mol Physiol* **288**, L68-76, doi:10.1152/ajplung.00156.2004 (2005).
- 99 Crean, J. K., Furlong, F., Mitchell, D., McArdle, E., Godson, C. & Martin, F. Connective tissue growth factor/CCN2 stimulates actin disassembly through Akt/protein kinase B-mediated phosphorylation and cytoplasmic translocation of p27(Kip-1). *Faseb j* **20**, 1712-1714, doi:10.1096/fj.05-5010fje (2006).
- 100 Burns, W. C., Twigg, S. M., Forbes, J. M., Pete, J., Tikellis, C., Thallas-Bonke, V., Thomas, M. C., Cooper, M. E. & Kantharidis, P. Connective tissue growth factor plays an important role in advanced glycation end product-induced tubular epithelial-to-mesenchymal transition: implications for diabetic renal disease. *J Am Soc Nephrol* **17**, 2484-2494, doi:10.1681/asn.2006050525 (2006).
- 101 Gressner, O. A. & Gressner, A. M. Connective tissue growth factor: a fibrogenic master switch in fibrotic liver diseases. *Liver Int* **28**, 1065-1079, doi:10.1111/j.1478-3231.2008.01826.x (2008).
- 102 Li, G., Xie, Q., Shi, Y., Li, D., Zhang, M., Jiang, S., Zhou, H., Lu, H. & Jin, Y. Inhibition of connective tissue growth factor by siRNA prevents liver fibrosis in rats. *J Gene Med* **8**, 889-900, doi:10.1002/jgm.894 (2006).
- 103 Chan, S. W., Lim, C. J., Loo, L. S., Chong, Y. F., Huang, C. & Hong, W. TEADs mediate nuclear retention of TAZ to promote oncogenic transformation. *J Biol Chem* **284**, 14347-14358, doi:10.1074/jbc.M901568200 (2009).
- 104 Pobbati, A. V. & Hong, W. Emerging roles of TEAD transcription factors and its coactivators in cancers. *Cancer Biol Ther* **14**, 390-398, doi:10.4161/cbt.23788 (2013).

- 105 Zhou, Z., Hu, T., Xu, Z., Lin, Z., Zhang, Z., Feng, T., Zhu, L., Rong, Y., Shen, H., Luk, J. M., Zhang, X. & Qin, N. Targeting Hippo pathway by specific interruption of YAP-TEAD interaction using cyclic YAP-like peptides. *Faseb j* **29**, 724-732, doi:10.1096/fj.14-262980 (2015).
- 106 Lamar, J. M., Stern, P., Liu, H., Schindler, J. W., Jiang, Z. G. & Hynes, R. O. The Hippo pathway target, YAP, promotes metastasis through its TEAD-interaction domain. *Proc Natl Acad Sci U S A* **109**, E2441-2450, doi:10.1073/pnas.1212021109 (2012).
- 107 Lee, M. J., Ran Byun, M., Furutani-Seiki, M., Hong, J. H. & Jung, H. S. YAP and TAZ regulate skin wound healing. *J Invest Dermatol* **134**, 518-525, doi:10.1038/jid.2013.339 (2014).
- 108 Hsu, Y. L., Hung, J. Y., Chou, S. H., Huang, M. S., Tsai, M. J., Lin, Y. S., Chiang, S. Y., Ho, Y. W., Wu, C. Y. & Kuo, P. L. Angiomotin decreases lung cancer progression by sequestering oncogenic YAP/TAZ and decreasing Cyr61 expression. *Oncogene* **34**, 4056-4068, doi:10.1038/onc.2014.333 (2015).
- 109 Xu, T., Wang, W., Zhang, S., Stewart, R. A. & Yu, W. Identifying tumor suppressors in genetic mosaics: the *Drosophila* *lats* gene encodes a putative protein kinase. *Development* **121**, 1053-1063 (1995).
- 110 Moroishi, T., Hansen, C. G. & Guan, K. L. The emerging roles of YAP and TAZ in cancer. *Nat Rev Cancer* **15**, 73-79, doi:10.1038/nrc3876 (2015).
- 111 Justice, R. W., Zilian, O., Woods, D. F., Noll, M. & Bryant, P. J. The *Drosophila* tumor suppressor gene *warts* encodes a homolog of human myotonic dystrophy kinase and is required for the control of cell shape and proliferation. *Genes Dev* **9**, 534-546 (1995).
- 112 Pan, D. Hippo signaling in organ size control. *Genes & development* **21**, 886-897, doi:10.1101/gad.1536007 (2007).
- 113 Huang, J., Wu, S., Barrera, J., Matthews, K. & Pan, D. The Hippo signaling pathway coordinately regulates cell proliferation and apoptosis by inactivating Yorkie, the *Drosophila* Homolog of YAP. *Cell* **122**, 421-434, doi:10.1016/j.cell.2005.06.007 (2005).
- 114 Harvey, K. F., Zhang, X. & Thomas, D. M. The Hippo pathway and human cancer. *Nat Rev Cancer* **13**, 246-257, doi:http://www.nature.com/nrc/journal/v13/n4/suppinfo/nrc3458_S1.html (2013).
- 115 Zhao, B., Tumaneng, K. & Guan, K.-L. The Hippo pathway in organ size control, tissue regeneration and stem cell self-renewal. *Nature cell biology* **13**, 877-883 (2011).
- 116 Yuen, H. F., McCrudden, C. M., Huang, Y. H., Tham, J. M., Zhang, X., Zeng, Q., Zhang, S. D. & Hong, W. TAZ expression as a prognostic indicator in colorectal cancer. *PLoS One* **8**, e54211, doi:10.1371/journal.pone.0054211 (2013).
- 117 Hong, W. Angiomotin'g YAP into the nucleus for cell proliferation and cancer development. *Sci Signal* **6**, pe27, doi:10.1126/scisignal.2004573 (2013).

- 118 Hong, L., Cai, Y., Jiang, M., Zhou, D. & Chen, L. The Hippo signaling pathway in liver regeneration and tumorigenesis. *Acta Biochim Biophys Sin (Shanghai)* **47**, 46-52, doi:10.1093/abbs/gmu106 (2015).
- 119 Zhang, K., Qi, H. X., Hu, Z. M., Chang, Y. N., Shi, Z. M., Han, X. H., Han, Y. W., Zhang, R. X., Zhang, Z., Chen, T. & Hong, W. YAP and TAZ Take Center Stage in Cancer. *Biochemistry* **54**, 6555-6566, doi:10.1021/acs.biochem.5b01014 (2015).
- 120 Calvo, F., Ege, N., Grande-Garcia, A., Hooper, S., Jenkins, R. P., Chaudhry, S. I., Harrington, K., Williamson, P., Moeendarbary, E., Charras, G. & Sahai, E. Mechanotransduction and YAP-dependent matrix remodelling is required for the generation and maintenance of cancer-associated fibroblasts. *Nat Cell Biol* **15**, 637-646, doi:10.1038/ncb2756 (2013).
- 121 Kim, T., Yang, S. J., Hwang, D., Song, J., Kim, M., Kyum Kim, S., Kang, K., Ahn, J., Lee, D., Kim, M. Y., Kim, S., Seung Koo, J., Seok Koh, S., Kim, S. Y. & Lim, D. S. A basal-like breast cancer-specific role for SRF-IL6 in YAP-induced cancer stemness. *Nat Commun* **6**, 10186, doi:10.1038/ncomms10186 (2015).
- 122 Zhang, N., Bai, H., David, K. K., Dong, J., Zheng, Y., Cai, J., Giovannini, M., Liu, P., Anders, R. A. & Pan, D. The Merlin/NF2 tumor suppressor functions through the YAP oncoprotein to regulate tissue homeostasis in mammals. *Dev Cell* **19**, 27-38, doi:10.1016/j.devcel.2010.06.015 (2010).
- 123 Zhang, W., Nandakumar, N., Shi, Y., Manzano, M., Smith, A., Graham, G., Gupta, S., Vietsch, E. E., Laughlin, S. Z., Wadhwa, M., Chetram, M., Joshi, M., Wang, F., Kallakury, B., Toretzky, J., Wellstein, A. & Yi, C. Downstream of mutant KRAS, the transcription regulator YAP is essential for neoplastic progression to pancreatic ductal adenocarcinoma. *Sci Signal* **7**, ra42, doi:10.1126/scisignal.2005049 (2014).
- 124 Kapoor, A., Yao, W., Ying, H., Hua, S., Liewen, A., Wang, Q., Zhong, Y., Wu, C. J., Sadanandam, A., Hu, B., Chang, Q., Chu, G. C., Al-Khalil, R., Jiang, S., Xia, H., Fletcher-Sananikone, E., Lim, C., Horwitz, G. I., Viale, A., Pettazzoni, P., Sanchez, N., Wang, H., Protopopov, A., Zhang, J., Heffernan, T., Johnson, R. L., Chin, L., Wang, Y. A., Draetta, G. & DePinho, R. A. Yap1 activation enables bypass of oncogenic Kras addiction in pancreatic cancer. *Cell* **158**, 185-197, doi:10.1016/j.cell.2014.06.003 (2014).
- 125 Shao, D. D., Xue, W., Krall, E. B., Bhutkar, A., Piccioni, F., Wang, X., Schinzel, A. C., Sood, S., Rosenbluh, J., Kim, J. W., Zwang, Y., Roberts, T. M., Root, D. E., Jacks, T. & Hahn, W. C. KRAS and YAP1 converge to regulate EMT and tumor survival. *Cell* **158**, 171-184, doi:10.1016/j.cell.2014.06.004 (2014).
- 126 Zhao, B., Li, L., Lu, Q., Wang, L. H., Liu, C. Y., Lei, Q. & Guan, K. L. Angiomotin is a novel Hippo pathway component that inhibits YAP oncoprotein. *Genes Dev* **25**, 51-63, doi:10.1101/gad.2000111 (2011).
- 127 Bossuyt, W., Chen, C. L., Chen, Q., Sudol, M., McNeill, H., Pan, D., Kopp, A. & Halder, G. An evolutionary shift in the regulation of the Hippo

- pathway between mice and flies. *Oncogene* **33**, 1218-1228, doi:10.1038/onc.2013.82 (2014).
- 128 Bratt, A., Wilson, W. J., Troyanovsky, B., Aase, K., Kessler, R., Van Meir, E. G. & Holmgren, L. Angiomotin belongs to a novel protein family with conserved coiled-coil and PDZ binding domains. *Gene* **298**, 69-77 (2002).
- 129 Bratt, A., Birot, O., Sinha, I., Veitonmaki, N., Aase, K., Ernkvist, M. & Holmgren, L. Angiomotin regulates endothelial cell-cell junctions and cell motility. *J Biol Chem* **280**, 34859-34869, doi:10.1074/jbc.M503915200 (2005).
- 130 Jiang, W. G., Watkins, G., Douglas-Jones, A., Holmgren, L. & Mansel, R. E. Angiomotin and angiomotin like proteins, their expression and correlation with angiogenesis and clinical outcome in human breast cancer. *BMC Cancer* **6**, 16, doi:10.1186/1471-2407-6-16 (2006).
- 131 Lv, M., Lv, M., Chen, L., Qin, T., Zhang, X., Liu, P. & Yang, J. Angiomotin promotes breast cancer cell proliferation and invasion. *Oncol Rep* **33**, 1938-1946, doi:10.3892/or.2015.3780 (2015).
- 132 Moleirinho, S., Guerrant, W. & Kissil, J. L. The Angiomotins--from discovery to function. *FEBS Lett* **588**, 2693-2703, doi:10.1016/j.febslet.2014.02.006 (2014).
- 133 Wang, C., An, J., Zhang, P., Xu, C., Gao, K., Wu, D., Wang, D., Yu, H., Liu, J. O. & Yu, L. The Nedd4-like ubiquitin E3 ligases target angiomotin/p130 to ubiquitin-dependent degradation. *Biochem J* **444**, 279-289, doi:10.1042/bj20111983 (2012).
- 134 Gagne, V., Moreau, J., Plourde, M., Lapointe, M., Lord, M., Gagnon, E. & Fernandes, M. J. Human angiomotin-like 1 associates with an angiomotin protein complex through its coiled-coil domain and induces the remodeling of the actin cytoskeleton. *Cell Motil Cytoskeleton* **66**, 754-768, doi:10.1002/cm.20405 (2009).
- 135 Adler, J. J., Heller, B. L., Bringman, L. R., Ranahan, W. P., Cocklin, R. R., Goebel, M. G., Oh, M., Lim, H. S., Ingham, R. J. & Wells, C. D. Amot130 adapts atrophin-1 interacting protein 4 to inhibit yes-associated protein signaling and cell growth. *J Biol Chem* **288**, 15181-15193, doi:10.1074/jbc.M112.446534 (2013).
- 136 Adler, J. J., Johnson, D. E., Heller, B. L., Bringman, L. R., Ranahan, W. P., Conwell, M. D., Sun, Y., Hudmon, A. & Wells, C. D. Serum deprivation inhibits the transcriptional co-activator YAP and cell growth via phosphorylation of the 130-kDa isoform of Angiomotin by the LATS1/2 protein kinases. *Proc Natl Acad Sci U S A* **110**, 17368-17373, doi:10.1073/pnas.1308236110 (2013).
- 137 Ernkvist, M., Aase, K., Ukomadu, C., Wohlschlegel, J., Blackman, R., Veitonmaki, N., Bratt, A., Dutta, A. & Holmgren, L. p130-angiomotin associates to actin and controls endothelial cell shape. *Febs j* **273**, 2000-2011, doi:10.1111/j.1742-4658.2006.05216.x (2006).
- 138 Ernkvist, M., Birot, O., Sinha, I., Veitonmaki, N., Nystrom, S., Aase, K. & Holmgren, L. Differential roles of p80- and p130-angiomotin in the switch

- between migration and stabilization of endothelial cells. *Biochim Biophys Acta* **1783**, 429-437, doi:10.1016/j.bbamcr.2007.11.018 (2008).
- 139 Yi, C., Shen, Z., Stemmer-Rachamimov, A., Dawany, N., Troutman, S., Showe, L. C., Liu, Q., Shimono, A., Sudol, M., Holmgren, L., Stanger, B. Z. & Kissil, J. L. The p130 isoform of angiomin is required for Yap-mediated hepatic epithelial cell proliferation and tumorigenesis. *Sci Signal* **6**, ra77, doi:10.1126/scisignal.2004060 (2013).
- 140 Katikireddy, K. R. & O'Sullivan, F. Immunohistochemical and immunofluorescence procedures for protein analysis. *Methods Mol Biol* **784**, 155-167, doi:10.1007/978-1-61779-289-2_11 (2011).
- 141 Hall, P. A. & Lane, D. P. p53 in tumour pathology: can we trust immunohistochemistry?--Revisited! *J Pathol* **172**, 1-4, doi:10.1002/path.1711720103 (1994).
- 142 Harvey, J. M., Clark, G. M., Osborne, C. K. & Allred, D. C. Estrogen receptor status by immunohistochemistry is superior to the ligand-binding assay for predicting response to adjuvant endocrine therapy in breast cancer. *J Clin Oncol* **17**, 1474-1481 (1999).
- 143 Garola, R. E. & McGuire, W. L. A hydroxylapatite micromethod for measuring estrogen receptor in human breast cancer. *Cancer Res* **38**, 2216-2220 (1978).
- 144 Matos, L. L., Trufelli, D. C., de Matos, M. G. & da Silva Pinhal, M. A. Immunohistochemistry as an important tool in biomarkers detection and clinical practice. *Biomark Insights* **5**, 9-20 (2010).
- 145 Rimm, D. L. What brown cannot do for you. *Nat Biotechnol* **24**, 914-916, doi:10.1038/nbt0806-914 (2006).
- 146 Bradley, W. H., Eng, K., Le, M., Mackinnon, A. C., Kendzierski, C. & Rader, J. S. Comparing gene expression data from formalin-fixed, paraffin embedded tissues and qPCR with that from snap-frozen tissue and microarrays for modeling outcomes of patients with ovarian carcinoma. *BMC Clin Pathol* **15**, 17, doi:10.1186/s12907-015-0017-1 (2015).
- 147 Baschong, W., Suetterlin, R. & Laeng, R. H. Control of Autofluorescence of Archival Formaldehyde-fixed, Paraffin-embedded Tissue in Confocal Laser Scanning Microscopy (CLSM). *Journal of Histochemistry & Cytochemistry* **49**, 1565-1571, doi:10.1177/002215540104901210 (2001).
- 148 Kajimura, J., Ito, R., Manley, N. R. & Hale, L. P. Optimization of Single- and Dual-Color Immunofluorescence Protocols for Formalin-Fixed, Paraffin-Embedded Archival Tissues. *J Histochem Cytochem* **64**, 112-124, doi:10.1369/0022155415610792 (2016).
- 149 Breslin, T. M., Xu, F., Palmer, G. M., Zhu, C., Gilchrist, K. W. & Ramanujam, N. Autofluorescence and diffuse reflectance properties of malignant and benign breast tissues. *Ann Surg Oncol* **11**, 65-70 (2004).
- 150 Cowen, T., Haven, A. J. & Burnstock, G. Pontamine sky blue: A counterstain for background autofluorescence in fluorescence and immunofluorescence histochemistry. *Histochemistry and Cell Biology* **82**, 205-208, doi:10.1007/BF00501396 (1985).

- 151 Mori, H., Borowsky, A. D., Bhat, R., Ghajar, C. M., Seiki, M. & Bissell, M. J. Laser scanning-based tissue autofluorescence/fluorescence imaging (LS-TAFI), a new technique for analysis of microanatomy in whole-mount tissues. *Am J Pathol* **180**, 2249-2256, doi:10.1016/j.ajpath.2012.02.032 (2012).
- 152 Neumann, M. & Gabel, D. Simple Method for Reduction of Autofluorescence in Fluorescence Microscopy. *Journal of Histochemistry & Cytochemistry* **50**, 437-439, doi:10.1177/002215540205000315 (2002).
- 153 Schnell, S. A., Staines, W. A. & Wessendorf, M. W. Reduction of Lipofuscin-like Autofluorescence in Fluorescently Labeled Tissue. *Journal of Histochemistry & Cytochemistry* **47**, 719-730, doi:10.1177/002215549904700601 (1999).
- 154 Van de Lest, C. H., Versteeg, E. M., Veerkamp, J. H. & Van Kuppevelt, T. H. Elimination of autofluorescence in immunofluorescence microscopy with digital image processing. *Journal of Histochemistry & Cytochemistry* **43**, 727-730, doi:10.1177/43.7.7608528 (1995).
- 155 Viegas, M. S., Martins, T. C., Seco, F. & do Carmo, A. An improved and cost-effective methodology for the reduction of autofluorescence in direct immunofluorescence studies on formalin-fixed paraffin-embedded tissues. *Eur J Histochem* **51**, 59-66 (2007).
- 156 Palmer, G. M., Keely, P. J., Breslin, T. M. & Ramanujam, N. Autofluorescence spectroscopy of normal and malignant human breast cell lines. *Photochem Photobiol* **78**, 462-469 (2003).
- 157 Kumar, B. S., Sandhyamani, S., Nazeer, S. S. & Jayasree, R. S. Rapid and simple method of photobleaching to reduce background autofluorescence in lung tissue sections. *Indian J Biochem Biophys* **52**, 107-110 (2015).
- 158 Erben, T., Ossig, R., Naim, H. Y. & Schnekenburger, J. What to do with high autofluorescence background in pancreatic tissues - an efficient Sudan Black B quenching method for specific immunofluorescence labeling. *Histopathology*, doi:10.1111/his.12935 (2016).
- 159 Davis, A. S., Richter, A., Becker, S., Moyer, J. E., Sandouk, A., Skinner, J. & Taubenberger, J. K. Characterizing and Diminishing Autofluorescence in Formalin-fixed Paraffin-embedded Human Respiratory Tissue. *J Histochem Cytochem* **62**, 405-423, doi:10.1369/0022155414531549 (2014).
- 160 Fowler, C. B., Evers, D. L., O'Leary, T. J. & Mason, J. T. Antigen Retrieval Causes Protein Unfolding: Evidence for a Linear Epitope Model of Recovered Immunoreactivity. *Journal of Histochemistry and Cytochemistry* **59**, 366-381, doi:10.1369/0022155411400866 (2011).
- 161 Wong, H., Lau, S., Yau, T., Cheung, P. & Epstein, R. J. Presence of an *in situ* component is associated with reduced biological aggressiveness of size-matched invasive breast cancer. *Br J Cancer* **102**, 1391-1396, doi:10.1038/sj.bjc.6605655 (2010).
- 162 Dieterich, M., Hartwig, F., Stubert, J., Klocking, S., Kundt, G., Stengel, B., Reimer, T. & Gerber, B. Accompanying DCIS in breast cancer patients

- with invasive ductal carcinoma is predictive of improved local recurrence-free survival. *Breast* **23**, 346-351, doi:10.1016/j.breast.2014.01.015 (2014).
- 163 Wells, C. D., Fawcett, J. P., Traweger, A., Yamanaka, Y., Goudreault, M., Elder, K., Kulkarni, S., Gish, G., Virag, C., Lim, C., Colwill, K., Starostine, A., Metalnikov, P. & Pawson, T. A Rich1/Amot complex regulates the Cdc42 GTPase and apical-polarity proteins in epithelial cells. *Cell* **125**, 535-548, doi:10.1016/j.cell.2006.02.045 (2006).
- 164 Heller, B., Adu-Gyamfi, E., Smith-Kinnaman, W., Babbey, C., Vora, M., Xue, Y., Bittman, R., Stahelin, R. V. & Wells, C. D. Amot recognizes a juxtannuclear endocytic recycling compartment via a novel lipid binding domain. *J Biol Chem* **285**, 12308-12320, doi:10.1074/jbc.M109.096230 (2010).
- 165 Lv, M., Li, S., Luo, C., Zhang, X., Shen, Y., Sui, Y. X., Wang, F., Wang, X., Yang, J., Liu, P. & Yang, J. Angiomotin promotes renal epithelial and carcinoma cell proliferation by retaining the nuclear YAP. *Oncotarget* **7**, 12393-12403, doi:10.18632/oncotarget.7161 (2016).
- 166 Holmgren, L., Ambrosino, E., Birot, O., Tullus, C., Veitonmaki, N., Levchenko, T., Carlson, L. M., Musiani, P., Iezzi, M., Curcio, C., Forni, G., Cavallo, F. & Kiessling, R. A DNA vaccine targeting angiomotin inhibits angiogenesis and suppresses tumor growth. *Proc Natl Acad Sci U S A* **103**, 9208-9213, doi:10.1073/pnas.0603110103 (2006).
- 167 Barutello, G., Curcio, C., Spadaro, M., Arigoni, M., Trovato, R., Bolli, E., Zheng, Y., Ria, F., Quaglino, E., Iezzi, M., Riccardo, F., Holmgren, L., Forni, G. & Cavallo, F. Antitumor immunization of mothers delays tumor development in cancer-prone offspring. *Oncoimmunology* **4**, e1005500, doi:10.1080/2162402x.2015.1005500 (2015).
- 168 Paramasivam, M., Sarkeshik, A., Yates, J. R., 3rd, Fernandes, M. J. & McCollum, D. Angiomotin family proteins are novel activators of the LATS2 kinase tumor suppressor. *Mol Biol Cell* **22**, 3725-3733, doi:10.1091/mbc.E11-04-0300 (2011).
- 169 Troyanovsky, B., Levchenko, T., Mansson, G., Matvijenko, O. & Holmgren, L. Angiomotin: an angiostatin binding protein that regulates endothelial cell migration and tube formation. *J Cell Biol* **152**, 1247-1254 (2001).
- 170 Benelli, R., Morini, M., Carrozzino, F., Ferrari, N., Minghelli, S., Santi, L., Cassatella, M., Noonan, D. M. & Albini, A. Neutrophils as a key cellular target for angiostatin: implications for regulation of angiogenesis and inflammation. *Faseb j* **16**, 267-269, doi:10.1096/fj.01-0651fje (2002).
- 171 Frohman, M. A., Dush, M. K. & Martin, G. R. Rapid production of full-length cDNAs from rare transcripts: amplification using a single gene-specific oligonucleotide primer. *Proc Natl Acad Sci U S A* **85**, 8998-9002 (1988).
- 172 Hakami, F., Darda, L., Stafford, P., Woll, P., Lambert, D. W. & Hunter, K. D. The roles of HOXD10 in the development and progression of head and

- neck squamous cell carcinoma (HNSCC). *Br J Cancer* **111**, 807-816, doi:10.1038/bjc.2014.372 (2014).
- 173 Lee, J. H., Park, S. M., Kim, O. S., Lee, C. S., Woo, J. H., Park, S. J., Joe, E. H. & Jou, I. Differential SUMOylation of LXRalpha and LXRbeta mediates transrepression of STAT1 inflammatory signaling in IFN-gamma-stimulated brain astrocytes. *Mol Cell* **35**, 806-817, doi:10.1016/j.molcel.2009.07.021 (2009).
- 174 Fouad, T. M., Kogawa, T., Reuben, J. M. & Ueno, N. T. The role of inflammation in inflammatory breast cancer. *Adv Exp Med Biol* **816**, 53-73, doi:10.1007/978-3-0348-0837-8_3 (2014).
- 175 Liu, D., Wang, X. & Chen, Z. Tumor Necrosis Factor-alpha, a Regulator and Therapeutic Agent on Breast Cancer. *Curr Pharm Biotechnol* **17**, 486-494 (2016).
- 176 Yang, L., Han, S. & Sun, Y. An IL6-STAT3 loop mediates resistance to PI3K inhibitors by inducing epithelial-mesenchymal transition and cancer stem cell expansion in human breast cancer cells. *Biochem Biophys Res Commun* **453**, 582-587, doi:10.1016/j.bbrc.2014.09.129 (2014).
- 177 Taniguchi, K., Wu, L. W., Grivennikov, S. I., de Jong, P. R., Lian, I., Yu, F. X., Wang, K., Ho, S. B., Boland, B. S., Chang, J. T., Sandborn, W. J., Hardiman, G., Raz, E., Maehara, Y., Yoshimura, A., Zucman-Rossi, J., Guan, K. L. & Karin, M. A gp130-Src-YAP module links inflammation to epithelial regeneration. *Nature* **519**, 57-62, doi:10.1038/nature14228 (2015).
- 178 Lu, S., Jiao, H., Xu, J., Zheng, Y., Sun, Y. & Chen, H. Downregulation of IL6 Targeted MiR-376b May Contribute to a Positive IL6 Feedback Loop During Early Liver Regeneration in Mice. *Cell Physiol Biochem* **37**, 233-242, doi:10.1159/000430348 (2015).
- 179 Tiberio, G. A., Tiberio, L., Benetti, A., Cervi, E., Montani, N., Dreano, M., Garotta, G., Cerea, K., Steimberg, N., Pandolfo, G., Ferrari-Bravo, A., Mazzoleni, G., Giulini, S. M. & Schiaffonati, L. IL-6 Promotes compensatory liver regeneration in cirrhotic rat after partial hepatectomy. *Cytokine* **42**, 372-378, doi:10.1016/j.cyto.2008.03.012 (2008).
- 180 Yovchev, M., Jaber, F. L., Lu, Z., Patel, S., Locker, J., Rogler, L. E., Murray, J. W., Sudol, M., Dabeva, M. D., Zhu, L. & Shafritz, D. A. Experimental Model for Successful Liver Cell Therapy by Lenti TTR-YapERT2 Transduced Hepatocytes with Tamoxifen Control of Yap Subcellular Location. *Sci Rep* **6**, 19275, doi:10.1038/srep19275 (2016).
- 181 Grijalva, J. L., Huizenga, M., Mueller, K., Rodriguez, S., Brazzo, J., Camargo, F., Sadri-Vakili, G. & Vakili, K. Dynamic alterations in Hippo signaling pathway and YAP activation during liver regeneration. *Am J Physiol Gastrointest Liver Physiol* **307**, G196-204, doi:10.1152/ajpgi.00077.2014 (2014).
- 182 Shi, H., Yang, G., Zheng, T., Wang, J., Li, L., Liang, Y., Xie, C., Yin, D., Sun, B., Sun, J., Wang, H., Pan, S., Jiang, H., Lau, W. & Liu, L. A preliminary study of ALPPS procedure in a rat model. *Sci Rep* **5**, 17567, doi:10.1038/srep17567 (2015).

- 183 Zimmers, T. A., Fishel, M. L. & Bonetto, A. STAT3 in the systemic inflammation of cancer cachexia. *Semin Cell Dev Biol* **54**, 28-41, doi:10.1016/j.semcdb.2016.02.009 (2016).
- 184 Martin, A. I., Nieto-Bona, M. P., Castellero, E., Fernandez-Galaz, C., Lopez-Menduina, M., Gomez-Sanmiguel, A. B., Gomez-Moreira, C., Villanua, M. A. & Lopez-Calderon, A. Effect of cyclooxygenase-2 inhibition by meloxicam, on atrogin-1 and myogenic regulatory factors in skeletal muscle of rats injected with endotoxin. *J Physiol Pharmacol* **63**, 649-659 (2012).
- 185 Zhou, D., Conrad, C., Xia, F., Park, J. S., Payer, B., Yin, Y., Lauwers, G. Y., Thasler, W., Lee, J. T., Avruch, J. & Bardeesy, N. Mst1 and Mst2 maintain hepatocyte quiescence and suppress hepatocellular carcinoma development through inactivation of the Yap1 oncogene. *Cancer Cell* **16**, 425-438, doi:10.1016/j.ccr.2009.09.026 (2009).
- 186 Loeffler, S., Fayard, B., Weis, J. & Weissenberger, J. Interleukin-6 induces transcriptional activation of vascular endothelial growth factor (VEGF) in astrocytes in vivo and regulates VEGF promoter activity in glioblastoma cells via direct interaction between STAT3 and Sp1. *Int J Cancer* **115**, 202-213, doi:10.1002/ijc.20871 (2005).
- 187 Lin, S., Saxena, N. K., Ding, X., Stein, L. L. & Anania, F. A. Leptin increases tissue inhibitor of metalloproteinase I (TIMP-1) gene expression by a specificity protein 1/signal transducer and activator of transcription 3 mechanism. *Mol Endocrinol* **20**, 3376-3388, doi:10.1210/me.2006-0177 (2006).
- 188 Melchionna, R., Bellavia, G., Romani, M., Straino, S., Germani, A., Di Carlo, A., Capogrossi, M. C. & Napolitano, M. C/EBPgamma regulates wound repair and EGF receptor signaling. *J Invest Dermatol* **132**, 1908-1917, doi:10.1038/jid.2012.51 (2012).
- 189 Rao, M., Atay, S. M., Shukla, V., Hong, Y., Upham, T., Ripley, R. T., Hong, J. A., Zhang, M., Reardon, E., Fetsch, P., Miettinen, M., Li, X., Peer, C. J., Sissung, T., Figg, W. D., De Rienzo, A., Bueno, R. & Schump, D. S. Mithramycin Depletes Specificity Protein 1 and Activates p53 to Mediate Senescence and Apoptosis of Malignant Pleural Mesothelioma Cells. *Clin Cancer Res* **22**, 1197-1210, doi:10.1158/1078-0432.ccr-14-3379 (2016).
- 190 Yuan, P., Wang, L., Wei, D., Zhang, J., Jia, Z., Li, Q., Le, X., Wang, H., Yao, J. & Xie, K. Therapeutic inhibition of Sp1 expression in growing tumors by mithramycin a correlates directly with potent antiangiogenic effects on human pancreatic cancer. *Cancer* **110**, 2682-2690, doi:10.1002/cncr.23092 (2007).
- 191 Fernandez-Guizan, A., Mansilla, S., Barcelo, F., Vizcaino, C., Nunez, L. E., Moris, F., Gonzalez, S. & Portugal, J. The activity of a novel mithramycin analog is related to its binding to DNA, cellular accumulation, and inhibition of Sp1-driven gene transcription. *Chem Biol Interact* **219**, 123-132, doi:10.1016/j.cbi.2014.05.019 (2014).

- 192 Saha, S., Mukherjee, S., Mazumdar, M., Manna, A., Khan, P., Adhikary, A., Kajal, K., Jana, D., Sa, G., Mukherjee, S., Sarkar, D. K. & Das, T. Mithramycin A sensitizes therapy-resistant breast cancer stem cells toward genotoxic drug doxorubicin. *Transl Res* **165**, 558-577, doi:10.1016/j.trsl.2014.10.011 (2015).
- 193 Holmes, A., Abraham, D. J., Chen, Y., Denton, C., Shi-wen, X., Black, C. M. & Leask, A. Constitutive connective tissue growth factor expression in scleroderma fibroblasts is dependent on Sp1. *J Biol Chem* **278**, 41728-41733, doi:10.1074/jbc.M305019200 (2003).
- 194 Cordova, G., Rochard, A., Riquelme-Guzman, C., Cofre, C., Scherman, D., Bigey, P. & Brandan, E. SMAD3 and SP1/SP3 Transcription Factors Collaborate to Regulate Connective Tissue Growth Factor Gene Expression in Myoblasts in Response to Transforming Growth Factor beta. *J Cell Biochem* **116**, 1880-1887, doi:10.1002/jcb.25143 (2015).
- 195 Li, J., Du, S., Sheng, X., Liu, J., Cen, B., Huang, F. & He, Y. MicroRNA-29b Inhibits Endometrial Fibrosis by Regulating the Sp1-TGF-beta1/Smad-CTGF Axis in a Rat Model. *Reprod Sci* **23**, 386-394, doi:10.1177/1933719115602768 (2016).
- 196 Liu-Chittenden, Y., Huang, B., Shim, J. S., Chen, Q., Lee, S. J., Anders, R. A., Liu, J. O. & Pan, D. Genetic and pharmacological disruption of the TEAD-YAP complex suppresses the oncogenic activity of YAP. *Genes Dev* **26**, 1300-1305, doi:10.1101/gad.192856.112 (2012).
- 197 Hatz, K., Schneider, U., Henrich, P. B., Braun, B., Sacu, S. & Prunte, C. Ranibizumab plus verteporfin photodynamic therapy in neovascular age-related macular degeneration: 12 months of retreatment and vision outcomes from a randomized study. *Ophthalmologica* **233**, 66-73, doi:10.1159/000367603 (2015).
- 198 Guo, L. & Teng, L. YAP/TAZ for cancer therapy: opportunities and challenges (review). *Int J Oncol* **46**, 1444-1452, doi:10.3892/ijo.2015.2877 (2015).
- 199 Moroishi, T., Park, H. W., Qin, B., Chen, Q., Meng, Z., Plouffe, S. W., Taniguchi, K., Yu, F. X., Karin, M., Pan, D. & Guan, K. L. A YAP/TAZ-induced feedback mechanism regulates Hippo pathway homeostasis. *Genes Dev* **29**, 1271-1284, doi:10.1101/gad.262816.115 (2015).
- 200 Nguyen, L. T., Tretiakova, M. S., Silvis, M. R., Lucas, J., Klezovitch, O., Coleman, I., Bolouri, H., Kutuyavin, V. I., Morrissey, C., True, L. D., Nelson, P. S. & Vasioukhin, V. ERG Activates the YAP1 Transcriptional Program and Induces the Development of Age-Related Prostate Tumors. *Cancer Cell* **27**, 797-808, doi:10.1016/j.ccell.2015.05.005 (2015).
- 201 Santucci, M., Vignudelli, T., Ferrari, S., Mor, M., Scalvini, L., Bolognesi, M. L., Uliassi, E. & Costi, M. P. The Hippo Pathway and YAP/TAZ-TEAD Protein-Protein Interaction as Targets for Regenerative Medicine and Cancer Treatment. *J Med Chem* **58**, 4857-4873, doi:10.1021/jm501615v (2015).
- 202 Zhao, B., Ye, X., Yu, J., Li, L., Li, W., Li, S., Yu, J., Lin, J. D., Wang, C. Y., Chinnaiyan, A. M., Lai, Z. C. & Guan, K. L. TEAD mediates YAP-

- dependent gene induction and growth control. *Genes Dev* **22**, 1962-1971, doi:10.1101/gad.1664408 (2008).
- 203 Huang da, W., Sherman, B. T. & Lempicki, R. A. Systematic and integrative analysis of large gene lists using DAVID bioinformatics resources. *Nat Protoc* **4**, 44-57, doi:10.1038/nprot.2008.211 (2009).
- 204 Pellegrinelli, V., Heuvingh, J., du Roure, O., Rouault, C., Devulder, A., Klein, C., Lacasa, M., Clement, E., Lacasa, D. & Clement, K. Human adipocyte function is impacted by mechanical cues. *J Pathol* **233**, 183-195, doi:10.1002/path.4347 (2014).

CURRICULUM VITAE

Lauren R. Bringman

Education

Doctor of Philosophy, Biochemistry and Molecular Biology **January 2017**

Mentor: Dr. Clark Wells, Ph.D.

PhD Minor: Cancer Biology

Indiana University, Indianapolis, IN GPA 3.75/4.0

Bachelor of Science in Biology, Chemistry

May 2010

Research Mentor: Dr. George Bennett, Ph.D.

Academic Minor: Political Science

Millikin University, Decatur, IL GPA 3.62/4.0

Professional Experience

Postdoctoral Fellowship in Pathology

July 2016-Present

Mentors: Drs. David Lombard, M.D., Ph.D. and Costas Lyssiotis, Ph.D.

University of Michigan, Ann Arbor, MI

Publications and Research

***Bringman, L.R.**, Lane, B.S., Folck, A., Young, S.K., Wek, R., and C.D. Wells (2016). "Stat3-mediated Sp1 transcriptional activity drives total Amot transcription to control Yap nuclear activity and CTGF expression in breast cancer. (To be submitted).

***Bringman, L.R.**, Sandusky, G., and C.D. Wells. (2016). "Angiomotin is elevated across multiple breast cancer tissue subtypes." (To be submitted).

Ranahan, W.P., Heller, B.L., **Bringman, L.R.** Lane, B.R., and C.D. Wells (2016). "Amot 80 promotes Yap nuclear activity in mammary epithelia." (To be submitted).

Wang, H., Cai, S., Bailey, B.J., Saadatzadeh, M.R., Ding, J., Tonsing-Carter, E., Georgiadis, M., Gunter, T.Z., Long, E.C., Minto, R.E., Gordon, K.R., Sen, S.E., Cai, W., Eitel, J.A., Waning, D.L., **Bringman, L.R.**, Wells, C.D., Murray, M.E., Sarkaria, J., Gelbert, L.M., Jones, D.R., Cohen-Gadol, A.A., Mayo, L.D., Shannon, H.E., and K.E. Pollok. (April 2016). "Combination therapy in a xenograft model of glioblastoma: Mdm2 antagonist enhances anti-tumor activity of temozolomide." Journal of Neurosurgery. Epub ahead of print.

Adler, J.J., Johnson, D.E., Heller, B.L., **Bringman, L.R.**, Ranahan, W.P., Conwell, M.D., Sun, Y., Hudmon, A., and Wells, C.D. (May 2013) "Serum Deprivation Inhibits Yes-Associated Protein and Cell Growth via Phosphorylation of Amot by the Large Tumor Suppressor Kinase." PNAS. 110(43): 17368-73.

Adler, J.J., Heller, B.L., **Bringman, L.R.**, Ranahan, W.P., Cocklin, R.R., Goebel, M.G., Oh, M., Lim, H., Inghan, R.J., and Wells, C.D. (April 2013) "The Amot130 adapts Atrophin-1 interacting protein 4 to inhibit Yes Associating Protein signaling and cell growth." JBC. 288(21): 15181-93.

Adler, J.J., Judd M.V., **Bringman L.R.**, Wells C.D., and Marrs, K.A. (April 2013). "Day as a Pathologist: Utilization of Technology to Guide Students in Exploring Careers in Breast Cancer Pathology" The American Biology Teacher. 75(8): 559-565.

Bennett, G.D., ***Bringman, L.R.**, (April 2011). "Synthesis of bicyclo[4.3.0]non-3-ene-7,9-diones via solventless Diels-Alder methodology." Synthetic Communications. 41(6): 898-902.

Bennett, G.D., ***Bringman, L.R.**, *Wildman, E.M., Wheeler, K.A. (Sept 2010). "Synthesis and Structures of Two Functionalized Isobenzofurans: (3aR,7aR,4S,5S)-1,3,3a,4,5,7a-hexahydro-5-methyl-3-oxoisobenzofuran-4-carboxylic acid and (3a α ,4 β ,7 β ,7a α)-4-[(acetyloxy)methyl]-3a,4,7,7a-tetrahydro-7-methyl-1,3-isobenzofurandione." Journal of Chemical Crystallography. 40(1): 76-79.

**Indicates first authorship*

Professional Presentations

Bringman, L.R. (June 2016). "Specificity Protein 1 induces the expression of Angiomotin in response to IL-6/STAT3 activation to mediate YAP-dependent growth of breast cancer cells." Thesis Defense Presentation: IU School of Medicine, Indianapolis, IN.

Bringman, L.R., Lane, B., and C.D. Wells. (Dec 2015). "The convergence of inflammatory IL-6/Stat3 signaling and cellular de-differentiation in breast cancer." Poster Presentation: ASCB Annual Meeting. San Diego, CA.

Bringman, L.R., Lange, K., Ranahan, W., and C.D. Wells. (Dec 2014). "Alternative transcription of Amot80 and Amot130 in response to inflammation in breast cancer." Poster Presentation: ASCB Annual Meeting. Philadelphia, PA.

Bringman, L.R., Lange, K., Ranahan, W., and C.D. Wells. (Oct 2014). "Alternative transcription of Amot80 and Amot130 in response to inflammation in breast cancer." Poster Presentation: ASCB Midwest Membrane Trafficking and Signaling Symposium. Louisville, KY.

Bringman, L.R., Ranahan, W., and C.D. Wells (May 2014). "Alternative transcription of Amot 80 and Amot 130 in response to inflammation in breast cancer." Keynote Address: Millikin University GOLD Lecture. Decatur, IL.

Funding and Research Support

T32: Lung Immunopathology Training Grant

January 2017-January 2019

Wells Lab Breast Cancer Research Foundation of Indiana University

September 2014-June 2016

Educational Enhancement Grant

December 2014

Graduate and Professional Student Government of Indiana University

Professional Affiliations and Awards

Millikin University Carl and Lucille Weatherbee Chemistry Award

May 2010

-For the Chemistry major who has done note-worthy research under direction of a University faculty member and who has made the most outstanding contributions to the University in other areas.

Millikin University Clyde Dennis Award **May 2010**

-Given to one student whom has made outstanding contributions to the University and the Biology Department

Millikin University Chemistry Fellow's Recipient **January 2009**

-Fellowship in the amount of \$1000 provided to fund the research of the Chemistry student with the most noteworthy research.

Millikin University *Cum Laude*

May 2010

American Society of Cell Biology

September 2014-Present

Image selected for cover photo of The American Biology Teacher, October 2013 Edition

Leadership Experience

- Solicited nearly \$1500 in private donations made to the Wells Lab Breast Cancer Research Foundation (2014-2016) through annual fundraisers and rolling donation acceptance.
- Developed and coordinated IUSM Biochemistry "Student Data Club," a student-led group fostering student to student critiques, feedback, and scientific discussion (2013-2016).
- Elected Student Representative of the IU School of Medicine Dept. of Biochemistry and Molecular Biology (2013-2015).
- Served on the Board of Graduate Student Representatives, an IUSM Travel Grant Selection Committee (2013-2014).
- Elected President for Millikin University's American Cancer Society Chapter (2009-2010)
- Elected President for Millikin University's Collegiate Rotary Chapter (2006-2010)
- Elected Senator for the College of Arts and Sciences for Millikin University Student Senate (2006-2010)
- Served as a member of Millikin University Varsity Competitive Cheerleading Squad (2006-2010)
- Served as a Delta Delta Delta fraternity officer in the following positions: Academic Chair, House Manager (2006-2010)

Volunteer Experience

Big Brothers Big Sisters of Central Indiana

2012-Ongoing

Big Sister

Provide one-on-one academic, career, and personal mentorship to an Indianapolis teen-aged girl

Families First

2013-2016

Domestic violence support group facilitator

Provided education and awareness in healthy relationships and anger management to victims of domestic violence aged <18 yrs.